CONSTRUCTION OF FREQUENCY-ENERGY PLOTS FOR NONLINEAR DYNAMICAL SYSTEMS FROM TIME-SERIES DATA

BY

XINGYUAN WANG

THESIS

Submitted in partial fulfillment of the requirements
for the degree of Master of Science in Mechanical Engineering
in the Graduate College of the
University of Illinois at Urbana-Champaign, 2010

Urbana, Illinois

Advisers:

Professor Lawrence A. Bergman
Professor D. Michael McFarland
Professor Alexander F. Vakakis

Abstract

The frequency-energy plot (FEP) is a useful tool in analyzing nonlinear system response, but previous methods of generating the FEP were limited to analytical calculations or use of the wavelet transform. Although these are acceptable methods of constructing the FEP, the former requires significant computation, and the latter does not provide a sharp frequency estimate. This work presents the construction of the FEP with knowledge of the mass distribution and velocity time series, which is obtained either by direct measurement, using a laser vibrometer or equivalent; or through time differentiation or integration of measured displacement or acceleration, respectively. The FEP is generated through three intermediate steps. First, the total energy of the system is estimated by fitting a spline through the non-increasing peaks of the kinetic-energy time series. Use of the kinetic rather than the potential energy removes the need to know the nonlinear stiffnesses present in a system. Separately, the empirical mode decomposition (EMD) method is used to decompose the system response into intrinsic mode functions (IMFs) whose frequencies are then estimated with the Hilbert transform. The FEP is created by plotting these estimated frequencies against the total energy.

The components of this FEP algorithm are first defined in greater detail with a variety of examples, and an FEP is plotted for a simulated system. The system has been previously shown to exhibit 1:3 transient resonance capture (TRC), and the resulting FEP reflects that internal resonance with a sharper frequency estimate than is possible with the wavelet transform. Next, the algorithm is used to show that it is in fact possible to track the impulsive manifold when imposing different initial conditions to the same Hamiltonian system. Finally, it is applied to experimental data and simulations of the parameters identified from experimental data. Additional observations on the application of the algorithm to experimental data are also discussed, with the key conclusion that processing challenges arise when short-duration signals are analyzed with this method.

Dedicated to Liping Cai and Tingxiu Wang, whose undying love and unwavering support will forever provide sustenance

Acknowledgments

Throughout my six years at the University of Illinois, I have come to appreciate so much that goes on behind the scenes: the people who make the University run rarely receive acknowledgment, but it is truly with their help that 42,000 students and another 3,000 faculty can experience the joy of education. Professor Dimitrios Kyritsis is a good friend and mentor, and his insight has been valuable across a wide variety of topics not limited to academics. To my family and friends, who have collectively and patiently waited for my complaining about tests and homework to subside, thank you for supporting me and understanding my quirks. Your love made this project, and the at-times wandering journey that has been my college education, possible.

Being a researcher in the Linear and Nonlinear Dynamics and Vibrations Laboratory (LNDVL for "short") has also exposed me to some of the brightest students in the current field. Mrs. Mercedes Mane has been of great help in the laboratory and with MATLAB© coding suggestions, Mr. David Andersen provided invaluable time and explanation of MATLAB code, and Dr. Yuli Starosvetsky was always a tremendous repository of dynamics knowledge. The other students in the group were always willing to help as well, and even three former students—Mr. Jeffrey J. Kowtko, Dr. Young Lee (now a professor himself), and Mr. Sean Hubbard—graciously provided example files and their time to set me on my own path. Five years after depositing his own thesis, Mr. Kowtko's experimental results are still good enough to be used as a benchmark for quality data and are used in this work for signal processing.

Of course, no graduate work would be complete without mention of the advisers who first accepted the graduate student and then provided a vision for the next several years. Dr. Alexander Vakakis took a gamble and added me to the LNDVL group and has been a continual source of advice and inspiration; he championed my cause and provided support during my brief tenure in the group. Dr. Larry Bergman challenged my initial progress and asked of me the best, providing encouragement and suggestions along the way. Finally, Dr. D. Michael McFarland accepted the challenge of conceiving a project that ultimately concluded in this work. He has been a tremendous adviser and mentor, shedding light on mathematical curiosities and dispensing grandfatherly wisdom alike, and I've come to truly appreciate his coaching. It was with the patience, guiding, and inspiration of these three men that these next pages have emerged, and it is to them that I owe a sincere thank-you.

This is the culmination of an interesting journey, but may the reader take note: it was with the help and encouragement of friends, family, and colleagues that I have made it through college in one piece. Collectively, they have been, without a doubt, my "guiding light," and I thank them enormously for it.

Xingyuan Wang
May 2010

Table of Contents

List of Figures

Chapter 1

Introduction

1.1 Motivation and Related Vibrations Research

The analysis of vibrating systems has been a research field driven in large measure by practical needs. Whether to suppress unwanted vibration, such as flutter in a wing; or to introduce a calculated amount of vibration, such as the "vibrate" mode in today's electronic devices; analysis, experiment, and simulation have each played a crucial role in enhancing the state of the art in vibrations research. To be able to understand these issues, however, it is frequently appropriate to split the focus into linear and nonlinear models. It is possible to simplify most real-world systems with linear generalizations, but there is only limited applicability associated with these assumptions. Even so, the study of linear dynamics provides the foundation of mathematical understanding for how vibrating systems behave, and to this end classical texts on vibrations have explored the motivation, mathematics, and analysis of linear systems in great detail [14, 15, 20]. The mathematics of the linear case allows us to selectively suppress a particular natural frequency, but one limitation of linear energy sinks (vibration absorbers) is precisely that they are able to be tuned to one frequency—typically, only the system's resonant frequency [8]—making them impractical for situations where broadband attenuation is required. Therefore, there is great desire to consider vibration attenuation of nonlinear systems, which have interesting phenomena not observable in linear systems.

Targeted energy transfer (TET), whereby energy is transfered irreversibly from a linear element to an essentially non-linear energy sink (NES), is one aspect of nonlinear dynamics that has been extensively studied for its applicability to practical systems [22]. (An "essentially nonlinearizable" system is one that cannot be linearized.) The phenomenon has been investigated both analytically, as in Gendelman et al. [2] and Lee et al. [9]; and experimentally, as in McFarland et al. [12]. Analysis of resonance capture and impulsive orbits add to our understanding of TET and how to transfer energy passively; works such as Vakakis and Gendelman [21] and Kerschen et al. [5] discuss the mathematical intricacies of these phenomena. These analyses all give rise to the task of characterizing a nonlinear system response. Much as linear normal modes and the frequency response can help identify linear systems, there are nonlinear analogues that characterize nonlinear system response, aptly named "nonlinear normal modes" (NNMs).

Two key distinctions exist between NNMs and classical linear normal modes [22]. First, the number of NNMs may exceed the number of degrees of freedom (DOFs) of the system. Second, the governing equations of motion (EOMs) of undamped nonlinear systems can only sometimes be solved by the principle of separation of space and time, whereas for undamped linear systems, this method is always possible. Space-time separation is possible when the NNMs are *similar*, or when there are straight modal lines in the configuration space of the system. (Although it is always possible to introduce symmetry in linear systems by choosing a suitable modal transformation, the symmetries that would induce similar NNMs do not commonly occur in physical nonlinear systems.) Appropriately, *non-similar* NNMs arise when the oscillations are represented in configuration space with modal curves, and unlike similar NNMs, whose modal curves do not depend on the energy of the system, the modal curves of non-similar NNMs do depend on energy. It is due to this energy dependence that direct computation of the NNMs is difficult [22], but because such a relationship exists, it is possible to represent a synoptic view of NNMs on a frequency-energy plot (FEP).

As the name suggests, the FEP is constructed based on knowledge of the conserved total energy of a system and the frequency content of the periodic motion. Specifically, a given branch of the FEP is created by plotting a family of NNM motions that share the same qualitative features [17]. The various branches that result from plotting the periodic

solutions are denoted as $S_{nm^{\pm}}$ or U_{pq}, with S representing a symmetric solution and U an unsymmetric motion; nm (pq), an $n:m$ $(p:q)$ internal resonance; and $\pm$, either in-phase $(+)$ or anti-phase $(-)$ motion. The fundamental (backbone) curve is denoted thus as $S_{11^{\pm}}$, and various branches off of this curve denote bifurcations and are called *tongues*. To compute the NNMs, Peeters et al. recommends a combination of shooting and pseudo-arclength continuation methods [17]. Although procedures to construct an FEP have been documented in the past, there has been no signal-processing algorithm that allows for FEP construction from time series.

There are two related concerns with analytical methods of plotting the FEP. As seen in Lee et al. [9] and Peeters et al. [17], the procedure for plotting each branch systematically involves significant computation. Though the system described below and used in the remainder of this work contains only two total DOF, Peeters et al. includes a section, "Reduction of the computational burden," that warns that the complicated NNM motions quickly escalate the computational complexity as the system increases in scale [17]. In addition, and perhaps more importantly, knowledge of system parameters may not be feasible. With increasing interaction among electrical, mechanical, and recently, biological fields, the ability to estimate every spring stiffness—much less determine nonlinear spring parameters—becomes increasingly difficult. There is thus great motivation to construct the FEP from a system identification algorithm rather than from analytical calculations alone. We proceed with a summary of the complicated dynamics present in what is seemingly an innocuous 2-DOF system [9].

1.2 Dynamics of a Two-Degree-of-Freedom System

1.2.1 The Introduction of Nonlinearity into a System

One aspect that may be interesting for readers is the origin of nonlinearity: given the prominence of linear theory and how well it predicts carefully crafted real-world examples, a natural question is how to induce these nonlinearities. One way to do so is to make use of geometric properties of the system. Transverse displacements of a string, for instance,

will effect a cubic stiffness in the string restoring force due to the trigonometric relation between the string length and the transverse displacement.

Consider the wire stretched across two grounded posts depicted in Fig. 1.1.

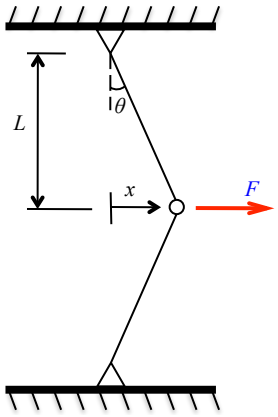

Fig. 1.1. One way to introduce nonlinearity is to make use of the geometry of a system; the deflected wire shown here provides a cubic nonlinearity.

Although it is elementary, we present here an abridged derivation for the restoring force in the nonlinear spring, with additional detail available in McFarland et al. [13]. Assuming linear material properties, the increase in tension due to stretching of the wire can be written as

$$T = EA\epsilon, \tag{1.1}$$

where A denotes the cross-sectional area; E, Young's modulus; and ϵ, the strain in the wire. From the geometry, it is clear that the stretched length of the wire resulting from a displacement x is $\sqrt{L^2 + x^2}$. If we assume a preload (initial tension) T_0 in the wire prior to deformation, the force balance becomes

$$F = 2(T_0 + T)\sin\theta. \tag{1.2}$$

The variable θ is the angle formed by the wire with its initial, horizontal position and is related to the displacement x and half-length L by $\sin\theta = x/\sqrt{L^2 + x^2}$. Substituting this expression into eq. (1.2) provides the exact expression for the force F in terms of the displacement x, but if $x \ll L$, we may use a Taylor series expansion about $x = 0$ to simplify

$F(x)$ into a more tractable form. The result, after discarding higher-order terms, is

$$F(x) = \frac{2T_0}{L}x + \frac{EA - T_0}{L^3}x^3. \tag{1.3}$$

There are three observations to be made here. The most obvious is that the linear term exists only if the wire is preloaded. Correspondingly, if the preload is increased, the restoring force $F(x)$ becomes increasingly linear. Finally, if there is no initial tension in the wire, the nonlinear spring force becomes simply

$$F(x) = Cx^3, \tag{1.4}$$

with $C = \frac{EA}{L^3}$. This expression for the essentially nonlinear force is what will be assumed in the systems in subsequent discussions, but in experimental systems, the nominally cubic exponent may vary slightly due to material properties. (For certain experiments outlined in Kowtko [8], for instance, the nonlinear exponent was 2.8 rather than 3.)

1.2.2 Analysis of the Nonlinear System

We consider a 2-DOF system with the cubic nonlinearity discussed in the previous section. The schematic of this system is depicted in Fig. 1.2. The nonlinear attachment, comprising the nonlinear spring k_2, the dashpot c_2 and the mass m_2, is the NES. The equations of motion for this system are

$$m_1\ddot{x} + k_1x + c_1\dot{x} + c_2(\dot{x} - \dot{v}) + k_2(x - v)^3 = 0, \tag{1.5a}$$

$$m_2\ddot{v} + c_2(\dot{v} - \dot{x}) + k_2(v - x)^3 = 0. \tag{1.5b}$$

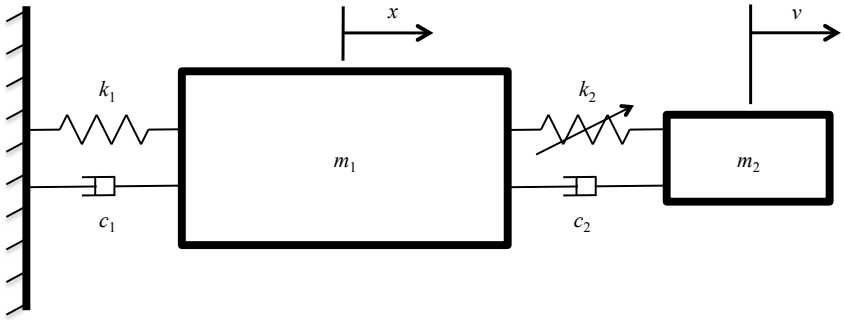

Fig. 1.2. The 2-DOF system with cubic nonlinearity due to the spring k_2.

Nondimensionalizing eqs. (1.5) with

$$\omega_0^2 = \frac{k_1}{m_1}, \quad C = \frac{k_2}{m_1}, \quad \epsilon = \frac{m_2}{m_1}, \quad \lambda_1 = \frac{c_1}{m_1}, \quad \lambda_2 = \frac{c_2}{m_1}, \tag{1.6}$$

we obtain

$$\ddot{x} + \omega_0^2 x + \epsilon\lambda_1\dot{x} + \epsilon\lambda_2(\dot{x} - \dot{v}) + C(x - v)^3 = 0, \tag{1.7a}$$

$$\epsilon\ddot{v} + \epsilon\lambda_2(\dot{v} - \dot{x}) + C(v - x)^3 = 0. \tag{1.7b}$$

Following the procedure outlined in Lee et al. [9] and Kerschen et al. [6], and considering first the undamped ($\lambda_1 = \lambda_2 = 0$) case, it is possible to classify the periodic solutions as either symmetric or unsymmetric and then to construct the FEP from these various branches. The resulting FEP of the Hamiltonian system is shown in Fig. 1.3. Clearly, the dynamics are more complicated than they might first appear for such a "simple" system; without the nonlinear spring k_2, we would expect two natural frequencies and two linear normal modes. The FEP allows us to consider particular branches in additional detail, and studying the specific branches helps us understand the resulting system dynamics.

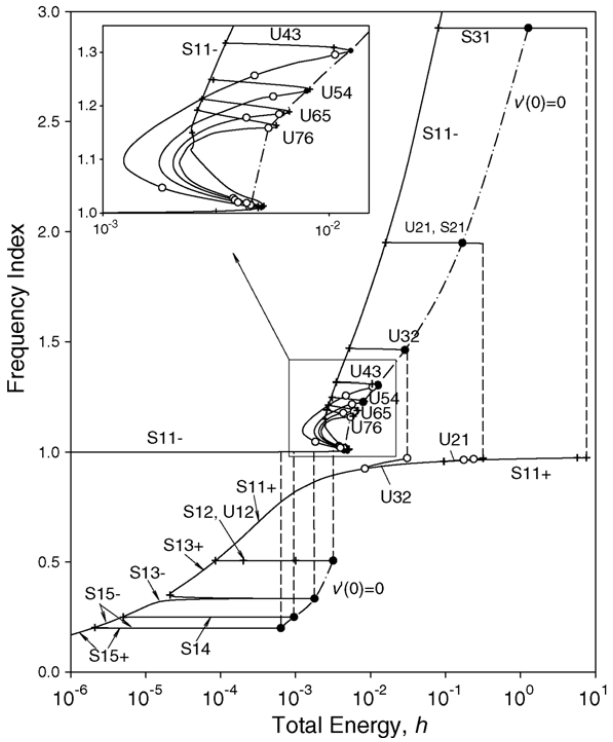

Fig. 1.3. The FEP resulting from the physical system shown in Fig. 1.2 [9].

1.3 Thesis Overview

This research considers FEP construction from time-series data as an algorithm involving four steps. First, with time-series response data and knowledge of the mass distribution, the kinetic energy can be used to estimate the total energy in the system. Second, using the empirical mode decomposition (EMD) algorithm, it is possible to decompose the system displacement time series into a set of intrinsic mode functions (IMFs). The Hilbert transform can then be applied to these monochromatic signals to obtain the frequency content of the IMFs, and as the last step, these frequencies are then plotted against the estimated energy to construct the FEP.

In Chapter 2, each step will be performed first on an example signal and then on the time series from the simulation of a physical system. Ultimately, the FEP will be constructed for a system with a known backbone curve. In Chapter 3, the algorithm is applied to experimental data collected by Kowtko [8] and simulation of a system with parameters equal to those from the experiments. The FEP will be constructed for both of these cases. The examples in both chapters will show the ability of this new algorithm to plot the FEP without significant computational resources or specific knowledge of system parameters.

Chapter 2

Algorithm for FEP Construction

Each step toward constructing the frequency-energy plot (FEP) already has practical use of its own, but they have never been brought together to generate the FEP from time series. This chapter defines each component of the algorithm. Each of the steps is first illustrated with an example of its application to a simple signal and is then demonstrated on a simulation of a physical system. The FEPs corresponding to a simulated system with various initial conditions are then presented and discussed.

2.1 Estimation of Total Energy from Kinetic Energy

2.1.1 Example of Picking Non-Increasing Peaks

The total energy of a dissipative vibrating system with no external forcing is a nonincreasing function of time. For this reason, it is possible to estimate the total energy of a system with the system's kinetic energy. Although it is possible to do the estimation with a system's potential energy, it can be tedious to ascertain the stiffness of a nonlinear spring experimentally. Because the determination of the mass distribution is typically a straightforward measurement and the velocity is simply integrated from the measured acceleration, the kinetic energy is obtained by a straightforward calculation from the time series.

To show a proof of concept, a simple function was generated first, with equation

$$x(t) = (\sin(2\pi t) + 0.3\sin(9\pi t) + 10)e^{-0.1t}. \tag{2.1}$$

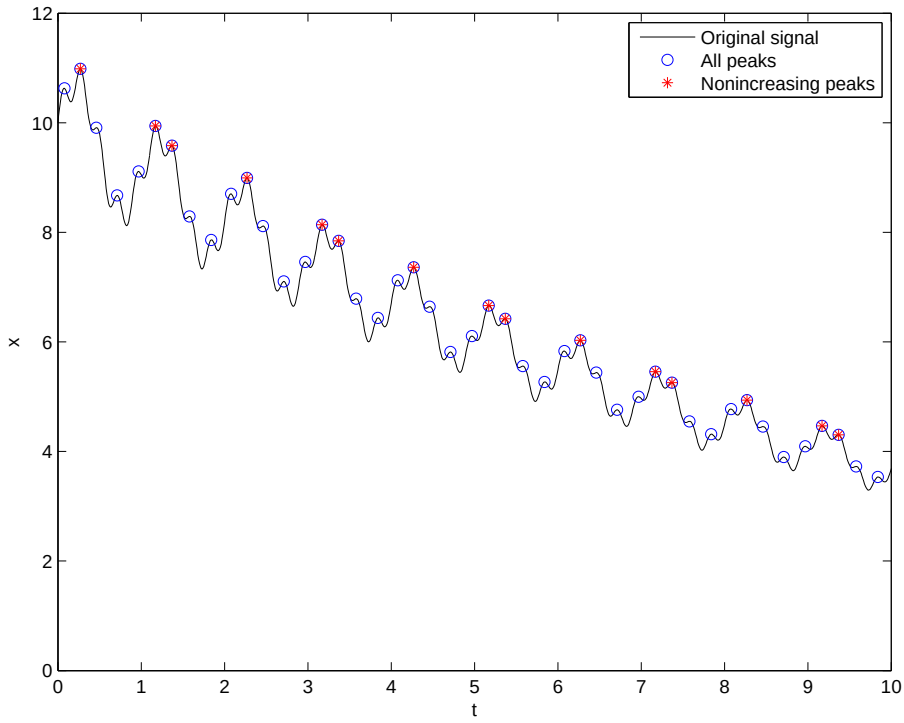

Fig. 2.1. The signal $x(t)$, peaks chosen by the peak-picking algorithm, and nonincreasing peaks.

The algorithm searches for all the peaks contained in $x(t)$, and upon identification of all the local maxima, it then picks the peaks that are nonincreasing. The signal $x(t)$, with the peaks circled and the nonincreasing peaks marked with asterisks, is plotted in Fig. 2.1. Fitting a monotonic spline to the nonincreasing peaks approximates the maximum envelope of the signal (Fig. 2.2), so that if the original signal were the kinetic energy, this process of peak-picking would result in an estimate of the total system energy.

2.1.2 Energy Estimation of a SDOF, Ungrounded NES System

With the basis of the energy estimation described, the next step is to apply the algorithm to an actual time history. A single-degree-of-freedom (SDOF) system with an ungrounded nonlinear energy sink (NES) was chosen for an initial proof of concept, and initial conditions to put the system into 1:3 transient resonance capture (TRC) were previously derived by Professor Young Lee. Schematically, the system looks like that shown in Fig. 2.3 and has displacement y for cart m_1 (the linear oscillator, LO) and v for cart m_s (the NES).

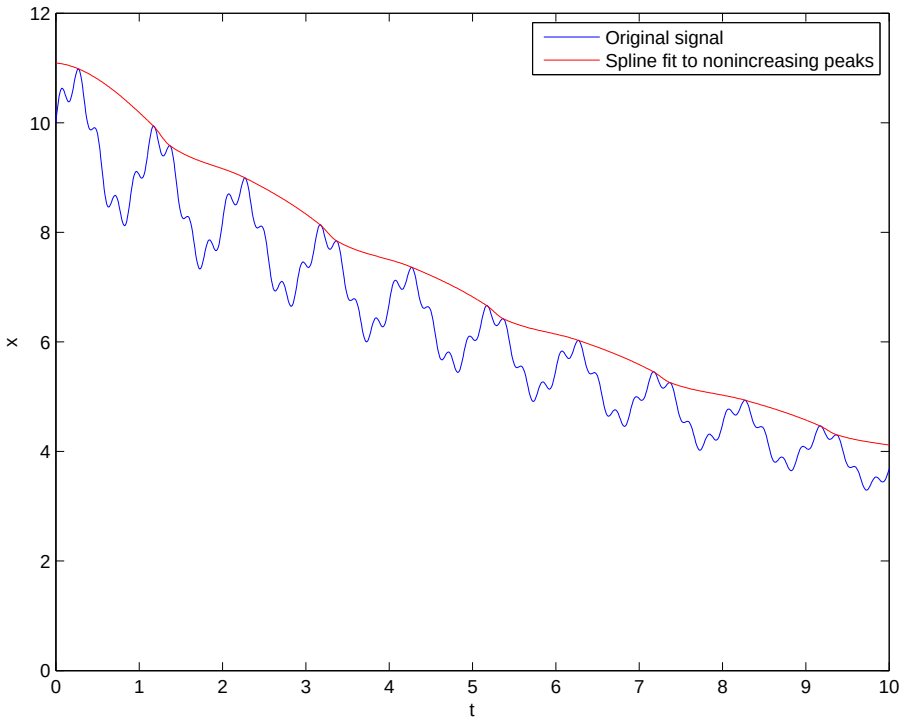

Fig. 2.2. The signal $x(t)$ and the spline fit to the nonincreasing peaks.

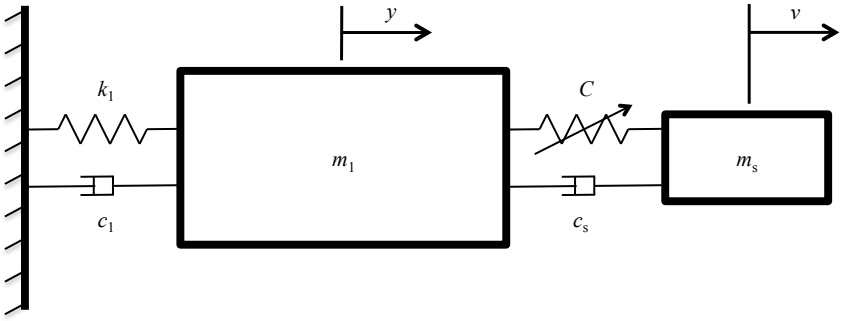

Fig. 2.3. Schematic for a SDOF system with ungrounded NES [8].

The nondimensionalized equations of motion for the system are

$$\ddot{y} + \omega_0^2 y + \epsilon\lambda_1\dot{y} + \epsilon\lambda_2(\dot{y} - \dot{v}) + C(y - v)^3 = 0, \tag{2.2a}$$

$$\epsilon\ddot{v} + \epsilon\lambda_2(\dot{v} - \dot{y}) + C(v - y)^3 = 0. \tag{2.2b}$$

The constants in eqs. (2.2) are related to physical parameters as in eq. (1.6) and are set to $\omega_0 = 1$, $C = 1$, $\epsilon = 0.05$, and $\lambda_1 = \lambda_2 = 0.03$. Because the MATLAB differential equation solver `ode45` works with first-order systems only, it becomes necessary to redefine the two

equations with state variables $\{x_1, x_2, x_3, x_4\}^T = \{y, v, \dot{y}, \dot{v}\}^T$, giving

$$\dot{x_1} = x_3, \tag{2.3a}$$

$$\dot{x_2} = x_4, \tag{2.3b}$$

$$\dot{x_3} = -\omega_0^2 x_1 - \epsilon\lambda_1 x_3 - \epsilon\lambda_2(x_3 - x_4) - C(x_1 - x_2)^3, \tag{2.3c}$$

$$\dot{x_4} = \lambda_2(x_3 - x_4) - \frac{C}{\epsilon}(x_2 - x_1)^3. \tag{2.3d}$$

To excite the system so that it enters 1:3 TRC, the initial conditions were specified to be $\dot{y}(0) = -0.05944$ and $\dot{v}(0) = 0.01500$, with both $y(0)$ and $v(0)$ equal to zero. The resulting displacements of the carts are shown in Fig. 2.4. To examine the energy of the system, we analyze the equations governing the system energy:

$$T = \frac{1}{2}(x_3^2 + \epsilon x_4^2), \tag{2.4a}$$

$$V = \frac{1}{2}k_1 x_1^2 + \frac{C}{4}(x_1 - x_2)^4. \tag{2.4b}$$

The energy stored in a spring is $\int F \mathrm{d}x$, which evaluates to the familiar quadratic form in the case of a linear spring and to the quartic term in eq. (2.4b) for a cubic stiffness. The total energy is, of course, the sum of the kinetic and potential energies, and each can be plotted as a function of time.

As is evident in Fig. 2.5, the energy of the system is monotonically decreasing. Following the discussion of Section 2.1.1, it should be possible to find the peaks of the monotonically decreasing kinetic-energy time series and estimate the total system energy by fitting a spline to the nonincreasing peaks of the kinetic energy. Applying this algorithm to the kinetic energy time series yields the plot depicted in Fig. 2.6. As this image is difficult to interpret due to the amount of data, we consider a smaller time interval in Fig. 2.7. Here, as before, it is clear that the algorithm is picking the nonincreasing peaks. This particular subset of the entire time duration is not challenging, however, as *all* the peaks also happen to be nonincreasing. It appears that $470 < t < 620$ s is a section of the total record that contains more blue circles than red asterisks; this time interval is shown in Fig. 2.8. Here again, it is clear that although there are other peaks, the algorithm has correctly identified the nonincreasing peaks. We may now fit a spline through these nonincreasing

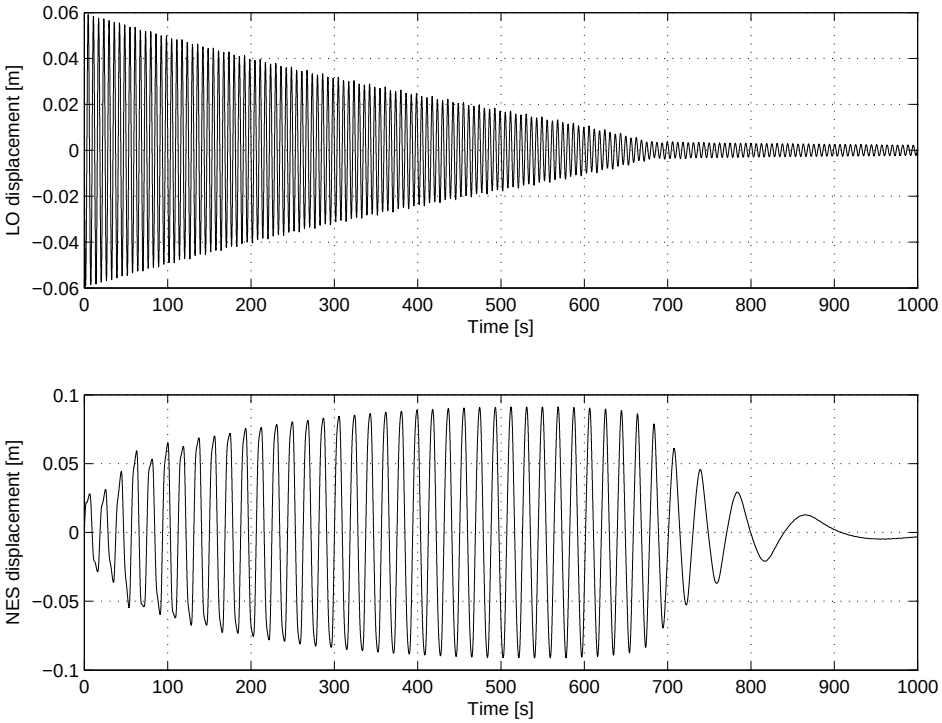

Fig. 2.4. LO and NES displacement of a system in 1:3 TRC (Fig. 2.3).

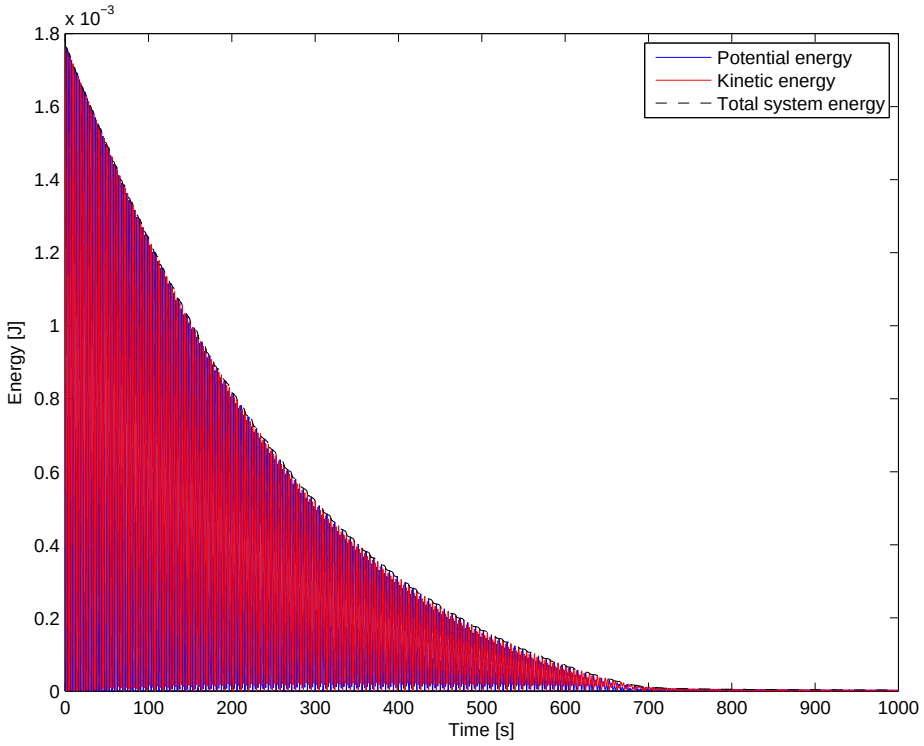

Fig. 2.5. Total energy of a SDOF system with ungrounded NES in 1:3 TRC.

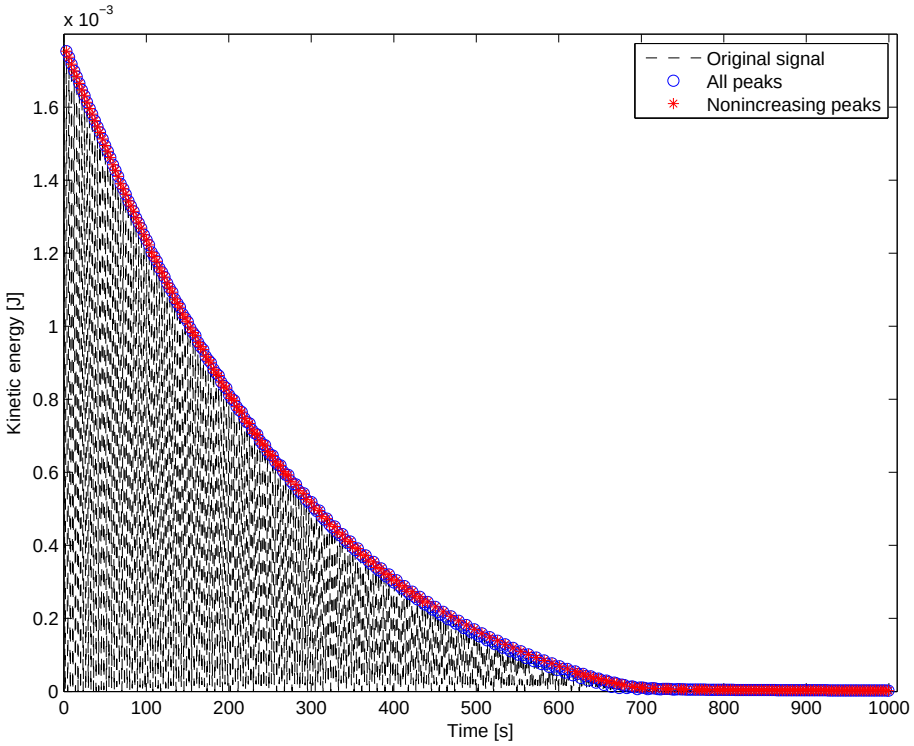

Fig. 2.6. All peaks and nonincreasing peaks of the KE time series.

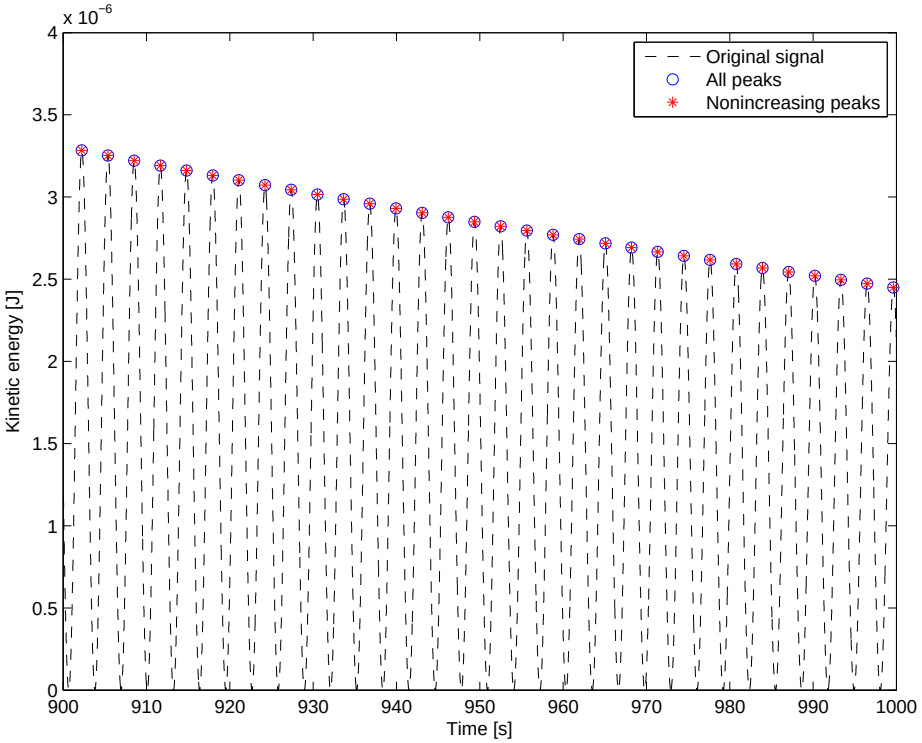

Fig. 2.7. Smaller time interval of the KE time history shown in Fig. 2.6.

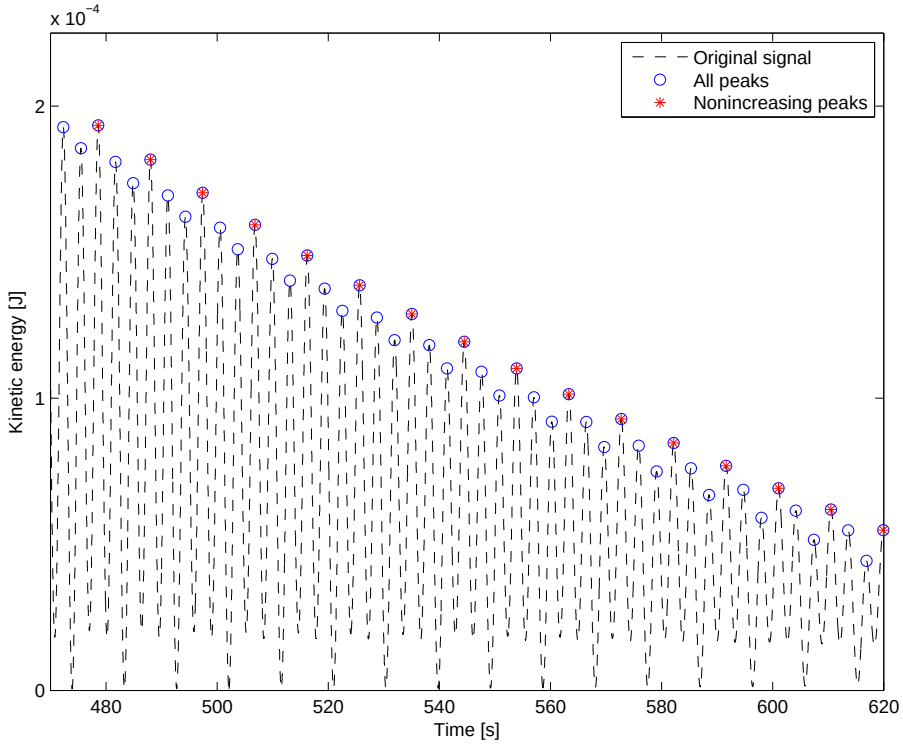

Fig. 2.8. The interval $470 < t < 620$ s from the KE time history of Fig. 2.6.

peaks to attempt to estimate the total energy; the nonincreasing peaks and the spline through them are shown in Fig. 2.9. Note that the nonincreasing peaks do not lie on a smooth curve between roughly $t = 200$ s and $t = 450$ s (i.e., one could imagine a "best fit" line going between the points rather than connect each point to its neighbor). Though this may seem like cause for concern, the FEP is not a direct function of time. The point of being able to use this algorithm is to estimate the total energy of the system using another monotonically decreasing time series (in this case, the kinetic energy of the system), so it would be appropriate to compare the spline as an estimate of the total system energy with the computed total system energy (plotted in Fig. 2.5). The results are shown in Fig. 2.10. The total energy and the estimate are clearly very close, so we have shown that it is in fact possible to estimate the total energy of a system by fitting a spline to the nonincreasing peaks of the kinetic-energy time series. This procedure forms the first component of FEP construction.

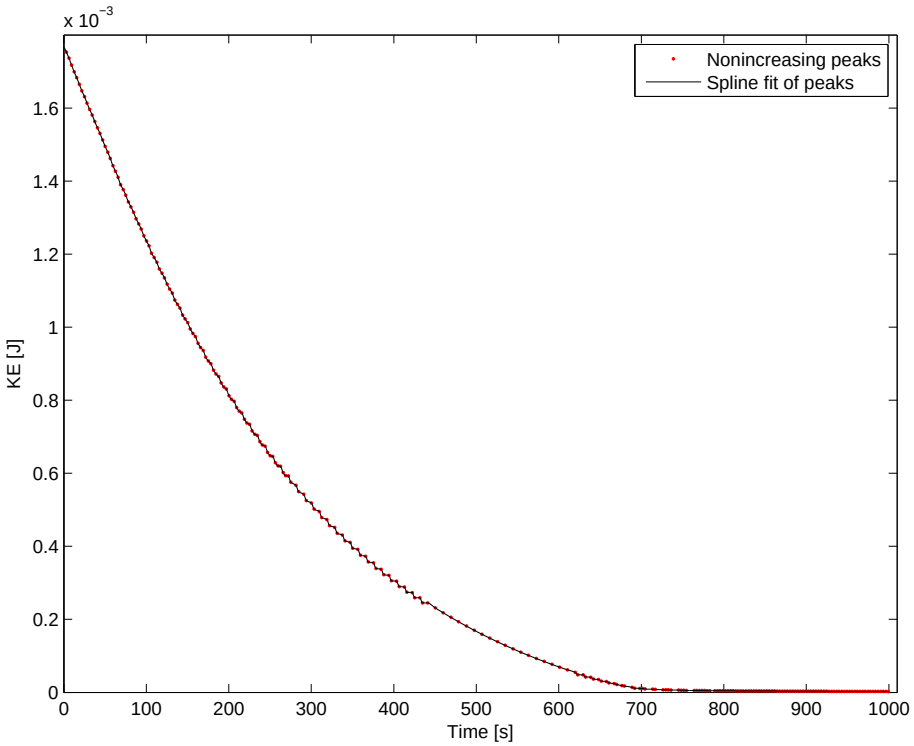

Fig. 2.9. The spline calculated from the nonincreasing peaks of the KE time series and the nonincreasing peaks.

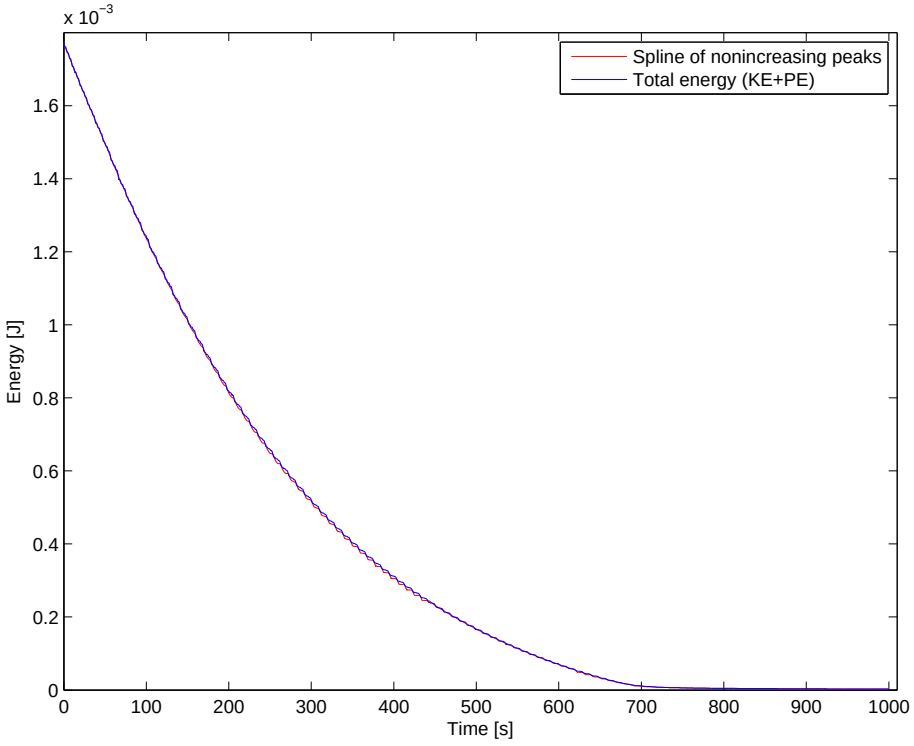

Fig. 2.10. A comparison of the actual total energy and total energy as computed by the nonincreasing peaks and spline algorithm.

2.2 Empirical Mode Decomposition

The next aspect of FEP construction is to determine the time-frequency relation of the system. Empirical mode decomposition, EMD, is used to decompose displacement time series into intrinsic mode functions (IMFs) whose frequencies can later be estimated with the Hilbert transform (Section 2.3).

2.2.1 Application of the Standard EMD to an Example Signal

We begin with an example signal comprising a sum of sinusoids of the form

$$x(t) = a_1 \sin(2\pi f_1 t) + a_2 \sin(2\pi f_2 t) + a_3 \sin(2\pi f_3 t), \tag{2.5}$$

with a_i, f_i, $i = 1, 2, 3$, distinct nonzero, real constants. In addition, we choose the ratio of any two frequencies to be outside the range [0.5, 2]. This choice of widely-spaced signal frequencies helps decompose the signal $x(t)$ into clean monochromatic signals. For our example, we take

$$x(t) = \sin(2\pi 10t) - 1.5 \sin(2\pi 25t) + 0.5 \sin(2\pi 60t). \tag{2.6}$$

A time interval of this signal is plotted in Fig. 2.11. The signal $x(t)$ is a stationary sum of sinusoids, so the Fast Fourier Transform (FFT) and Power Spectral Density (PSD) techniques should be able to find the three dominant frequencies f_1, f_2, and f_3. Both are able to do so admirably; the result is plotted in Fig. 2.12. The `fft` function in MATLAB can also find the phase of the signal $x(t)$, which in this case is constantly 0. The relative magnitudes of the peaks of the PSD, computed with MATLAB's `pwelch` function, reflect our choice that $|a_2| > |a_1| > |a_3|$. Although they work well here, the FFT and PSD are not as useful when the signal is not stationary. To decompose such signals, an alternate algorithm must be used.

The goal of the EMD algorithm is to decompose this type of signal into intrinsic mode functions (IMFs). First defined by Huang et al. [4], IMFs are defined by having two key characteristics.

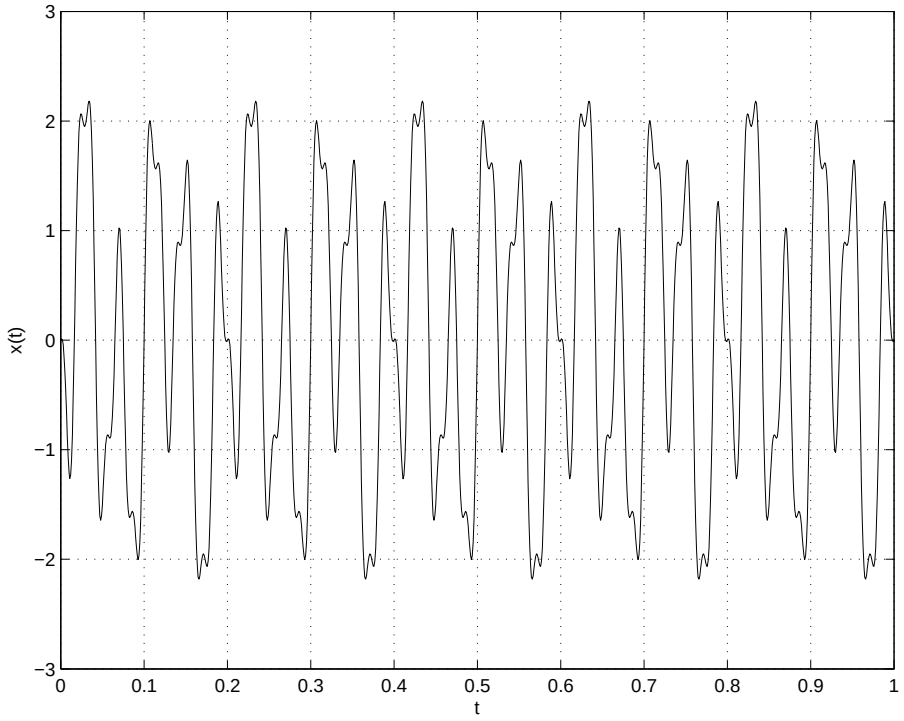

Fig. 2.11. The interval $0 \leq t \leq 1$ s of the signal $x(t)$ used to demonstrate the EMD process.

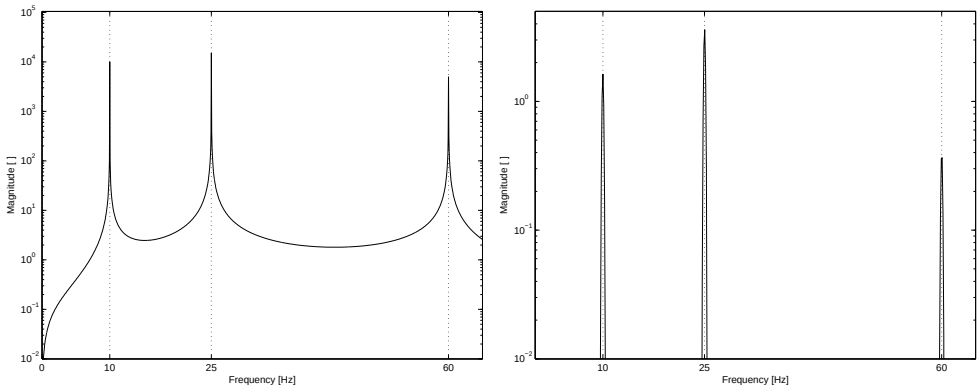

(a) FFT magnitude of $x(t)$ (b) PSD of $x(t)$

Fig. 2.12. The FFT and PSD analyses easily find the three frequencies present in the original signal $x(t)$.

- The number of extrema and zero crossings must differ by at most one;
- The IMF must have zero local mean.

The procedure of the EMD algorithm is summarized by Lee et al. [10] in the section, "Standard Empirical Mode Decomposition Method." The EMD code utilized was that of Professor Patrick Flandrin [18]. We would expect the EMD algorithm to generate three

IMFs whose individual frequencies correspond to f_1, f_2, and f_3. The sum of these IMFs should be equal to the original $x(t)$, so the amplitude of the individual IMFs should also reflect the constants a_1, a_2, and a_3. A small time interval of the IMF decomposition is shown in Fig. 2.13. The wavelet transform (WT) of each IMF is plotted in Figs. 2.14, and it is evident that one IMF has frequency 60 Hz; another, 25 Hz; and the third, 10 Hz.

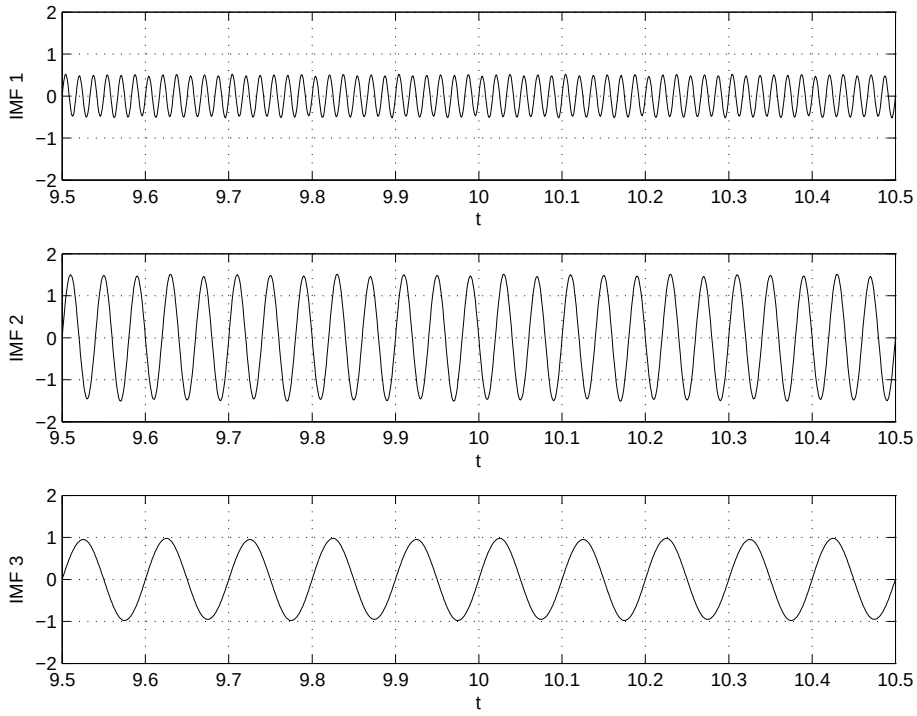

Fig. 2.13. A portion of the three IMFs generated by the standard EMD algorithm.

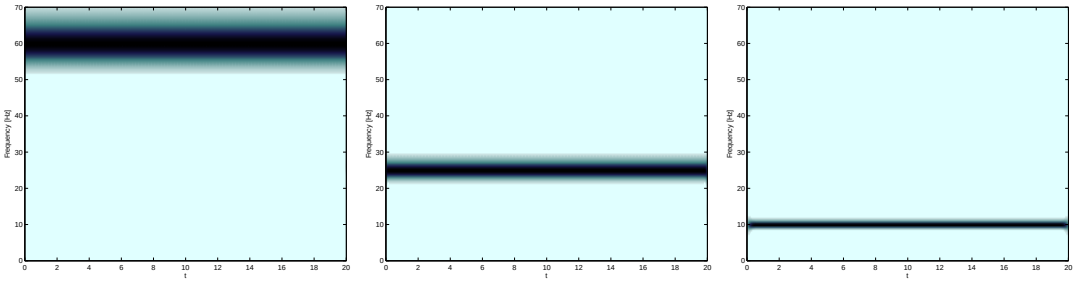

(a) Wavelet transform of IMF 1 (b) Wavelet transform of IMF 2 (c) Wavelet transform of IMF 3

Fig. 2.14. The wavelet transforms of each of the IMFs.

The sum of the IMFs should be identical to the original signal. To verify that the EMD algorithm has indeed produced satisfactory IMFs, in Fig. 2.15 we plot the sum of the three IMFs of Fig. 2.13 and the original signal $x(t)$.

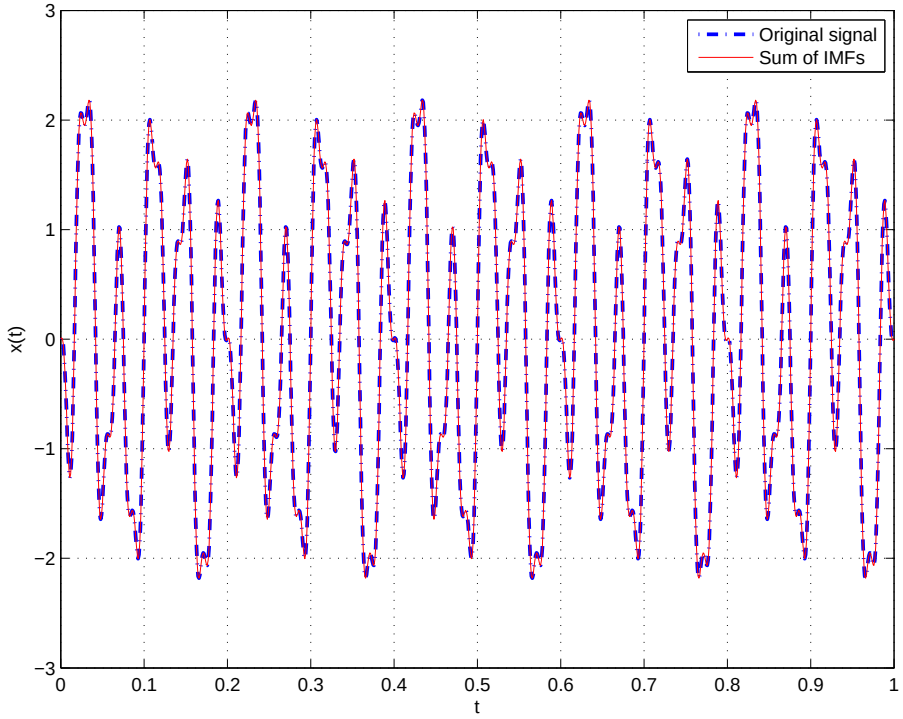

Fig. 2.15. The three IMFs of Fig. 2.13 sum to the original signal $x(t)$.

Although we have called the EMD algorithm satisfactory in its abilities to produce IMFs, we must be cognizant of possible issues with the IMFs generated. Many of these effects will be discussed in Section 2.2.2, because it is appropriate to treat IMF processing on a case-by-case basis, but the effects are worthy of mention here. Two factors contribute to end effects at the beginning and end of the time interval. First, the signal being sampled is finite (in this case, the total record length was 20 s), and second, the signal is not smooth at $t = 0$ s or $t = 20$ s. The end effects at small time are shown in Fig. 2.16; they exist at $t = 20$ s as well, but we present only the early-time end effects for brevity. It is clear that at small time, the IMFs don't quite behave exactly as expected. One expectation is that they would resemble sine functions with the appropriate frequency; that is, at $t = 0$ s, the value of each IMF should be zero. The IMFs here clearly do not have zero initial values and instead behave more as do cosine functions. In addition, both the first and second

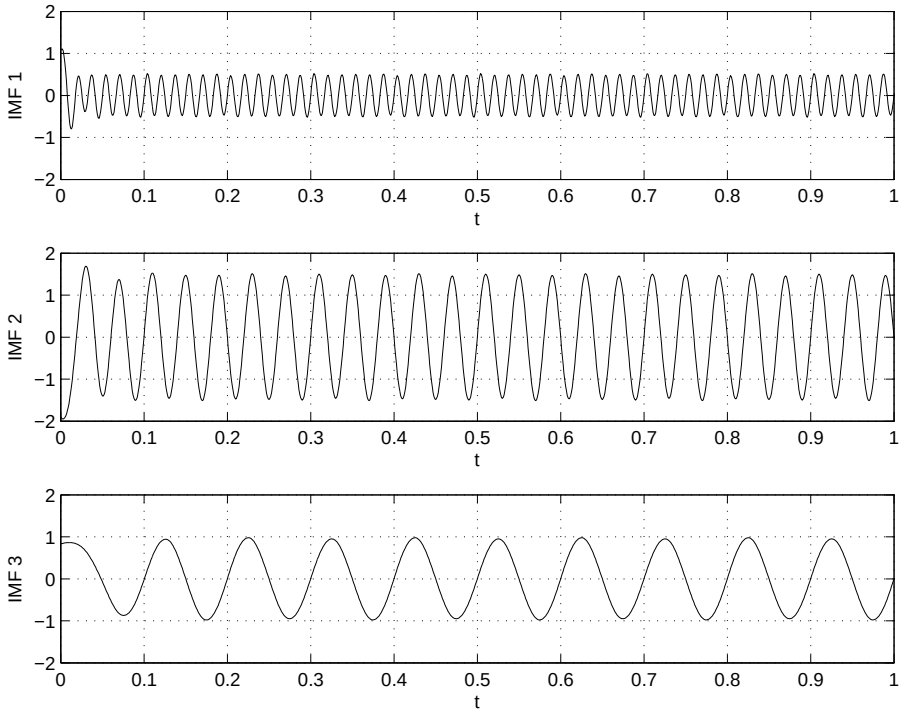

Fig. 2.16. The three IMFs have end effects near $t = 0$ s because of the finite nature of the time series and the non-smoothness present at $t = 0$ s.

IMFs have the end effect previously discussed. These are both issues that can be addressed with a variety of processing techniques, but the primary goal here was to apply the EMD process to a simple signal and to show that it is indeed possible to decompose a signal into IMFs whose sum returns the original signal. We have demonstrated that here, and leave the further processing of the IMFs to the following section.

2.2.2 Applying the EMD Procedure to the Time Series of a Physical System

Now that we have discussed the application of the EMD to an example signal, we turn our attention to the system described previously (see Fig. 2.3) with nondimensionalized equations of motion (2.2). Applying the EMD algorithm to the displacement vectors yields eight IMFs corresponding to the LO displacement and a further eight for the NES. The first two IMFs of each oscillator are plotted in Fig. 2.17. The linear oscillator IMFs look acceptable at first glance; the plot in the first row of Fig. 2.17 is qualitatively similar to the LO displacement, as expected, and the plot in the second row seems plausible as the

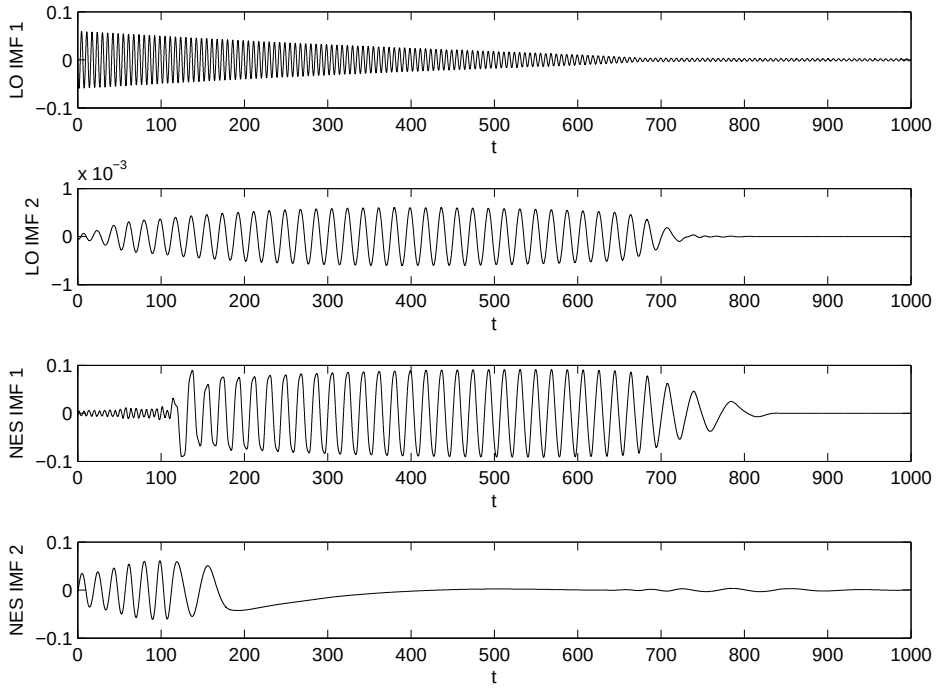

Fig. 2.17. The first two IMFs for both the LO and NES calculated using the standard EMD procedure.

slower-frequency NES oscillation. Closer inspection of the second LO plot does reveal that near $t = 0$ s, not all conditions for being an IMF are satisfied, so this is one aspect that needs to be addressed. More worrisome, however, is that the NES IMFs are not at all ideal, as it appears that the two IMFs plotted ought to be summed rather than be considered separately. In fact, the second NES IMF for $t < 100$ s seems to exhibit the same frequency behavior as that for $t > 100$ in the first, so it appears that the NES displacement has managed to confuse the EMD algorithm. The reason this occurs is that the high-frequency content contributes little to the overall NES response [10]. One way to address this critical issue is to use a cleverly designed masking signal (which can be incorporated with an `option` in the EMD code) that helps amplify the high-frequency component. This procedure, combined with the use of mirroring to mitigate end effects, forms the basis for the "advanced" EMD (AEMD) procedure described in detail in Lee et al. [10].

As a brief but important digression, we note that the specific methodology used to obtain the optimal IMFs out of a specific time series is highly dependent on the time series being considered. There are undoubtedly challenging time series for the EMD to process

alone, and questions arise about sifting parameters and end conditions [16]. There has been much research to mitigate undesirable effects, and the AEMD methodology is but one tool available. Other EMD processing tools, including detailed consideration of the masking signal, are discussed in Senroy et al. [19] and in Deering and Kaiser [1].

With this point in mind, and for the purposes of FEP construction of the current system, we will first ensure smoothness at $t = 0$ s by mirroring the time series. As described in the AEMD paper, it is possible to choose either an odd or an even mirror. An even mirror essentially flips positive time about the ordinate axis and is suitable for even signals; an odd mirror flips positive time about the origin, and naturally is the mirror of choice for odd signals. The original time series (red) and its mirrors (blue) are plotted in Fig. 2.18. The top plot shows the new displacement $\hat{x}_1$ for the linear oscillator, and the bottom shows the resulting displacement of $\hat{x}_2$, corresponding to the NES. To verify that the mirror did ensure smoothness at $t = 0$ s, consider Fig. 2.19, a close-up of Fig. 2.18 near $t = 0$. This figure demonstrates convincingly that the entire signal $\hat{x}$ is in fact continuous and differentiable everywhere for $0 \leq t < 1000$ s. The IMFs resulting from mirroring the time series should correct the end effects at $t = 0$ s, and the results are depicted in Fig. 2.20. At $t = 0$, it is clear that the now-differentiable time series yields an IMF that satisfies the conditions for being an IMF, but the NES IMFs still need some work.

The issue with processing the NES time series with the EMD tool is that the algorithm cannot find the high-frequency component of the original time series, because it is hidden among the other harmonics with larger amplitude. We now apply a masking signal that will allow the EMD algorithm to compute more efficiently the IMF corresponding to the high-frequency component in the NES time series. The masking signal takes the form

$$x_{\text{mask}}(t) = a_1 sin(\omega t) + a_2 cos(\omega t), \tag{2.7}$$

where the constants a_1, a_2, and ω are selected based on the specific data being analyzed [10]. The frequency ω for the system at hand was chosen to be 1 rad/s, as this corresponds to the highest frequency present in the system. It is also the frequency of the component whose amplitude is buried among the NES response, so the remaining decisions involve the choice of which trigonometric function and what amplifying coefficient to use. With no displacement

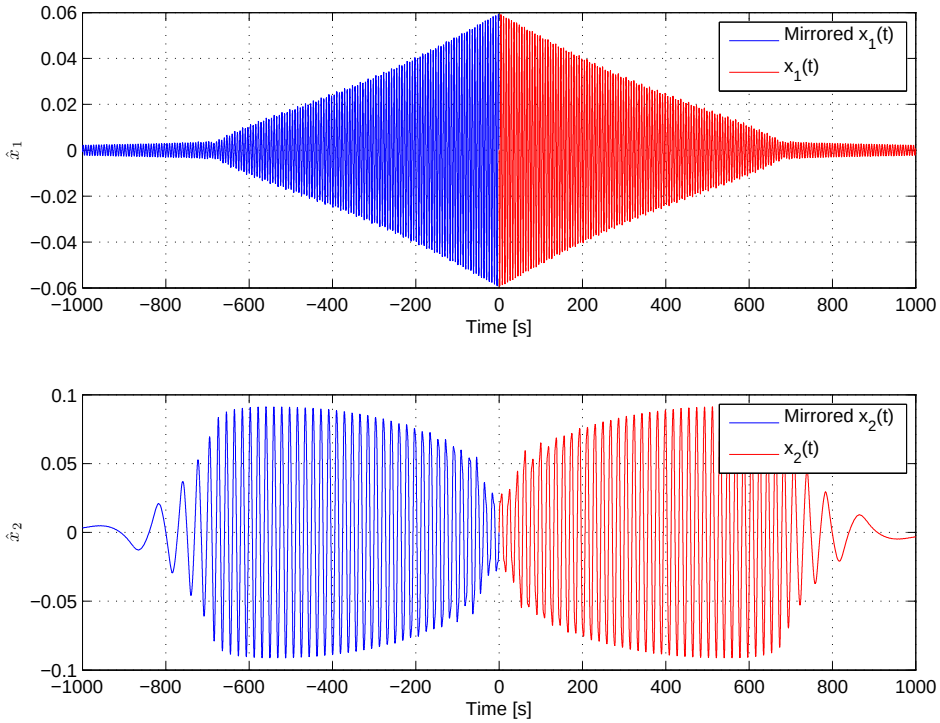

Fig. 2.18. The results of mirroring the linear oscillator displacement (top) and the NES displacement (bottom) with an odd mirror.

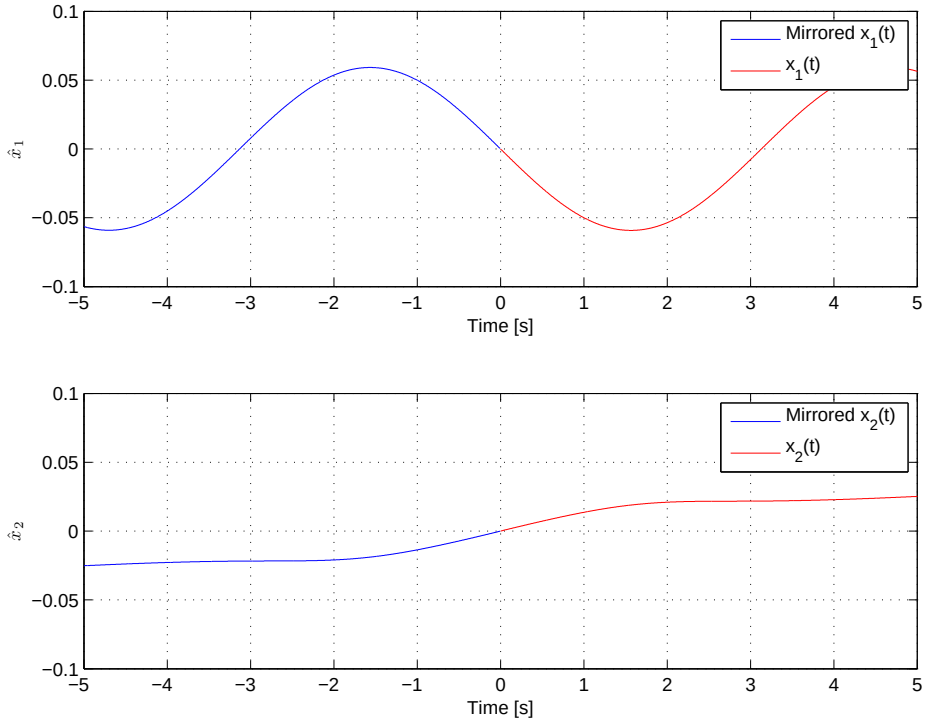

Fig. 2.19. Mirroring the signal about the origin introduces smoothness at $t = 0$ s.

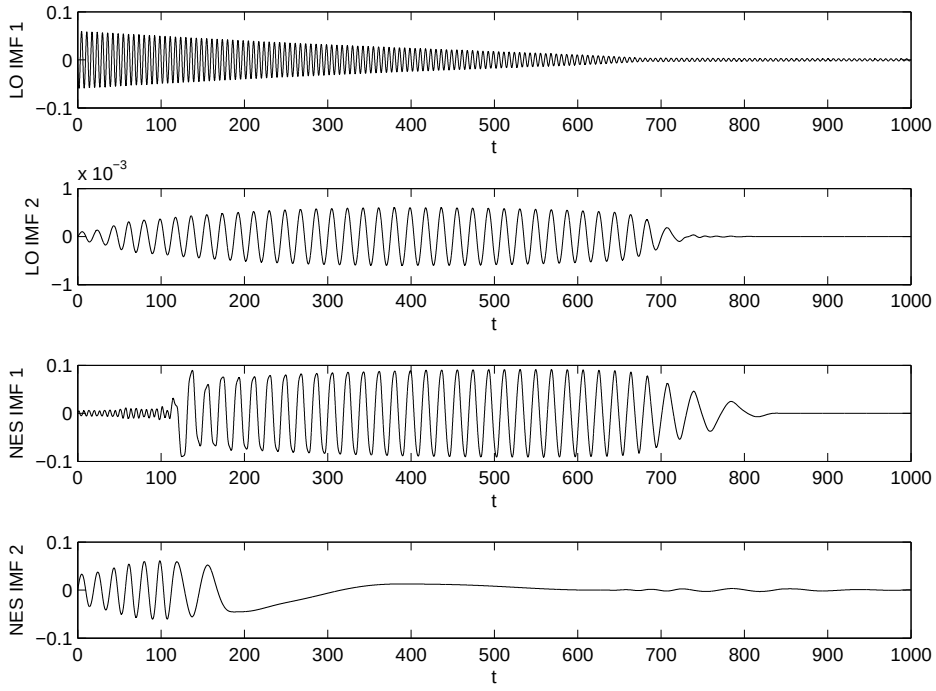

Fig. 2.20. The first two IMFs for each of the LO and NES calculated using the EMD procedure with mirroring of the original time series.

initial conditions imposed on the system, it is clear that the starting displacements of both the linear oscillator and NES are zero. For this reason, we will choose $a_2 = 0$ in eq. (2.7), allowing an in-phase initial condition between the masking signal and the original signal, and concentrate solely on the choice of a_1. Although the choice of this coefficient is empirical, we can let $a_1 = \alpha x_{\max}$ and vary α. The coefficient $x_{\max}$ is the maximum amplitude of the NES displacement. After several simulations, it became apparent that $\alpha = 0.7$ seemed to be the threshold for which the EMD algorithm could still decompose the IMFs correctly, and it is with this masking signal, and with the mirror defined previously, that the IMFs of Fig. 2.21 were generated. The mirroring removes the end effects, and it is clear from the IMFs at $t = 0$ that the initial conditions are satisfied (namely, that the displacements of the LO and NES are zero at $t = 0$). The masking signal has also correctly decomposed the NES displacement into its IMFs, and the slow-frequency mode of the second IMF closely resembles the actual NES displacement of Fig. 2.4.

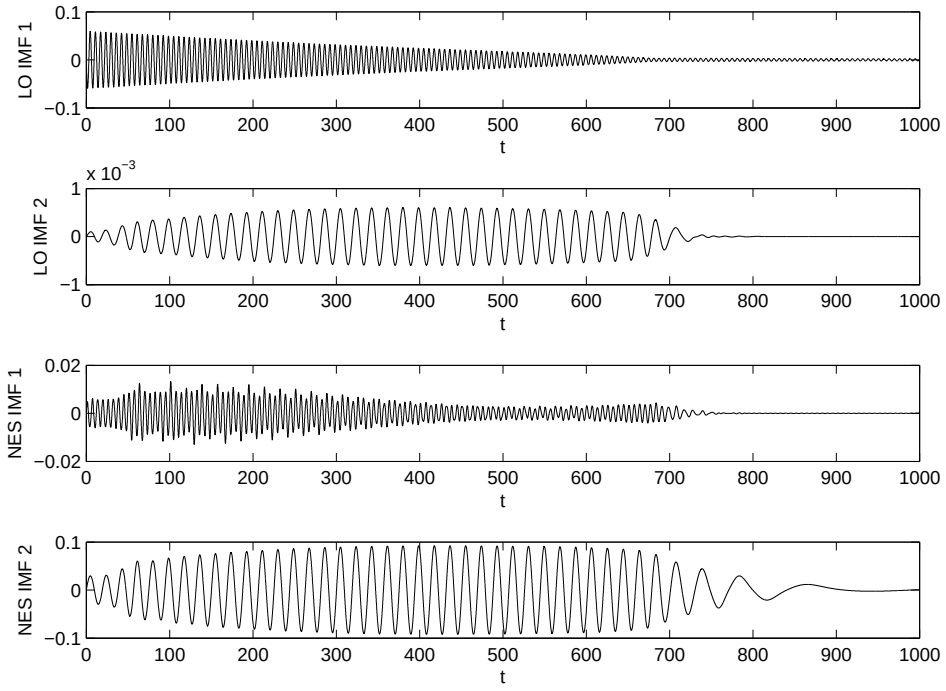

Fig. 2.21. The first two IMFs for each of the LO and NES calculated using the AEMD procedure with a masking signal, mirroring, and windowing.

2.3 Amplitude and Frequency Demodulation

2.3.1 Amplitude and Frequency Demodulation of an Example Signal

It is possible to estimate the frequency of a stationary, monochromatic signal by eye, but when the time response is frequency modulated, a more precise analysis is typically required to evaluate the frequency content. The Hilbert transform (HT) and wavelet transform are two ways to estimate the frequency content of the signal; here, we focus on the former as a potentially sharper tool for frequency estimation of a monochromatic signal. If we have a signal with modulated amplitude and modulated frequency of the form

$$x(t) = A(t)\sin(F(t)), \tag{2.8}$$

with

$$A(t) = A_0 + \sin(2\pi f_1 t) \tag{2.9}$$

and

$$F(t) = F_0 t + C\sin(2\pi f_2 t), \tag{2.10}$$

$f_1 \neq f_2$, the MATLAB command `hilbert` can be used to compute the Hilbert transform. For the original signal $x(t)$, `hilbert` x(t) produces a vector $z(t) \equiv x(t) + j\mathcal{H}(x(t))$, the analytic signal. The phase of $z(t)$ is $\theta(t) = \tan^{-1}\frac{\mathcal{H}(x(t))}{x(t)}$, which is related to the frequency of $z(t)$ by $\omega(t) = \dot{\theta}(t)$. The amplitude of the transformed signal is simply $|z(t)|$. With this, it should be possible to compare the estimated amplitude $|z(t)|$ and frequency $\omega(t)$ against the actual amplitude $A(t)$ and frequency $\frac{d}{dt}(F(t))$, respectively, to verify that the estimated frequency is nearly identical to the actual frequency. Values were assigned to the parameters in $A(t)$ and $F(t)$: in eq. (2.9), $A_0 = 1$, $f_1 = \frac{1}{100}$; and in eq. (2.10), $F_0 = 6$, $C = 5$, and $f_2 = \frac{1}{40}$. A plot showing the original signal $x(t)$ and its modulating functions $A(t)$ and $F(t)$, and the results of the Hilbert transform, is provided as Fig. 2.22. Plotting the Hilbert transform and the wavelet transform on the same axes shows the sharpness offered by the Hilbert transform in estimating the frequency of the signal, shown in Fig. 2.23. It is interesting to note that even without any means of making $z(t)$ a completely clean signal (end effects and rippling are still present), the deviation of $\omega(t)$ is still smaller than the band of the wavelet transform and therefore offers more precision on the actual frequency content of the signal.

It is apparent from Fig. 2.22 that the Hilbert transform does an admirable job at capturing the amplitude and frequency of the input signal $x(t)$. In fact, $|z(t)|$ and $\omega(t)$ are nearly identical to $A(t)$ and $\frac{d}{dt}(F(t))$ with the exceptions of the endpoints of the time scale and of some ripples for $t > 60$ s. In the former instance, the end effects exist due to the finite time interval and due to the absence of any windowing. (Although we have previously discussed mirroring, we will investigate mitigation of these undesirable effects with windowing in the next section.) In an extreme case, it is possible to choose the constant f_2 to confuse the wavelet transform greatly, and the sharpness of the Hilbert transform is even more apparent. Maintaining $A_0 = 1$ and $f_1 = \frac{1}{100}$ in eq. (2.9) as before, we now choose $F_0 = 6$, $C = 5$, $f_2 = \frac{1}{10}$ in eq. (2.10). The Hilbert transform is able to capture the frequency of this new signal, as seen in Fig. 2.24, but following even just a four-fold increase

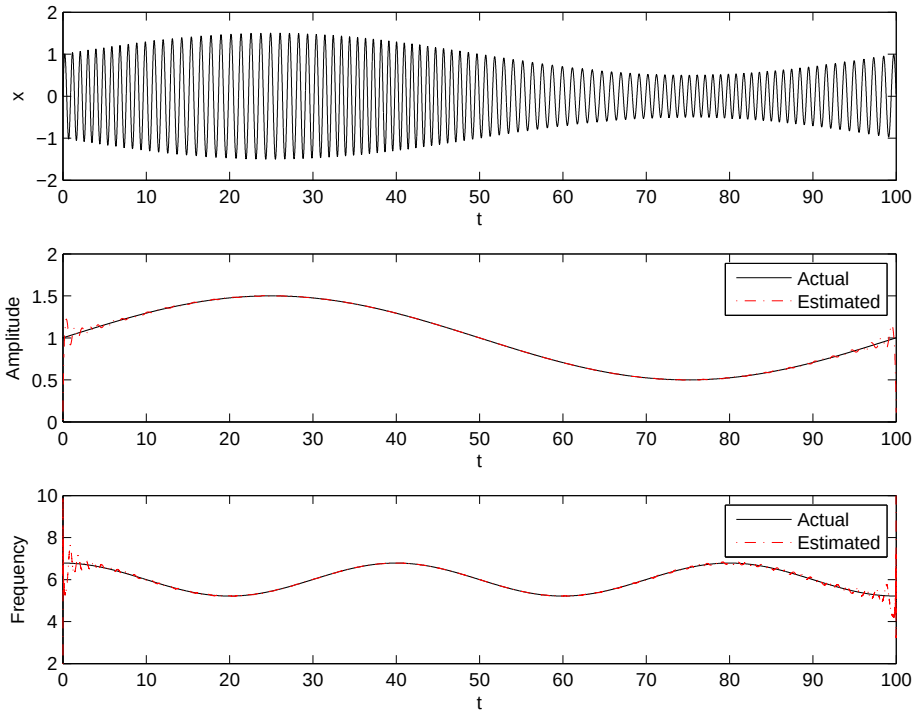

Fig. 2.22. Plot showing the original signal $x(t)$ and its actual and estimated amplitude and frequency modulation.

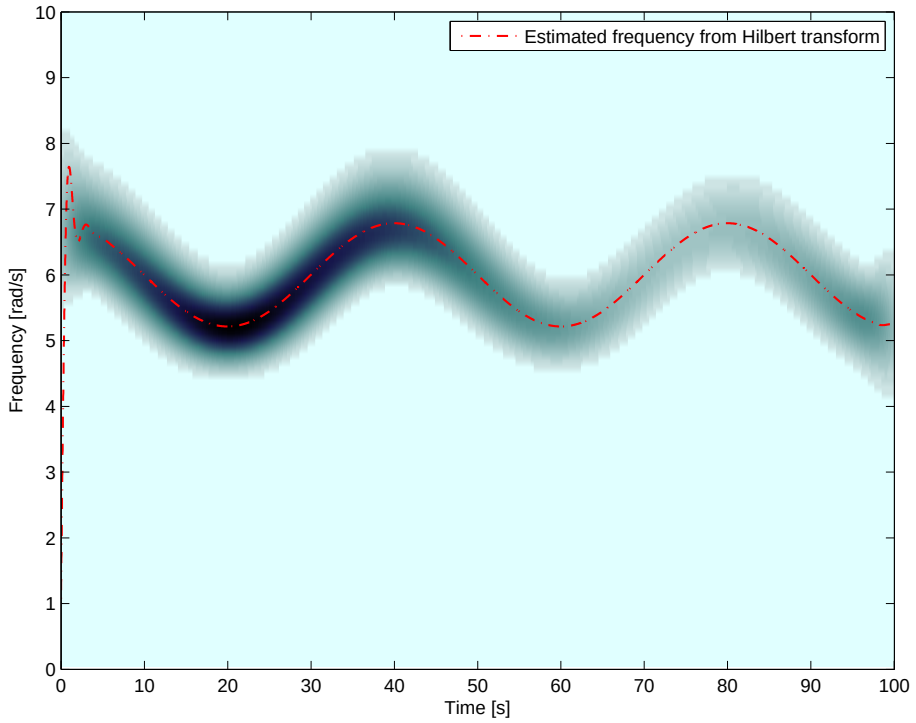

Fig. 2.23. Though the wavelet and Hilbert transforms show the same estimated frequency, the sharpness of the Hilbert transform is readily apparent.

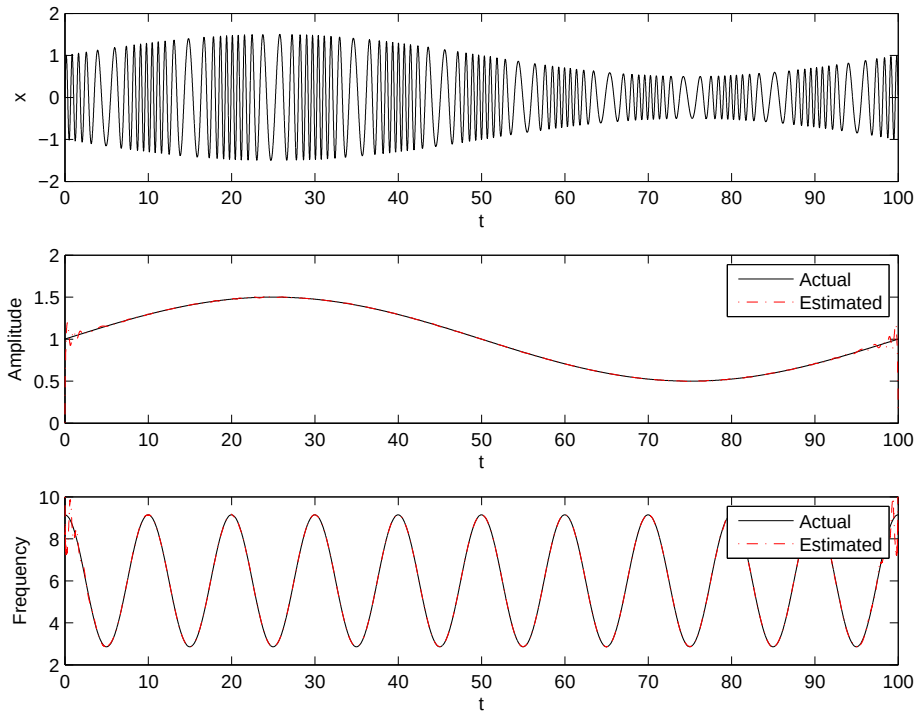

Fig. 2.24. The Hilbert transform is able to demodulate the signal $x(t)$ with a higher modulating frequency.

in the frequency of $x(t)$, the wavelet transform algorithm has a difficult time estimating the frequency content of this new signal. The complicated wavelet transform amplitude is shown in Fig. 2.25. There are still end effects and a ripple in this Hilbert transform, as again the data has not had a window applied and has not been filtered, but it is clear from Fig. 2.24 that the Hilbert transform has managed to capture the frequency content of $x(t)$ quite successfully. It is interesting to compare the wavelet transform to the Hilbert transform for these chosen parameters of $F(t)$, so Fig. 2.26 shows an overplot of the Hilbert transform on the wavelet transform. In contrast to the results obtained using the previous value of the signal parameters, where the Hilbert transform merely had more sharpness than the wavelet transform, to the untrained eye the current wavelet transform looks far messier than the clean lines of the Hilbert transform. This quick example shows that when a monochromatic signal is available, the Hilbert transform will provide a sharper estimate of the modulating frequency than can the wavelet transform.

The end effects present at both $t = 0$ and $t = t_f$ are undesirable and are due to the finite nature of the signal. Although mirroring works to reduce end effects, as shown in

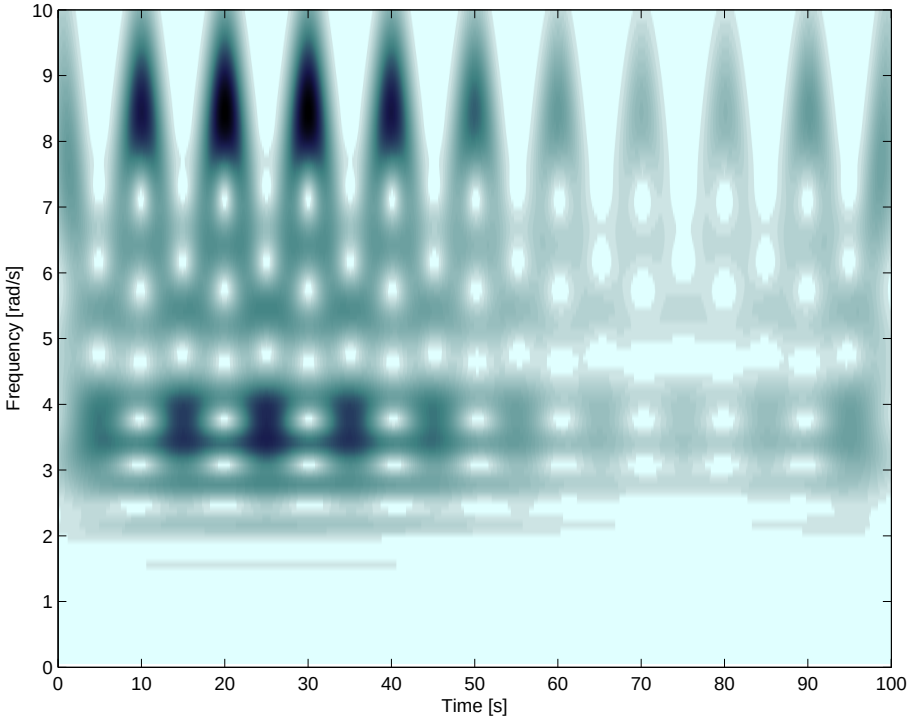

Fig. 2.25. With a slightly higher modulating frequency, it is difficult to deduce the frequency content of the new signal from the wavelet transform.

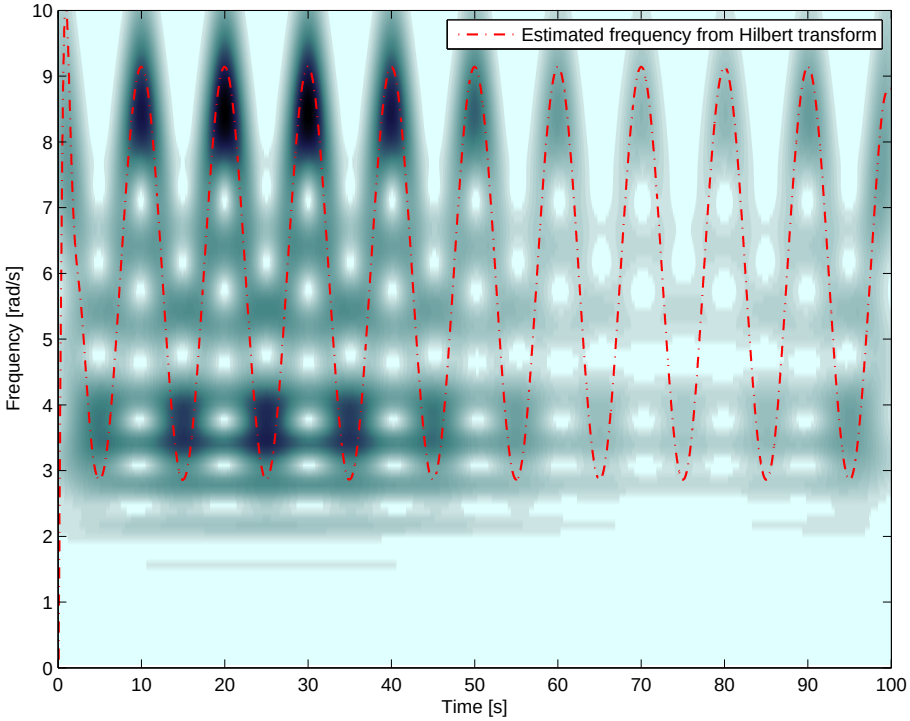

Fig. 2.26. The HT still has decipherable results with the new frequency.

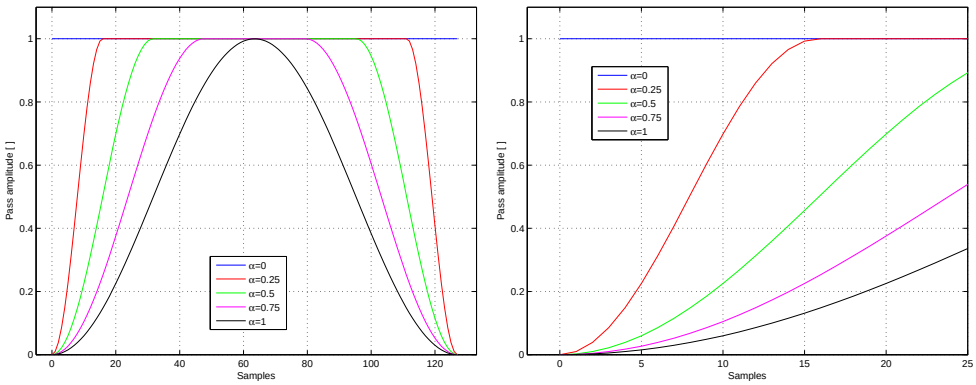

(a) Effects of α on window

(b) Smoothness of window

Fig. 2.27. Left: at $\alpha = 1$, the window is a Hann window; at $\alpha = 0$, it is a rectangular window. Right: Even as α tends toward 0, the `tukeywin` function maintains smoothness.

Section 2.2.2, it is important to recall the procedure of the FEP algorithm: the Hilbert transform is used to demodulate a signal into its frequency and amplitude, so mirroring a signal might or might not be required if the signal being processed by the Hilbert transform is already continuous at $t = 0$ s. In the case of FEP construction, the IMFs are the result of a signal that had already been mirrored, so the Hilbert transform would not see a discontinuity or a non-differentiable point at $t = 0$ s. Hence, we present a brief overview of windowing to show its effects on reducing (but not eliminating) the end effects of a Hilbert-transformed signal. A tapered cosine was chosen to preserve as much of the signal as possible while enforcing a fast rise time. Some examples of the tapered cosine windows generated with MATLAB's `tukeywin`, or tapered cosine, window are shown in Figs. 2.27. As the parameter α decreases toward the lower limit of 0, the window applied becomes more and more rectangular, becoming a rectangular window at $\alpha = 0$; at the upper limit of $\alpha = 1$, the window is equivalent to a Hann window. Note that the smoothness and differentiability of the cosine function is maintained even as the window resembles a rectangular window at $\alpha = 0.25$ (Fig. 2.27(b)). The shape of the window chosen for removing most end effects in our specific example is shown in Fig. 2.28; here, $\alpha = 0.05$. To reduce the ripple present in the frequency and amplitude demodulation, a tenth-order (after using the MATLAB

command `filtfilt`), low-pass Butterworth filter with a cutoff frequency $f_c = 40$ Hz was used. The effects of the windowing and filter are shown in Figs. 2.29 and 2.30.

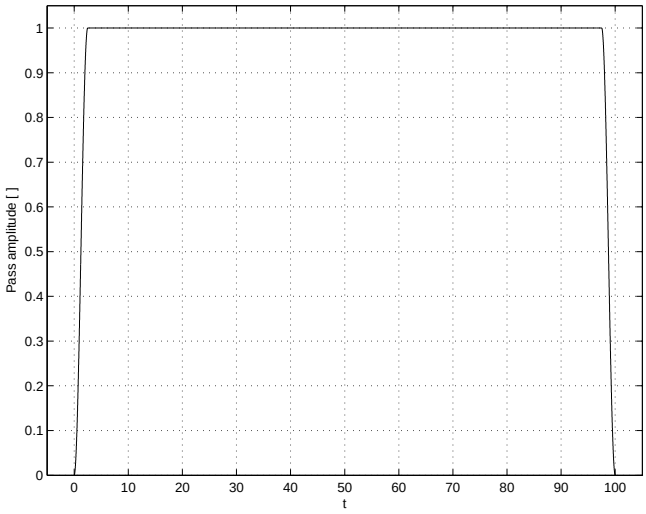

Fig. 2.28. The window used is a tapered cosine that is nearly rectangular.

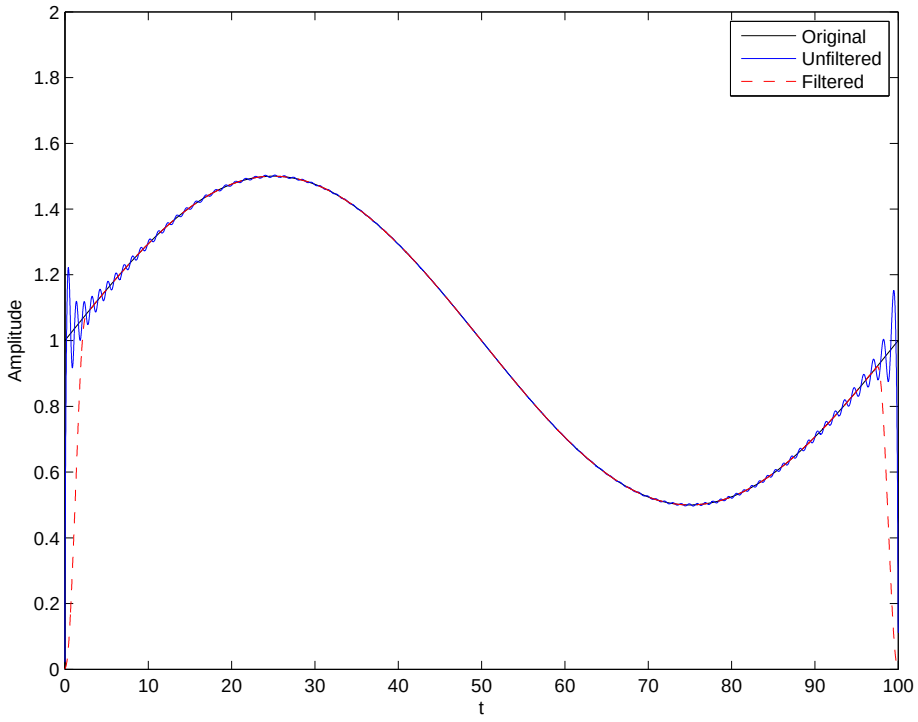

Fig. 2.29. Windowing reduces the end effects of the amplitude demodulation.

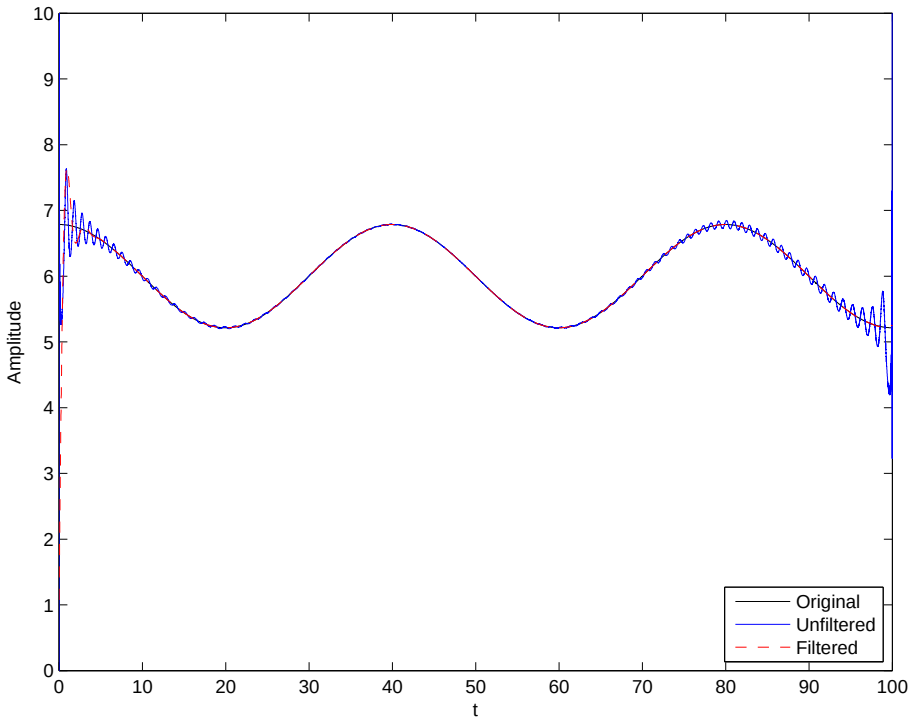

Fig. 2.30. With both windowing and filtering, the estimated frequency also has fewer end effects and less rippling.

The frequency and amplitude demodulation of all subsequent IMFs were generated with a mirrored signal, and the frequencies of these IMFs were then calculated after a tapered cosine window had been applied across the entire time record. This double application removes end effects at $t = 0$ s with mirroring, and the window helps reduce their effects at large time. Low-pass filtering was also applied to reduce high-frequency content, but ultimately, the choice of end effect mitigation technique is best decided on a case-by-case basis.

2.3.2 Amplitude and Frequency Demodulation of the IMFs of a SDOF System with Ungrounded NES

We now have the tools necessary to process the IMFs discussed in Section 2.2.2. The Hilbert transform allows us to calculate the frequency and amplitude of a monochromatic signal, and it is ultimately with this frequency component and the estimated energy discussed in Section 2.1.2 that the FEP is constructed.

Following the steps of Section 2.3.1, it is possible to extract the frequency and amplitude components of the IMFs with the Hilbert transform. The first two figures show the results of applying the Hilbert transform (with tapered cosine window) to the IMFs computed from the standard EMD (Fig. 2.17) and from the EMD of the mirrored signal (Fig. 2.20), respectively. In Fig. 2.31, the windowing helps to reduce some of the end effects, which were otherwise orders of magnitude higher than the expected amplitude or frequency.

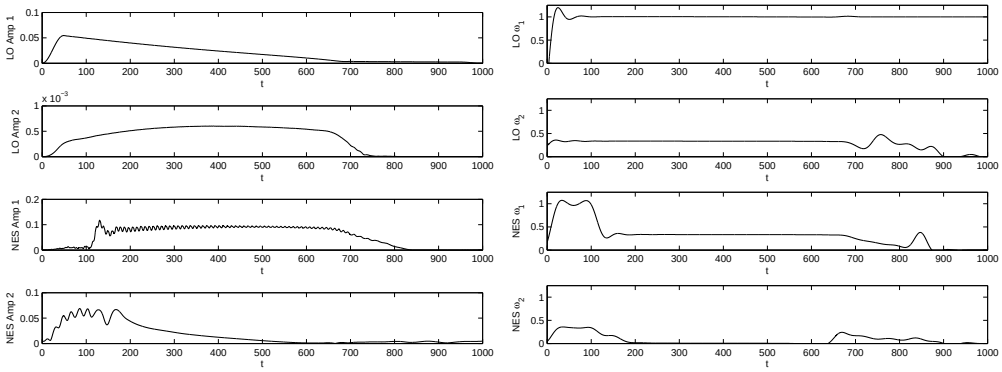

(a) Amplitude (b) Frequency

Fig. 2.31. Amplitude and frequency of the IMFs generated without the use of mirroring or a masking signal.

The LO frequencies here do not look entirely unreasonable—the top plot of Fig. 2.31(b) seems to suggest that the LO has a frequency of 1 rad/s, as expected. The trouble is with the NES, which, according to the third plot of Fig. 2.31(b), seems to oscillate with a frequency of roughly 0.33 rad/s, but only after 150 seconds. (This time delay behavior was not apparent in the displacement plot, Fig. 2.4, however!) The next set of IMF amplitudes and frequencies, Fig. 2.32, were generated from the signal that had been mirrored before applying the EMD algorithm, but no masking signal was used to produce the IMFs. The linear oscillator frequencies look better only because the end effects have been reduced, but the mirroring did not help produce cleaner NES IMFs. This isn't much of a surprise, as mirroring is not intended to amplify the high-frequency component that was causing the EMD algorithm grief in the first place. If we consider now the IMFs of Fig. 2.21, generated with mirroring and a masking signal, the resulting frequencies should be much more presentable. A window was applied to the IMFs prior to using the Hilbert transform

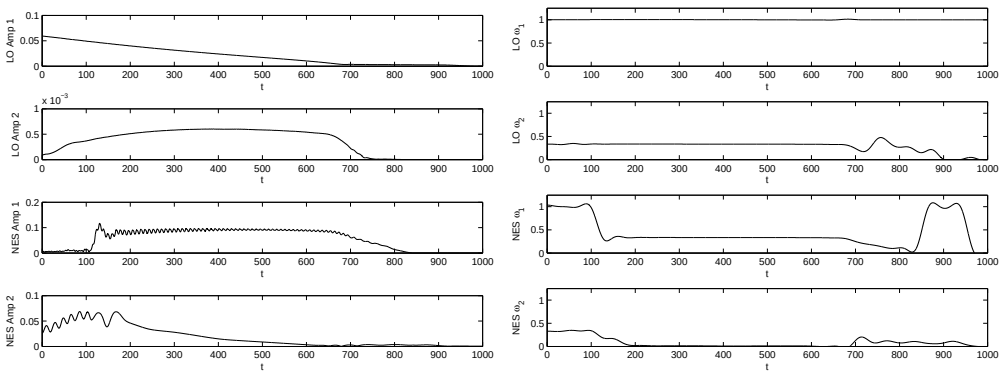

(a) Amplitude (b) Frequency

Fig. 2.32. Amplitude and frequency of the IMFs generated with mirroring but without a masking signal.

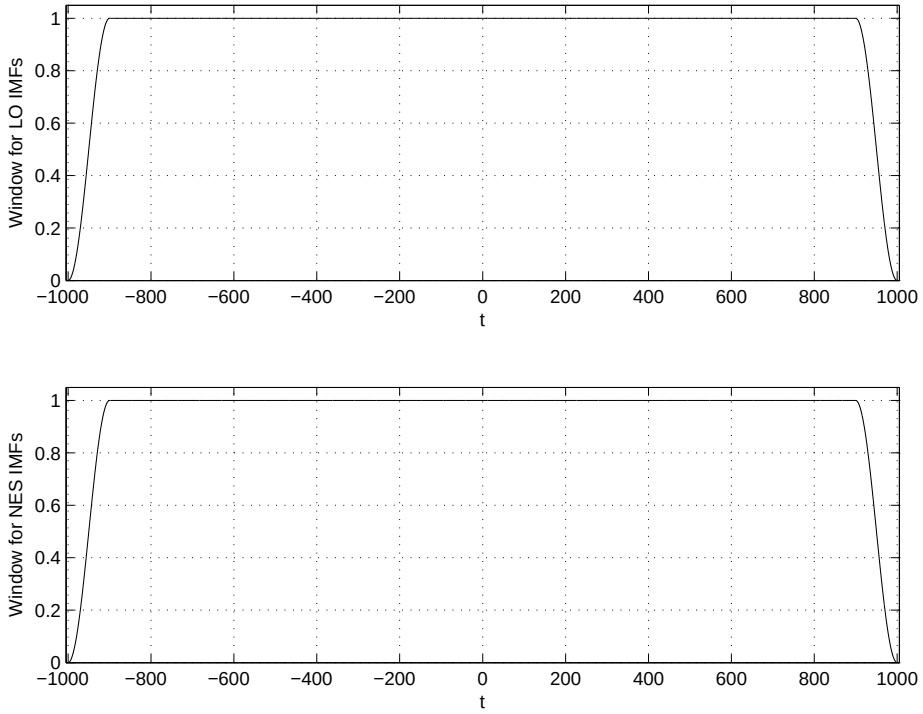

Fig. 2.33. The tapered cosine window applied to the full time interval $\hat{t}$ prior to taking the Hilbert transform of the IMFs.

to calculate the IMF amplitudes and frequencies, and the specific window (Fig. 2.33) was chosen to mitigate end effects but to retain as much data as possible. In this sense, we desire a faster window than a traditional Hann window and thus choose a version of the tapered cosine window. Applying the Hilbert transform to the IMFs of Fig. 2.21, the frequency and amplitude components are quickly found to be those shown in Fig. 2.34. As expected from

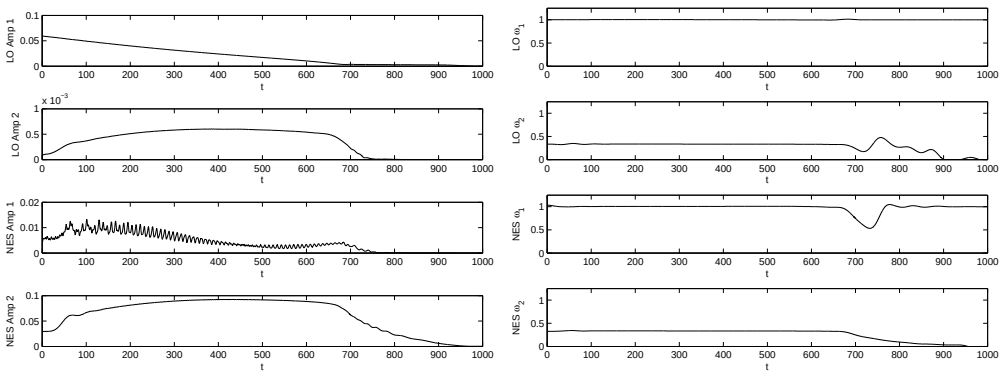

(a) Amplitude (b) Frequency

Fig. 2.34. The Hilbert transform demodulation of the amplitude and frequency of the IMFs produced using mirroring and a masking signal.

the equations of motion and knowledge that the system should enter 1:3 TRC, the IMFs confirm that the linear oscillator oscillates with a natural frequency of 1 rad/s, and the NES oscillates with a frequency roughly one-third of that. As shown in Fig. 2.34, the first plot shows a clean, sharp 1 rad/s oscillation of the LO, and the fourth plot, a 1/3 rad/s oscillation that decays after about 700 s for the NES. With the frequencies and energies determined, it is now possible to construct the FEP.

2.4 Frequency-Energy Plot Construction

2.4.1 The FEP of a System in 1:3 TRC

Recall the three main steps discussed: energy estimation, generating IMFs, and estimating the frequencies of the IMFs. The FEP is constructed by plotting these frequencies against the estimated total energy, and the construction of the FEP is simply a matter of choosing the correct IMF frequencies to plot. Visually, the process of FEP construction may be imagined as that below. It is well-documented [5, 11, 22] that the wavelet transform is also capable of producing an FEP by providing a frequency estimate of a signal, and we may imagine that the top branch of Fig. 2.35 could be replaced by the Morlet wavelet transform (see Goupillaud et al. [3]).

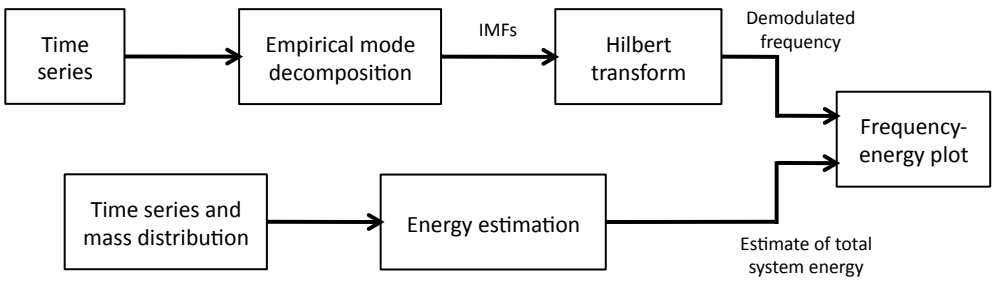

Fig. 2.35. Overview of steps to construct the FEP.

It has been shown that the EMD process generates at least one IMF, so the lingering question is which IMF frequency to plot against total energy. If the EMD properly decomposes the time series into n IMFs, we expect the dominant mode(s) of vibration to have the highest amplitude IMF(s). Referring again to the physical system described by eqs. (2.2), recall the IMFs from Fig. 2.21. The EMD algorithm finds additional IMFs—nine in total for the linear oscillator and nine for the NES—but for brevity, we have plotted just the first two IMFs generated for each. In both cases, one IMF is of significantly larger amplitude than the other, and the amplitude of the remaining IMFs is orders of magnitude smaller. Thus, while the linear oscillator may possess small components of other frequencies, its dominant mode of vibration corresponds to the frequency of the first IMF. The NES also has a high-amplitude IMF with several smaller-amplitude IMFs, and so we choose the second IMF in Fig. 2.21 to use for FEP construction. It may be that specific intervals of certain IMFs, and not just one IMF, need to be plotted on the FEP. The residual is an important part of this determination, but there is no universal rule that would suggest which IMFs to plot on the FEP for all systems, and thus, this decision should be made based on the specific IMFs being analyzed.

Using MATLAB, the procedure of plotting the frequencies against the energies is trivial after having completed the three steps, and the resulting FEP is shown in Fig. 2.36. The backbone diagram that shows in faint lines the various branches was constructed by Dr. Young Lee, and it is clear from it that the initial conditions imposed do indeed excite the system into 1:3 TRC.

To contrast the FEP constructed with the IMFs of Figs. 2.17 and 2.20, consider Figs. 2.37. (Note that the frequency of the first, rather than the second, NES IMF was chosen for the or-

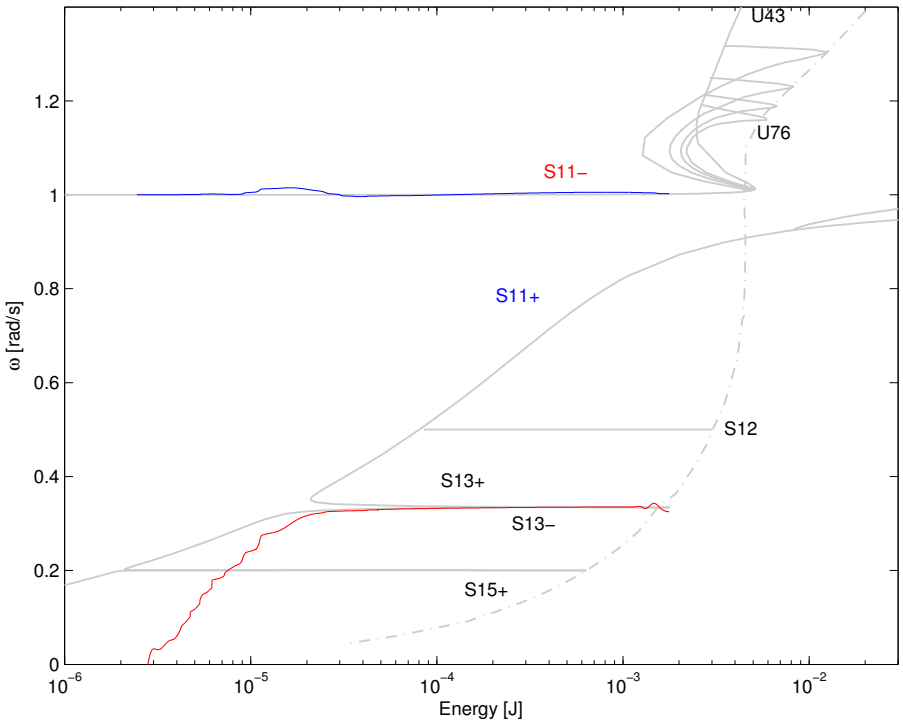

Fig. 2.36. Frequency-energy plot for the SDOF system with ungrounded NES in 1:3 TRC.

dinate axes of these plots, as this was the high-amplitude IMF generated from the standard EMD procedure.) Though the IMFs (Figs. 2.17 and 2.20) used to construct these FEPs may have seemed only slightly different from those used to construct Fig. 2.36, and the frequency and amplitude of the IMFs may have appeared qualitatively similar, the FEPs of Figs. 2.37 simply do not behave as expected. In Fig. 2.37(a), the end effects are catastrophic. Here, windowing has even been applied to try to mitigate the end effects in the IMFs used in this FEP construction: without this windowing, the large-energy end effects would be even further pronounced. (One observation is that the energy of this physical system decays with time, as evident in Fig. 2.5, so the FEP depicts increasing time from right to left. Small times have large energy; large times have small energy.) Mirroring the original time series reduces the end effects present at $t = 0$ s, and as expected, the large energy portions of the S_{13-} branch of Fig. 2.37(b) are now clean, even if the remainder of the branch is not. In each of these two plots, recall that the IMFs (Figs. 2.17 and 2.20, respectively) correctly decomposed the LO displacement but could not properly decompose the NES displacement.

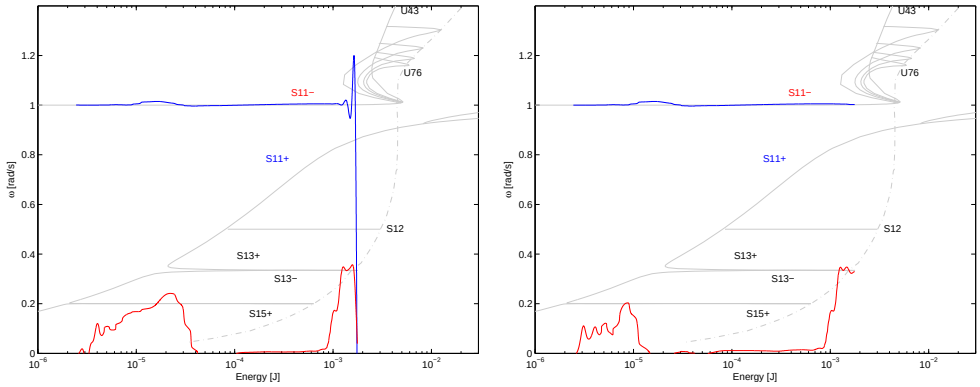

(a) FEP of IMFs of Fig. 2.17 (b) FEP of IMFs of Fig. 2.20

Fig. 2.37. FEPs constructed from improperly-decomposed IMFs. Mirroring the time series (right) only helps in removing end effects, not in amplifying the high-frequency component of the NES signal.

The final manifestation of the need to use a masking signal to correctly generate the NES IMF is shown in the clean branches of Fig. 2.36 and the unsuccessful attempt to track the S_{13-} branch of Figs. 2.37.

In Section 2.3.1, it was shown that the Hilbert transform provided a sharper estimate of a monochromatic signal's frequency and amplitude than did the wavelet transform. Increasing the resolution of the wavelet algorithm can help slightly, but the associated computational time increases significantly with a commensurate gain in resolution. Nevertheless, the natural question is still what the results of FEP construction using the one-step wavelet transform would be compared to the two-step EMD and Hilbert transform algorithm. The wavelet transforms associated with the physical system described are shown in Fig. 2.38. Plotting these frequencies against the estimated energy to construct the FEP (Fig. 2.39), we observe that the wavelet transform also tracks the appropriate S_{11-} and S_{13-} branches and does so without needing to employ a masking signal. The plot of Fig. 2.40 shows the LO FEP (left) and NES FEP (right), each plotted with frequencies calculated from the wavelet transform and EMD-Hilbert transform process. As seen in the example of demodulation, while both algorithms are able to correctly determine the monochromatic frequency, the Hilbert transform yields a much sharper frequency estimate.

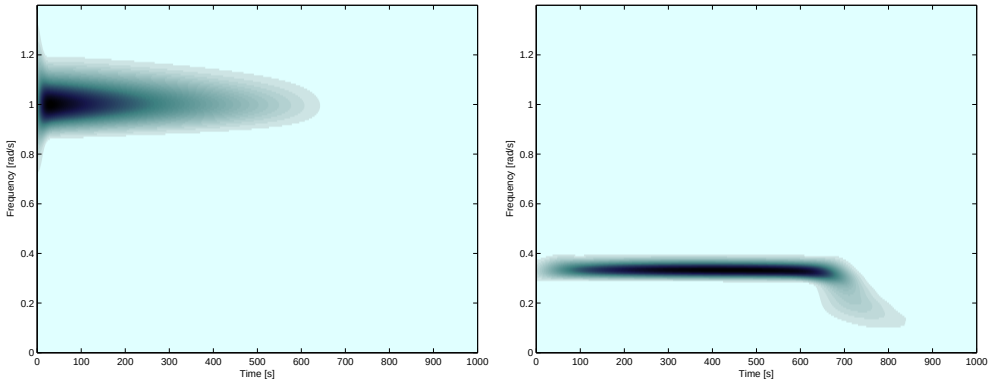

(a) LO wavelet transform (b) NES wavelet transform

Fig. 2.38. WT of the displacement time series of the system in 1:3 TRC.

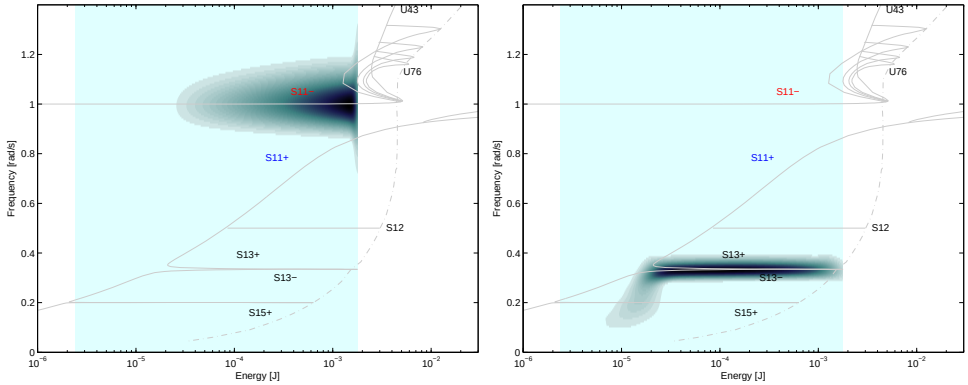

(a) FEP constructed from LO WT (b) FEP constructed from NES WT

Fig. 2.39. FEP of the LO (left) and NES (right) with frequencies estimated from the wavelet transform, which is able to track the two expected branches.

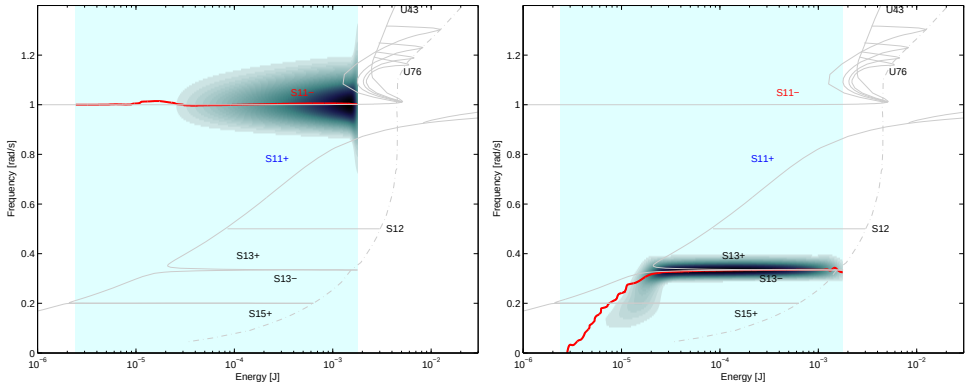

(a) LO comparison: WT and HT (b) NES comparison: WT and HT

Fig. 2.40. Comparison of the FEP of the LO and NES with frequency estimation by the WT (dark colored shapes) and the EMD-HT (red lines).

2.4.2 FEP of Impulsively-Excited System

The example SDOF system with an ungrounded NES was excited with initial conditions such that it would enter 1:3 TRC. The FEPs described in Section 2.4.1 reflect this nicely, but it can be difficult in experiment to impart individual velocities to the carts: the physical setup of the system uses a forcing on the first cart, which is most closely approximated in simulation with a velocity initial condition on the first cart, and it quickly becomes more tedious to apply velocity initial conditions to both carts. As a quick proof of concept, we take the initial energy of the 1:3 TRC system to be E_i, calculated as $E_i = \frac{1}{2}m_1\dot{y}_0^2 + \frac{1}{2}m_s\dot{v}_0^2$, where m_1 is the mass of the linear oscillator; m_s, the mass of the NES; $\dot{y}_0$, the initial velocity of the linear oscillator; and $\dot{v}_0$, the initial velocity of the NES. If we then take E_i and impart it entirely to the first cart via a velocity initial condition, we can approximate the effect of striking the cart impulsively. The resulting displacement is shown in Fig. 2.41. Clearly, the system still oscillates with a fast frequency ω_0 and some slower frequency.

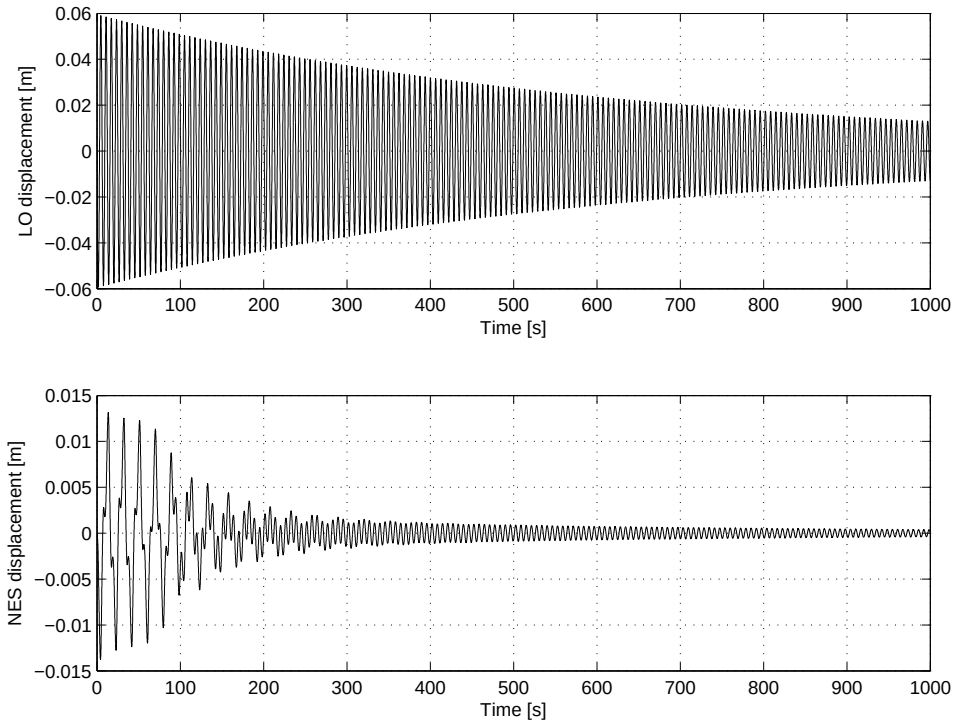

Fig. 2.41. The displacements of the impulsively excited system. The initial energy of this system is equal to that of the previous, 1:3 TRC system, but the initial conditions imposed here are those of initial velocity on only the LO.

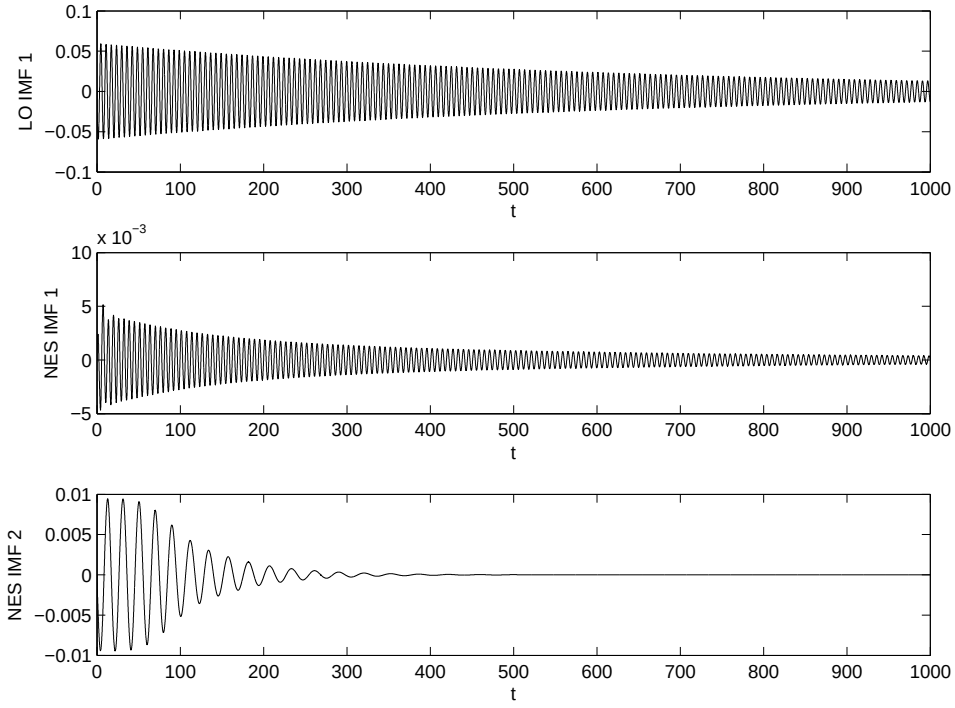

Fig. 2.42. The IMFs of the impulsively excited system.

After mirroring the time series, the IMFs obtained from the EMD algorithm are displayed in Fig. 2.42. No masking signal was required here, as the EMD algorithm was able to decompose cleanly the original signal $x(t)$. In this case, the EMD process found only one IMF corresponding to the linear oscillator displacement. The same window as in Fig. 2.33 was used in the Hilbert transform process as well; it is shown again for convenience in Fig. 2.43. The amplitude and frequency content of the IMFs can be obtained by using the Hilbert transform; the result is shown in Fig. 2.44. We show the total energy plot, Fig. 2.45, next to show the time relation of the system energy. Note that, as expected, the initial energy is identical to that of the system in 1:3 TRC. Plotting the frequencies against the total energy of the system of the first linear oscillator and second NES IMFs, respectively, yields the FEP in Fig. 2.46.

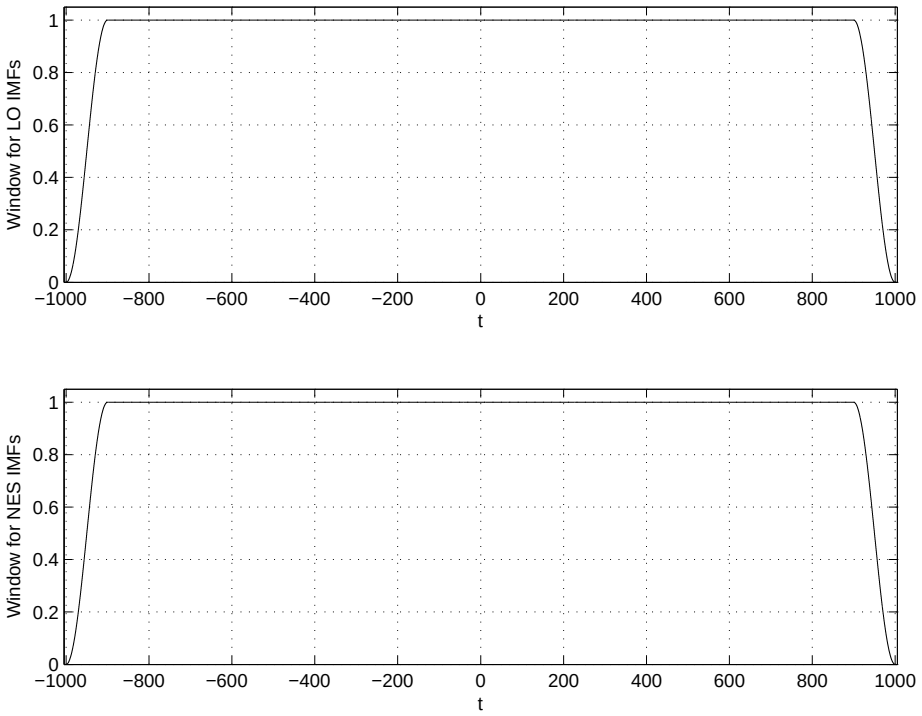

Fig. 2.43. The tapered cosine window applied to the full time interval $\hat{t}$.

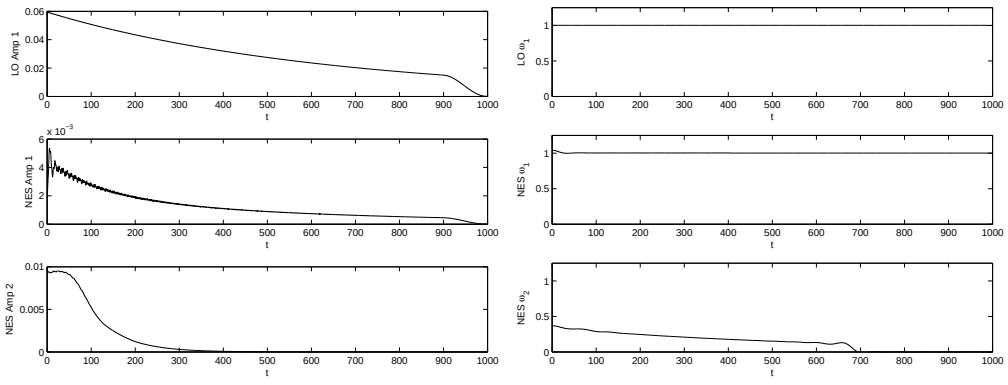

(a) Amplitude (b) Frequency

Fig. 2.44. Amplitude and frequency content of the IMFs of the impulsively excited system.

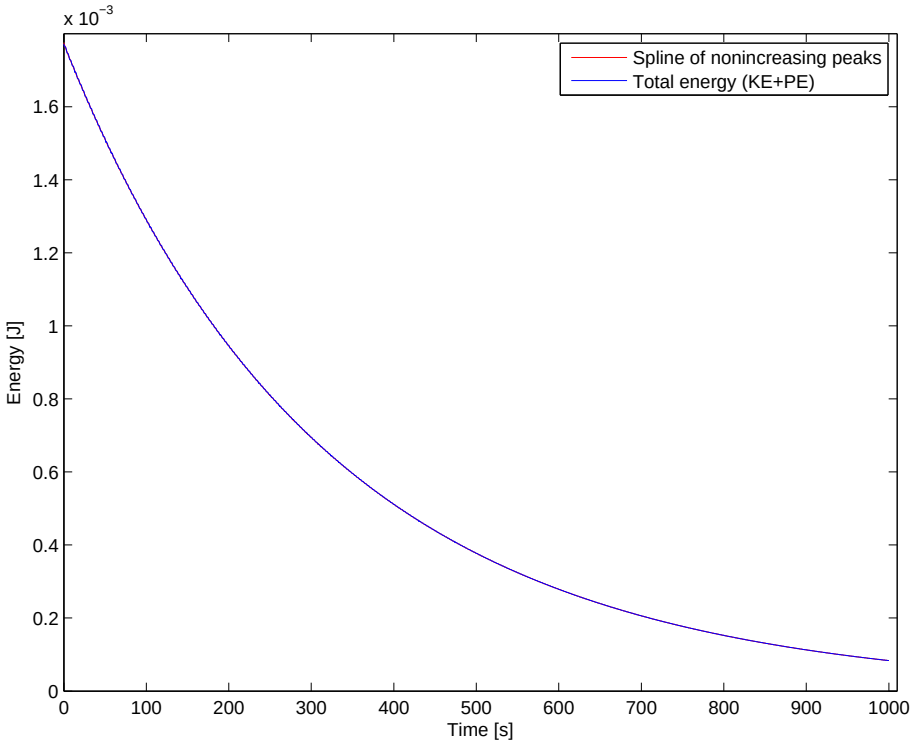

Fig. 2.45. The total energy of the impulsively excited system plotted as a function of time.

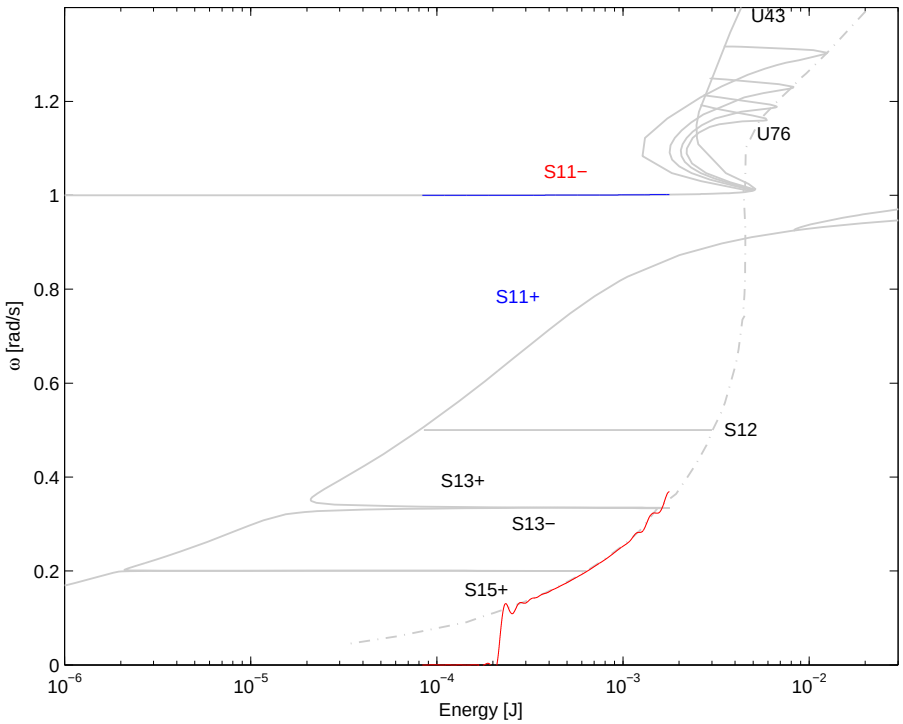

Fig. 2.46. The FEP of the system with initial velocity on only the linear oscillator.

It is clear that the system tracks the impulsive manifold of the system, and to further investigate this phenomenon, we consider the wavelet transforms of the original time series and later consider the case of a larger initial velocity. We begin with the results of the wavelet transform.

The wavelet transform of the time series yields the plots displayed in Figs. 2.47. If we overlay the FEPs from the EMD algorithm and the frequencies in the wavelet transform against the estimated energy of the system, we obtain the two plots in Figs. 2.48. It is apparent that these FEPs are qualitatively similar to the FEPs derived from the EMD process, but again, the EMD process (and specifically, the Hilbert transform) results in a FEP with much increased sharpness.

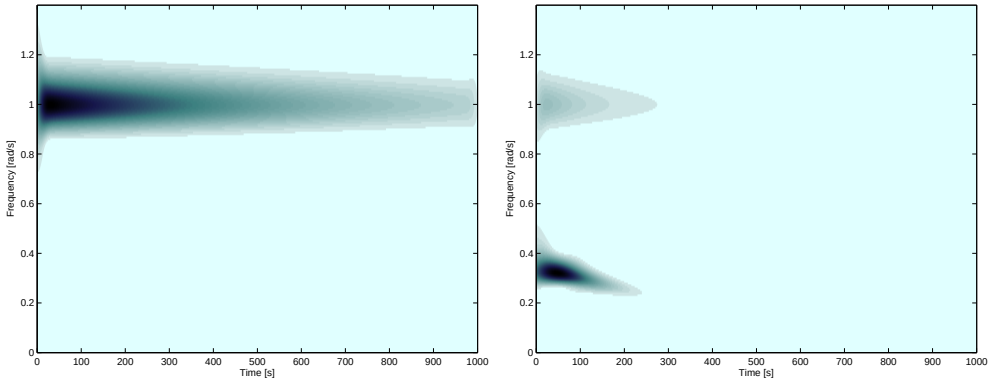

(a) LO wavelet transform (b) NES wavelet transform

Fig. 2.47. Wavelet transform of the displacement time series for the LO and NES of the SDOF system with only LO initial velocity.

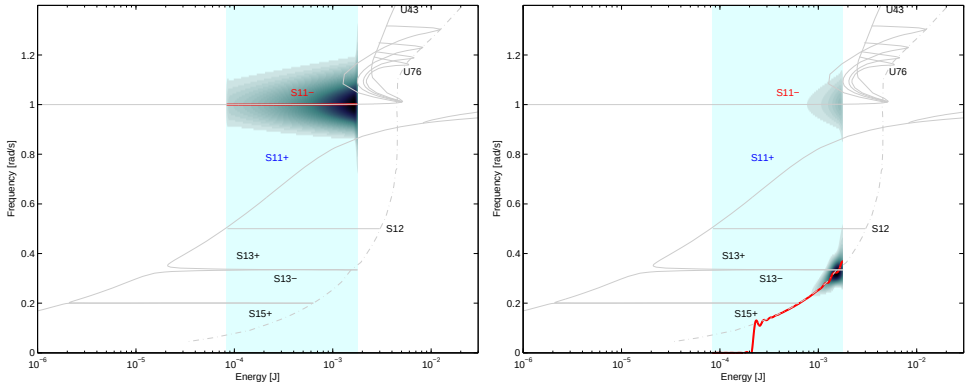

(a) LO FEP comparison: WT and HT (b) NES FEP comparison: WT and HT

Fig. 2.48. Comparison of the FEP, generated from the WT and the EMD-HT procedure, of the impulsively-excited system.

We now consider the case where the initial energy imparted to the linear oscillator is 1.5625 times that of the original initial energy from the system in 1:3 TRC (that is, this energy represents a 25% increase in the LO velocity initial condition), and the resulting displacements of the LO and NES are shown in Fig. 2.49. We will define this new initial energy as $E_{\text{new}} = 1.5625E_i$. The IMFs generated, Fig. 2.50, are qualitatively similar to those depicted in Fig. 2.42. Here, again, the original signal was mirrored, and no masking signal was used to produce the IMFs. From these IMFs, we can generate the FEP after applying the Hilbert transform algorithm. (The same tapered cosine window as that in Fig. 2.43 was used here as well.) The frequency and amplitude of the IMFs are shown in Figs. 2.51, and the estimated and actual total energy of the system is shown in Fig. 2.52. The resulting FEP is plotted in Fig. 2.53. The wavelet transforms of the displacement time series corresponding to this higher-energy excitation are shown in Fig. 2.54. Finally, the FEPs of the LO and NES, each generated from both the WTs of Fig. 2.54 and those generated from the EMD-HT process, are overlaid in Fig. 2.55.

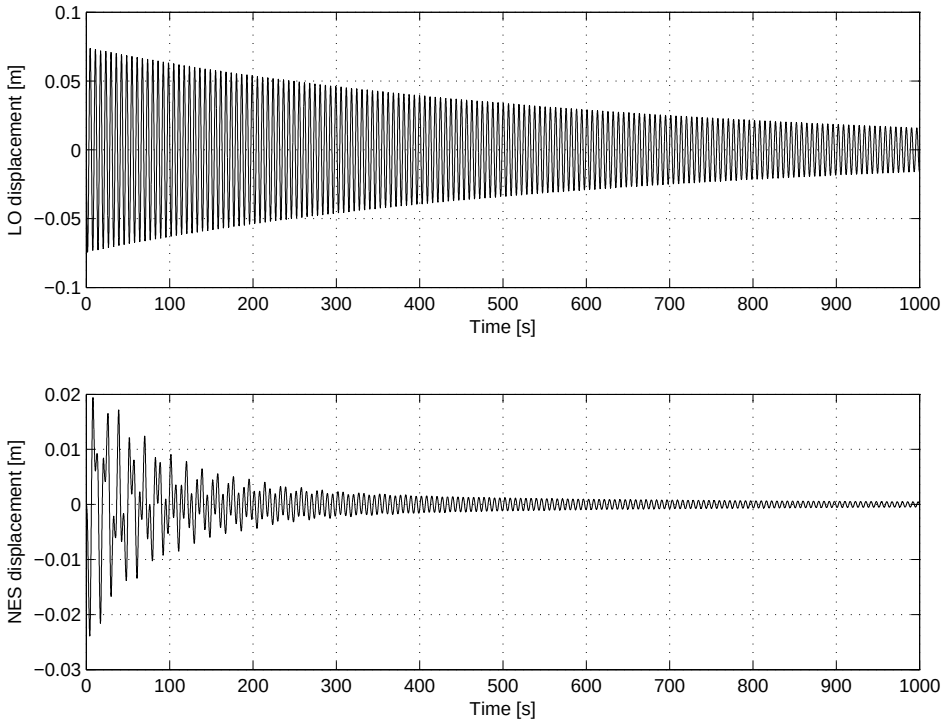

Fig. 2.49. The displacements from the impulsively excited system with velocity initial conditions on the LO such that the initial energy is E_{new}.

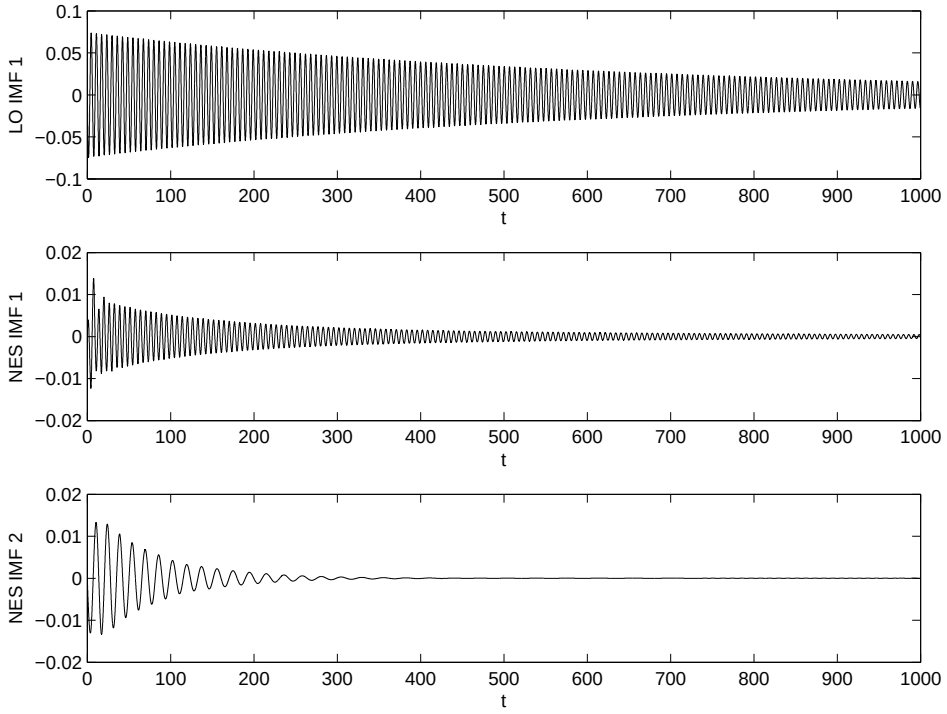

Fig. 2.50. The IMFs of the system with initial energy E_{new}.

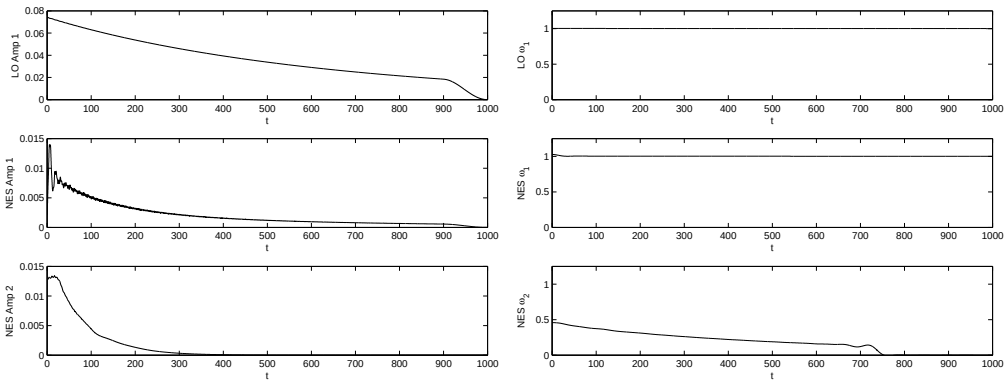

(a) Amplitude (b) Frequency

Fig. 2.51. Amplitude and frequency content of the IMFs corresponding to the impulsively excited system with initial energy E_{new}.

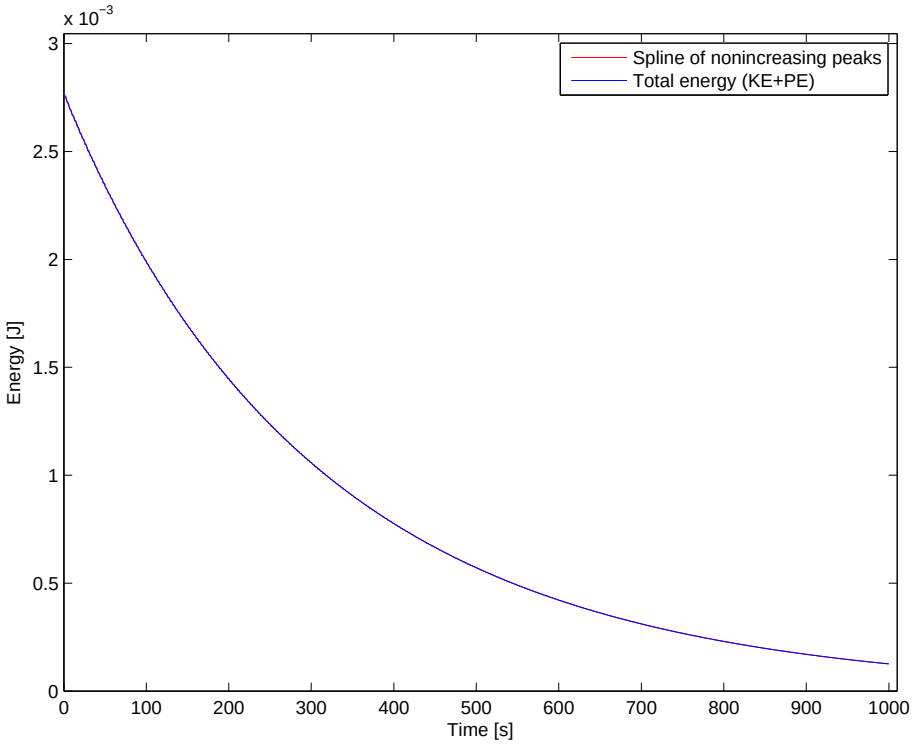

Fig. 2.52. The total energy of the system with initial energy E_{new}.

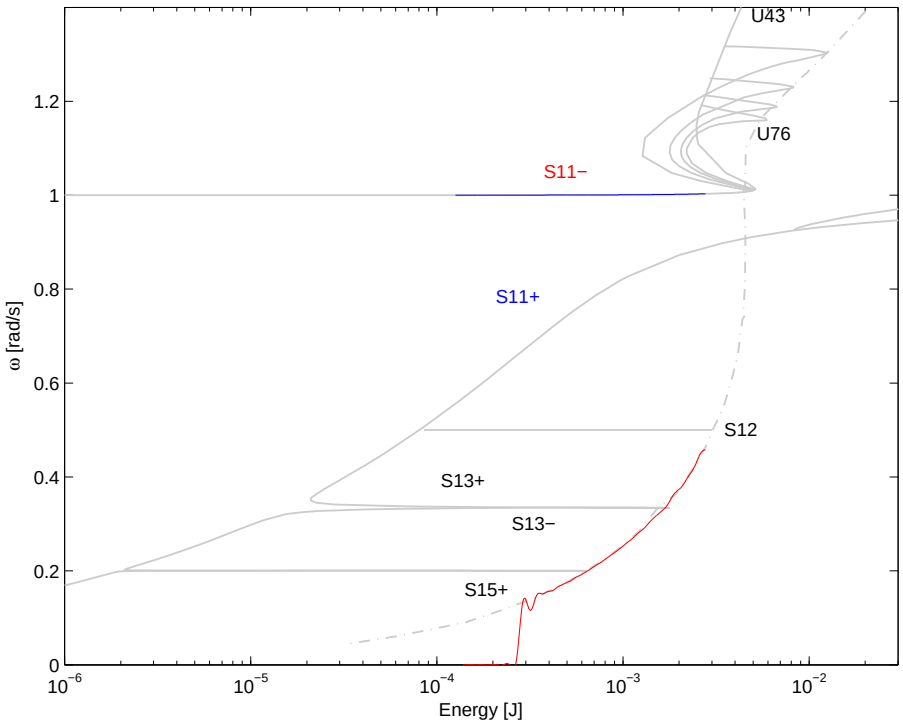

Fig. 2.53. The FEP of the system with linear oscillator initial velocity and initial total energy E_{new}.

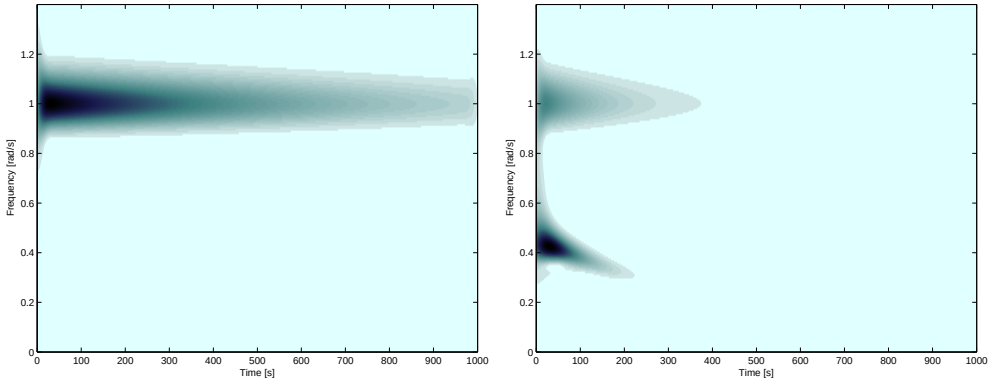

(a) LO wavelet transform (b) NES wavelet transform

Fig. 2.54. Wavelet transforms of the time series for the LO and NES with initial total energy E_{new} applied to the linear oscillator.

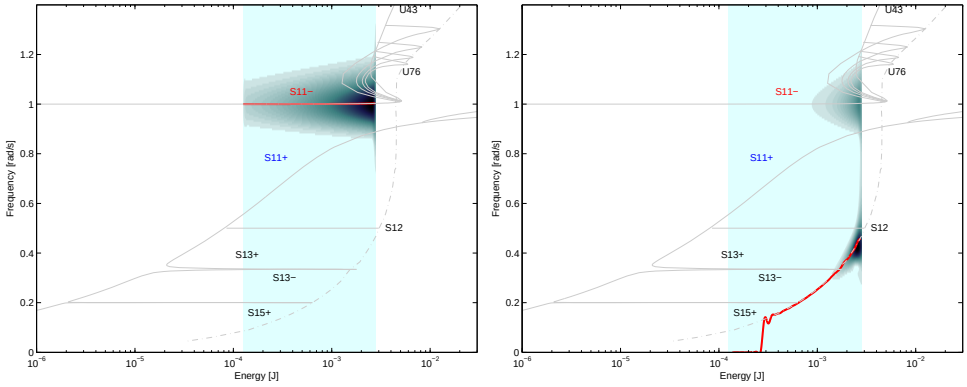

(a) LO FEP comparison: WT and HT (b) NES FEP comparison: wavelet and Hilbert transform

Fig. 2.55. Comparison of the FEP generated from the wavelet transform and the EMD-Hilbert transform procedure for the case of initial energy E_{new}.

It is clear that the behavior of the system for initial conditions corresponding to both E_i and E_{new} is similar, and the FEP results from both methods show this agreement. The ability of the procedure described for FEP construction to plot the FEP quickly is thus largely evident. This phenomenon of impulsive-orbit tracking had not previously been observed. Kerschen et al. [5] note that passive TET properties largely motivate the analysis of impulsive manifold tracking, but the details have not yet been fully investigated. With this method for FEP construction, we have shown that with certain initial conditions, it is possible to track the impulsive manifold and not just the expected S_{11^-} branch.

2.5 Summary of FEP Construction Algorithm

We have outlined the process for FEP construction with knowledge of a system's mass distribution and velocity time series in four steps, which are to:

1. Estimate the total energy by picking the nonincreasing peaks of the kinetic energy.
2. Use the EMD algorithm to generate IMFs.
3. Apply the Hilbert transform to the IMFs to estimate the frequencies of the IMFs.
4. Plot these frequencies against the estimated energies of step 1 to construct the FEP.

Chapter 3

Application of FEP Algorithm to Simulation and Experimental Data

This chapter first describes the experimental procedure and hardware used and then documents the construction of the FEP for a variety of configurations. The corresponding FEPs constructed from simulation data with parameters matching those of the experimental systems are also demonstrated. Throughout, the same three-step procedure for FEP construction discussed in Section 2.4 will be followed. Finally, some of the intricacies of post-processing this sort of data will be examined in detail, as the ramifications of these issues is readily apparent in the final FEP.

3.1 Experimental Hardware

The experimental data used in this work were obtained by a former student in the Linear and Nonlinear Dynamics and Vibrations Laboratory (LNDVL), Mr. Jeffrey Kowtko. The specifics of the experimental arrangement can be found in his thesis [8], but we begin with a brief overview of the experimental setup. Once again, we consider the single-degree-of-freedom system with an ungrounded NES. This arrangement is depicted schematically in Fig. 3.1. The equations of motion with constants reflecting those shown in Fig. 3.1 are

$$m_1\ddot{y} + k_1 y + c_1\dot{y} + c_s(\dot{y} - \dot{v}) + k_s(y - v)^3 = F(t), \tag{3.1a}$$

$$m_s\ddot{y} + c_s(\dot{v} - \dot{y}) + k_s(v - y)^3 = 0. \tag{3.1b}$$

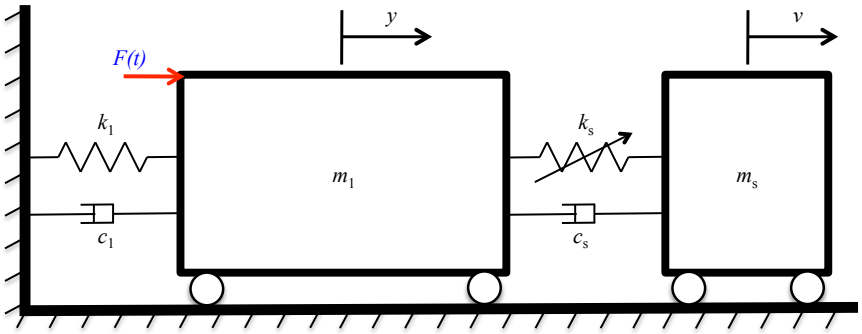

Fig. 3.1. The experimental 2-DOF system with cubic nonlinearity.

The right-hand side of eq. (3.1b) reflects the impulsive excitation to the system and does not suggest that a periodic force throughout the entire time interval was applied to the primary mass. In order to remove frictional effects (which introduce unadjustable and hence undesirable damping terms), the two carts were crafted out of 90-degree angle blocks; the underside of the carts rests on an angled aluminum air track. The air track and the cart are shown in Fig. 3.2. Pictures of the experimental setup are used with permission from Kowtko [8], but some images have been edited. The air track itself is effectively a section of square stock with small holes along two adjacent faces. The face detail of the track is shown in Fig. 3.3. The entire system from an iso-perspective is presented in Fig. 3.4. Fig. 3.5 labels each component and illustrates the proportion of mass to each oscillator for simulation purposes. The dashpot used to damp the motion of the NES is an Airpot model 2KS56. Specifications for this dashpot are shown in Appendix D of Kowtko [8]. A close up of the dashpot is pictured in Fig. 3.6. The NES comprises the steel shaft, connecting hardware, and two steel plates clamping the piano wire. It is the piano wire that introduces the geometric nonlinearity discussed in Section 1.2. Two accelerometers were used to capture the motion of the carts. The system was excited with a long-stroke shaker; the stinger of the shaker struck the linear oscillator. For quick trials, an impulse hammer is sufficient, but certainly repeatability and precise force application become more difficult with this mode of force application.

A brief discussion of data acquisition tools is pertinent here. The data acquisition boxes used by Jeff Kowtko were two Spectral Dynamics SigLab dynamic signal analyzers. Additional information is available in his thesis [8], but we point out that it is now possible

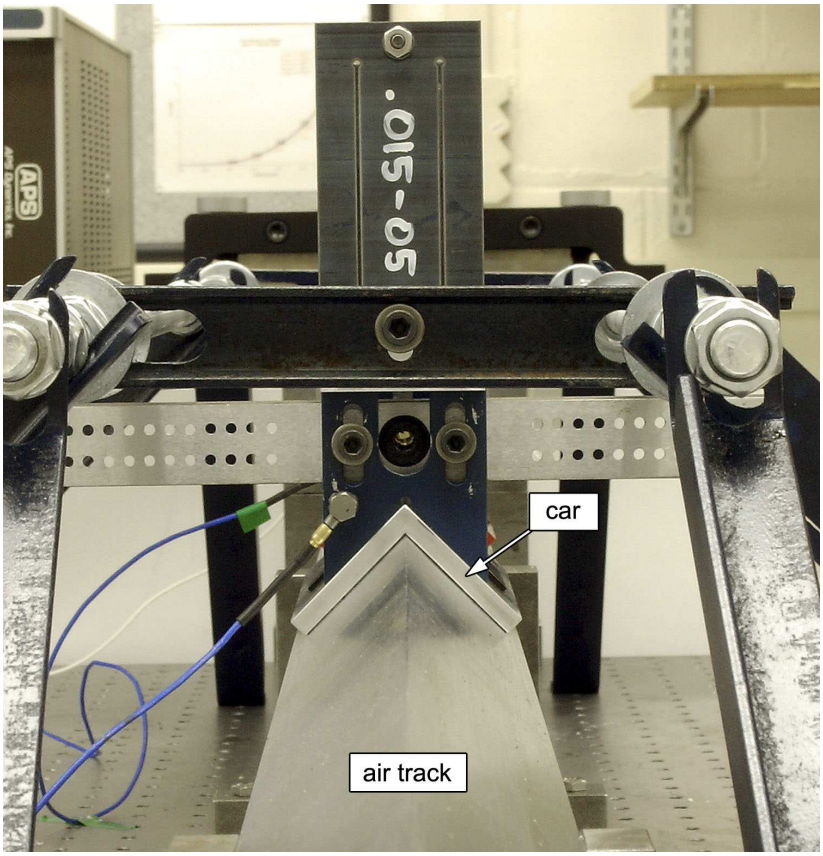

Fig. 3.2. Longitudinal view of the air track and cart [8].

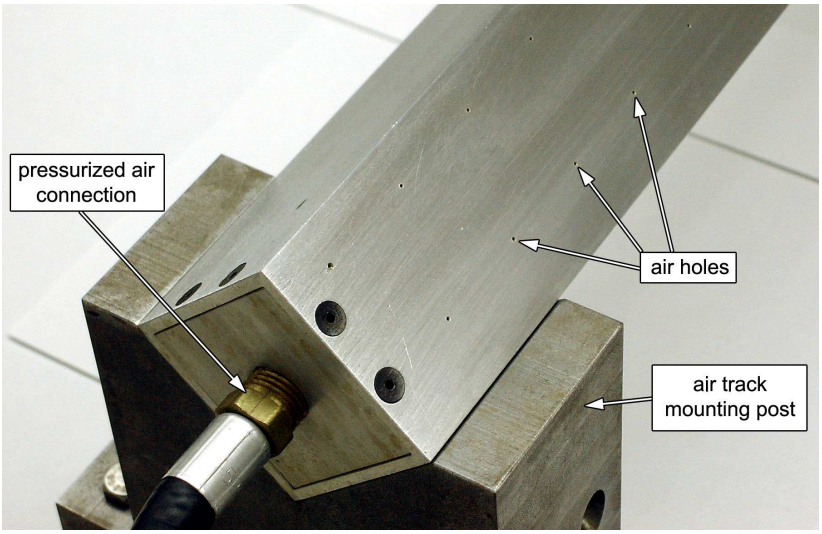

Fig. 3.3. Surface detail of the air track [8].

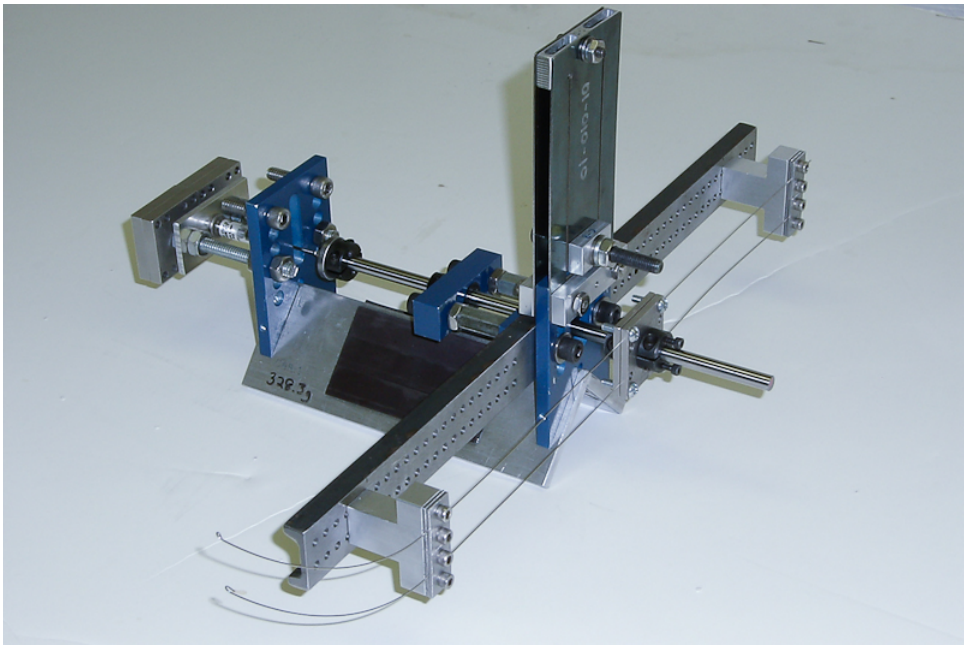

Fig. 3.4. An iso-view of the experimental system [8].

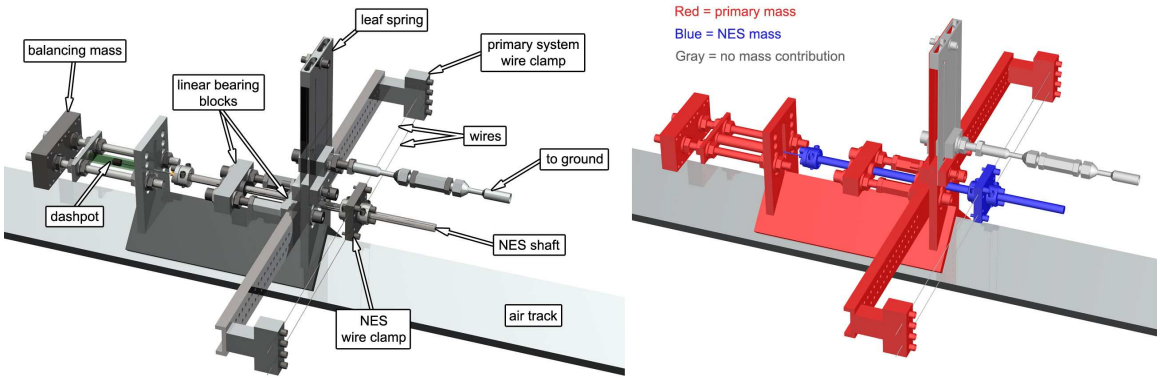

Fig. 3.5. An iso-view of the schematic of the experimental system. The figure at right depicts the mass distribution of the hardware [8].

to gather eight channels of information in a single box (previous efforts required "daisy-chaining" together the two boxes [8]). Current tools, such as those produced by M+P International and two examples of which are currently used in the LNDVL, are commercially available and offer a corresponding software suite that interfaces with those products. Data export in MATLAB's `.mat` format is also possible, and data processing tools, including a built-in frequency-response function (FRF) generator, are also included.

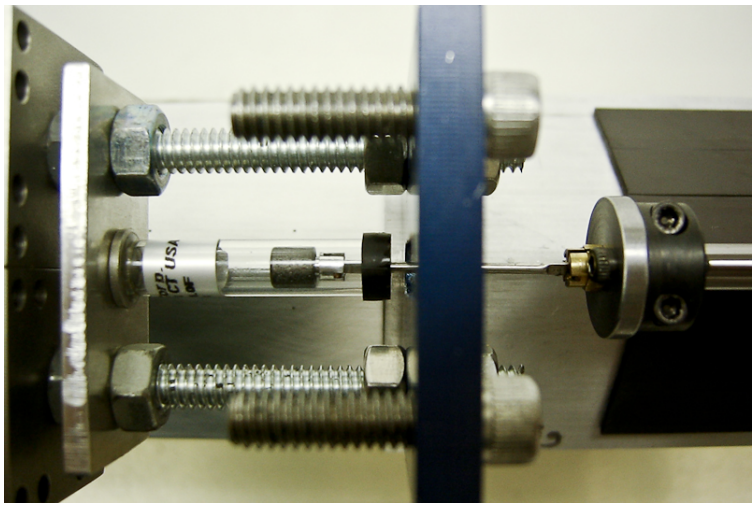

Fig. 3.6. The dashpot connecting the NES and the linear oscillator [8].

Regardless of the choice of data acquisition hardware or software, for the experiments described herein it is important to remain cognizant of the effects of sampling frequency. Although the data collected with a higher sampling frequency will be understandably noisier, a sampling frequency of at least 512 Hz is typically required to capture fully the impact. In some of the author's experiments, the impact duration was sufficiently brief that a sampling frequency appropriate for capturing the cart's motion—128 Hz is more than sufficient to capture the dynamics of the system—actually aliases the hammer force signal, resulting in a force profile that was lower in magnitude than the actual force striking the system. With this overview of the experimental arrangement, we now proceed to discuss the data processing and construction of the resulting FEP.

3.2 Constructing the FEP from Time-Series Data

In the first case, we will present several intermediate steps prior to showing the FEP itself in order to showcase any nuances that arise during the algorithm. (The experimental data and certain figures presented here are used with permission from Kowtko [8].) In subsequent cases, we will proceed more quickly. In this section, we will present the FEP construction with little discussion of post-processing subtleties; discussion of challenges and possible resolutions are discussed afterwards in Section 3.2.4.

3.2.1 Case I: 45 N Excitation Force

The system parameters for this configuration are shown in Table 3.1.

Parameter	Value
m_1 [kg]	1.266
m_s [kg]	0.14
k_1 [N/m]	1143
k_s [N/m$^{2.8}$]	1.42×10^6
c_1 [N/m/s]	0.13
c_s [N/m/s]	0.30

Table 3.1. Parameters for the nonlinear model of eq. (3.1); data from Kowtko [8].

The force used to excite the system is plotted in Fig. 3.7. The resulting measured accelerations of the linear oscillator and NES are quite noisy, so a low-pass filter with cutoff frequency of 128 Hz was applied to the data. The resulting signals, with the LO in the left plot and the NES in the right, are compared to the original signal in Figs. 3.8. Note that this data has been largely presented in Kowtko [8]; we are presenting it here as an introduction to the overall signal processing scheme required to generate the FEP from experimental time series. The next figure shows a comparison of the filtered acceleration data and the results from the MATLAB simulation. The Newmark integration scheme was used in Kowtko [8], but the agreement between the results of that calculation and the one provided by the `ode45` solver is excellent—it is impossible to distinguish the two results at normal resolutions, and the maximum difference between the two solutions is of the order 10^{-2} m/s^2 with an average difference of order 10^{-5} m/s^2.

The measured accelerations were integrated twice to obtain the displacements of the two carts. There is good correlation between the simulation and experimental results, suggesting that the parameters identified are accurate and that the simulation model itself is robust. The quicker decay of the experimental system suggests that the linear damping model assumed in the simulation may not actually be fully accurate in describing the experimental system, but the displacements are nevertheless comparable for the majority of the duration. Although it is standard practice to plot the displacement of each cart, it is also sometimes useful to plot the relative displacement, $x_{\text{rel}} = y - v$, of the carts and to construct the FEP using this new variable.

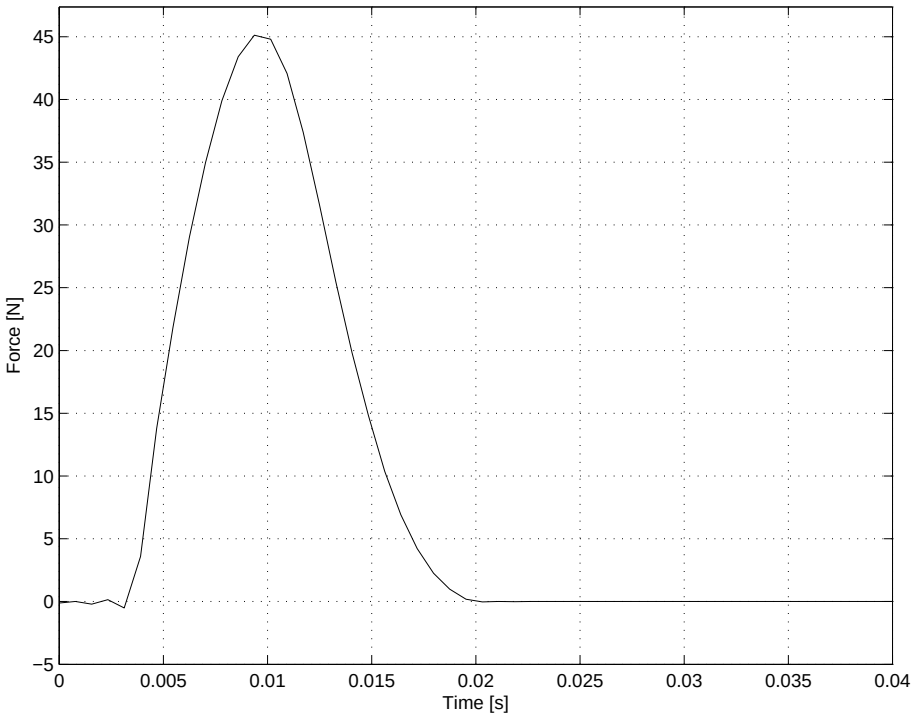

Fig. 3.7. The forcing, plotted versus time, applied to the physical system.

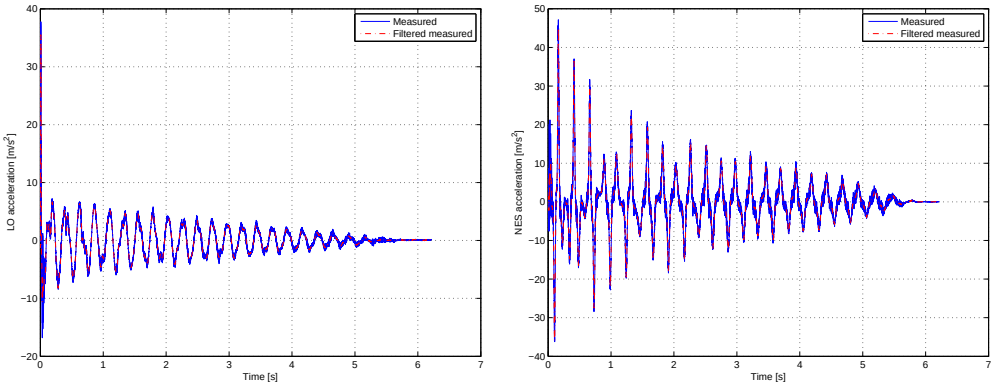

(a) LO (b) NES

Fig. 3.8. A comparison of the measured (raw) and filtered acceleration data.

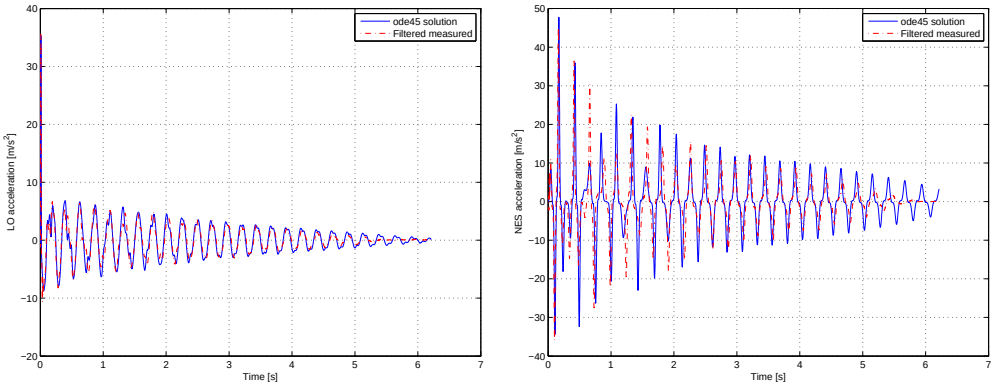

(a) LO (b) NES

Fig. 3.9. The simulated (blue) and filtered accelerations from experimental data (red) agree.

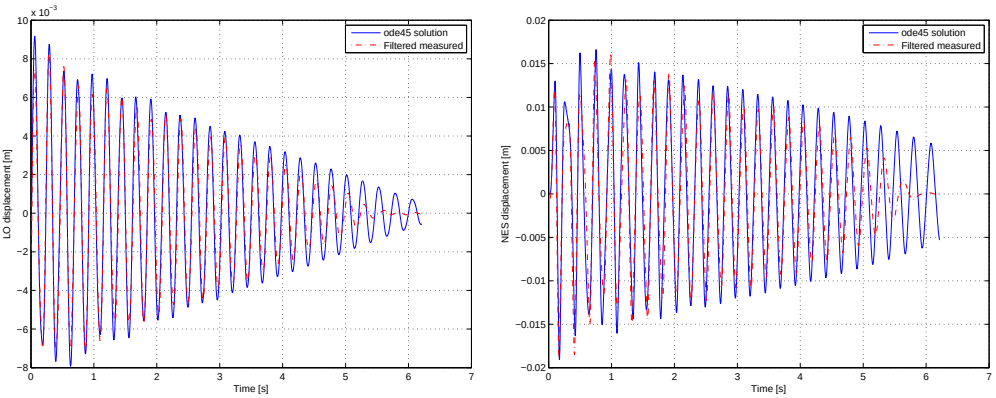

(a) LO (b) NES

Fig. 3.10. With appropriate filtering (see Section 3.2.4), the simulated (blue) and experimental (red) displacements match closely.

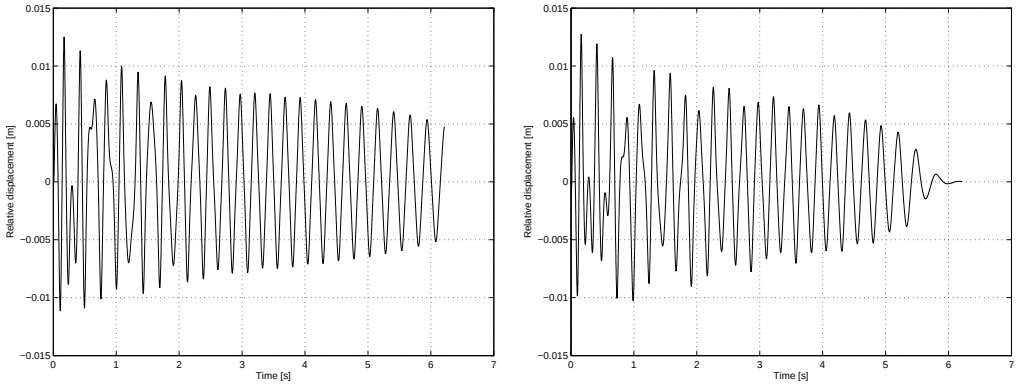

(a) Simulation (b) Experimental

Fig. 3.11. The relative displacement is the difference in displacement of the LO and NES.

We now discuss the total energy estimation. The energy in the system should be a monotonically-decreasing function of time, and the simulation data shows this nicely. Although the total energy is not quite as smooth in the experimental results, the energy there is largely still nonincreasing. Applying the nonincreasing-peaks algorithm to the kinetic energy history, we can estimate the total energy of the system. The picked peaks and spline fit to them are shown in Fig. 3.14. The actual total energy, calculated by summing the potential and kinetic energies, can be compared to the estimated total energy from the spline of the previous figure.

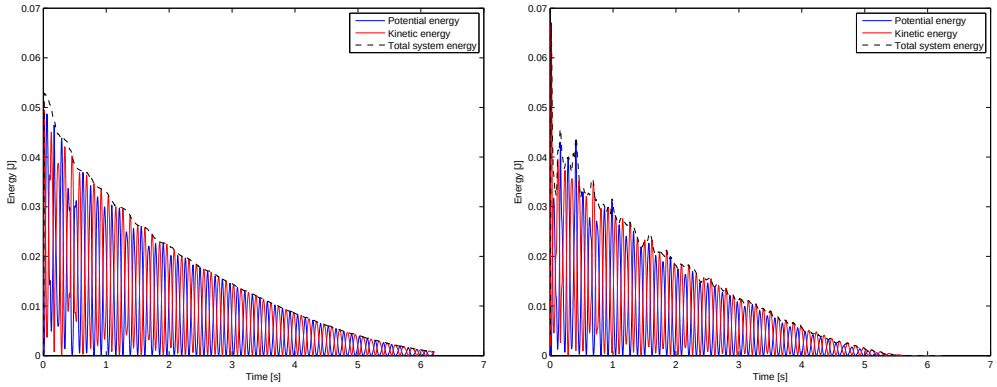

(a) Simulated (b) Experimental

Fig. 3.12. The potential, kinetic, and total energies as simulated (left) and calculated from experimental results (right).

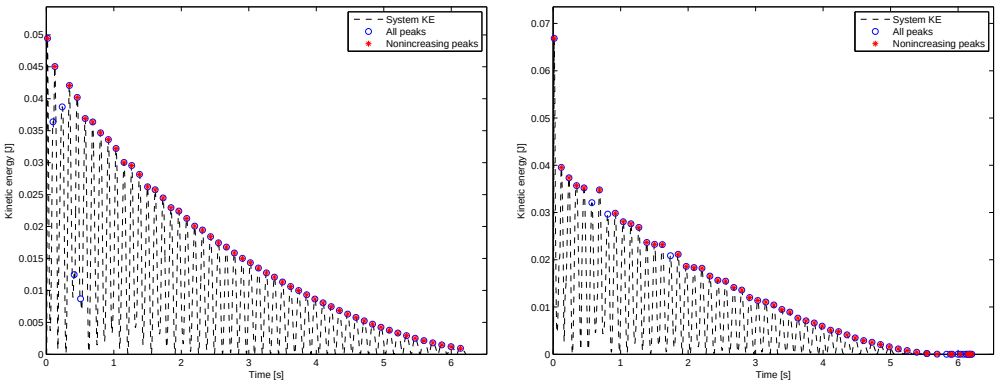

(a) Simulated (b) Experimental

Fig. 3.13. The kinetic energies, all peaks (circled), and the nonincreasing peaks (asterisks). The total energy estimated by the spline fitted to the nonincreasing peaks should be strictly decreasing.

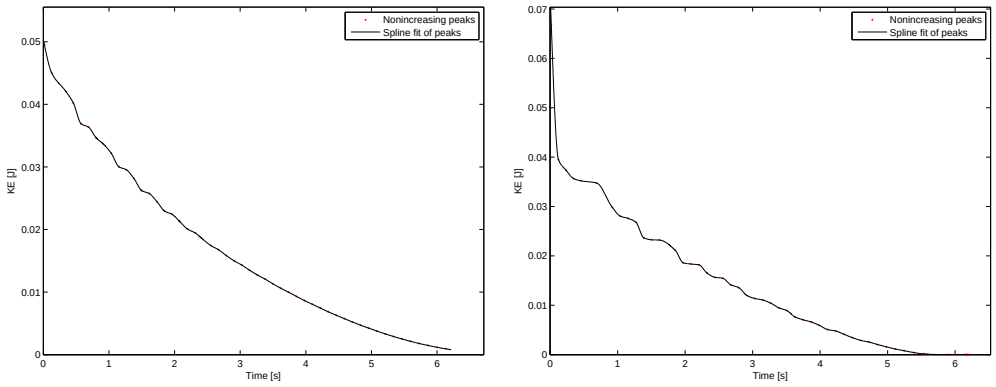

(a) Simulated (b) Experimental

Fig. 3.14. A spline is fitted to the nonincreasing peaks of the kinetic energy time series to estimate the total energy.

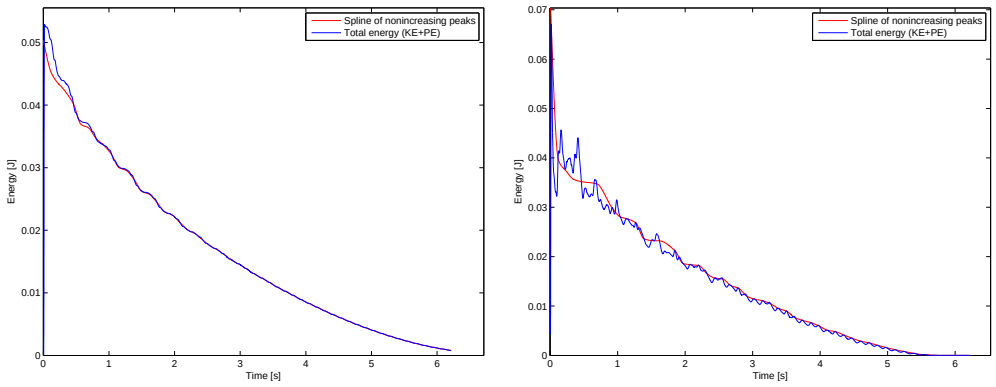

(a) Simulated (b) Experimental

Fig. 3.15. The estimated total energy is also a monotonically decreasing function of time with good agreement with the calculated total energy.

Next, we apply the EMD algorithm to estimate the frequencies plotted on the ordinate axis of the FEP. As in the previous chapter, the signal was mirrored with an odd mirror in order to introduce continuity and differentiability near $t = 0$ s. It seems from the experimental data that there is a rather large discontinuity at $t = 0$, but this gap reflects the lack of two points—one corresponding to the mirrored signal and another corresponding to the original, positive-time signal—at $(0, 0)$. When plotting the mirrored signal alone, the line connecting its discrete data points thus stops at one index prior to $t = 0$. Two of the IMFs of the LO and NES displacement generated from the EMD algorithm with no masking

signal are shown below. The IMFs produced (Fig. 3.18) are acceptable for use later in the Hilbert transform and their sum does reproduce the respective LO or NES displacement.

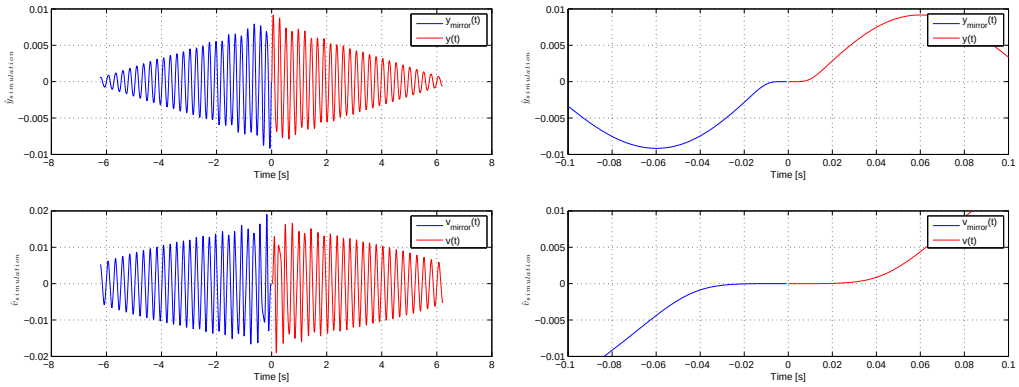

(a) Simulated: mirrored $y(t)$, $v(t)$ (b) Simulated: mirrored $y(t)$, $v(t)$ near $t = 0$

Fig. 3.16. The simulated signals $y_{\text{sim}}(t)$ and $v_{\text{sim}}(t)$ were mirrored about the origin.

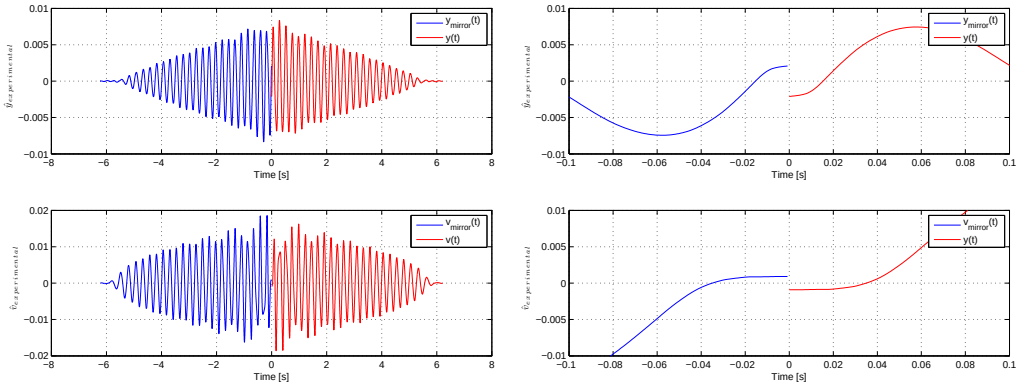

(a) Experimental: mirrored $y(t)$, $v(t)$ (b) Experimental: mirrored $y(t)$, $v(t)$ near $t = 0$

Fig. 3.17. The experimental signals $y_{\text{exp}}(t)$ and $v_{\text{exp}}(t)$ were mirrored about the origin to introduce smoothness at $t = 0$ s.

The Hilbert transform was used next to extract the amplitude and frequency content of the IMFs. In order to produce the frequency and amplitude estimates, a tapered cosine window (Fig. 3.19) was utilized to help reduce end effects, and a low-pass filter with cutoff frequency 2 Hz was chosen to reduce the ripple in the resultant frequency. Further discussion of the choice of this frequency is postponed until Section 3.2.4. The results are shown first for simulation data (Fig. 3.20) and then for experimental data (Fig 3.21). It is generally clear from Figs. 3.20(b) and 3.21(b) that the system exhibits 1:1 resonance capture; that is,

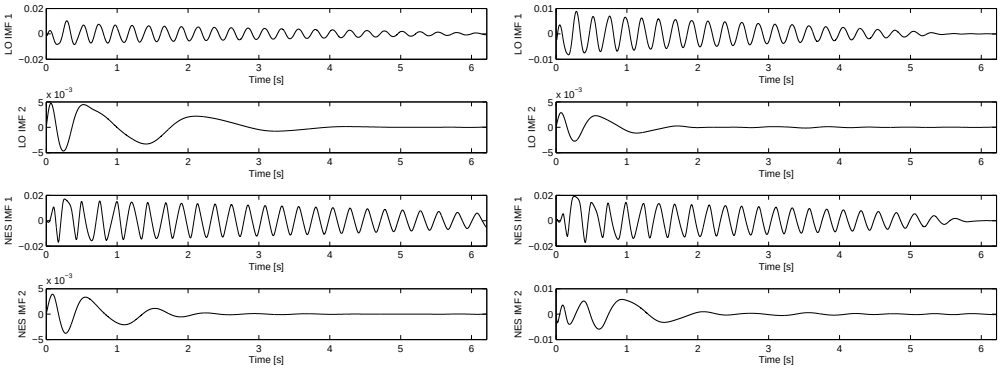

(a) Simulation (b) Experimental

Fig. 3.18. The EMD analysis yields IMFs that seem generally well-behaved.

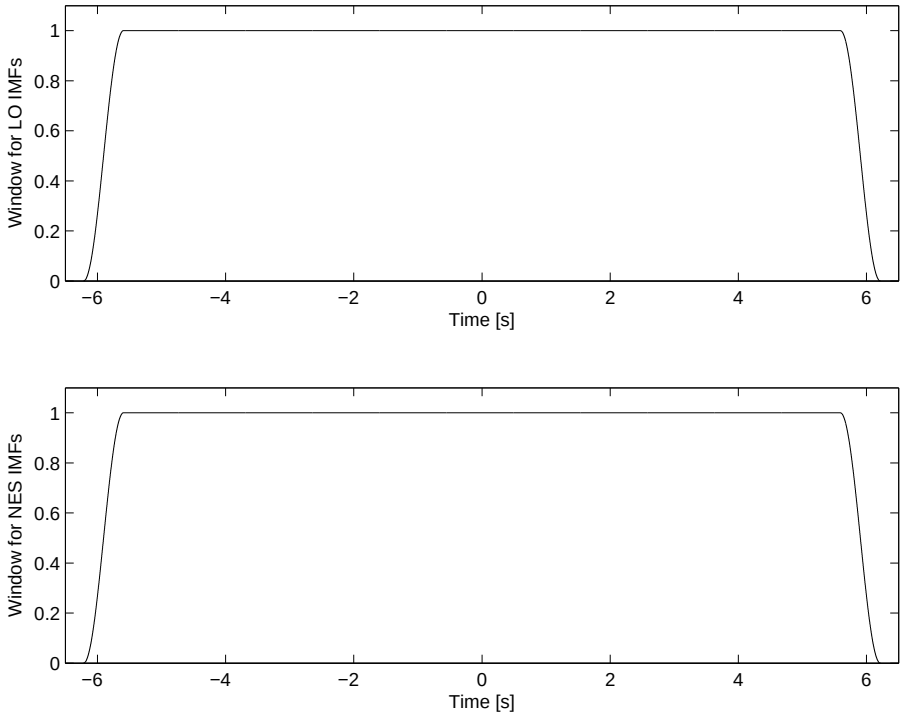

Fig. 3.19. A tapered cosine window was used to help mitigate end effects.

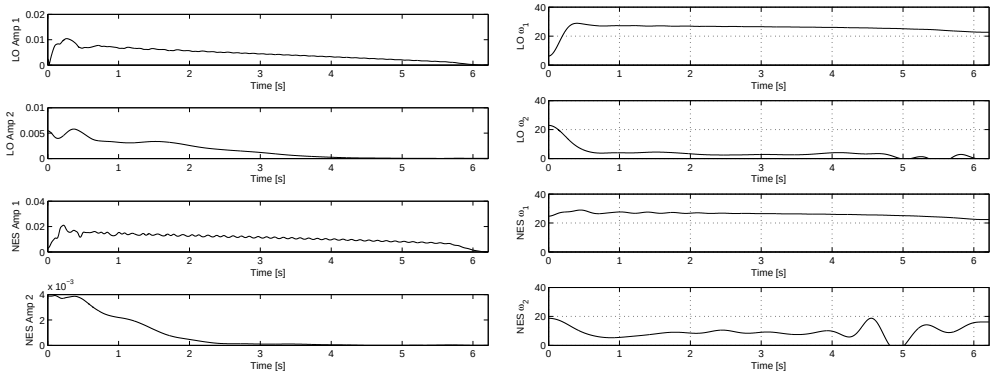

(a) Amplitude (b) Frequency

Fig. 3.20. The amplitude (a) and frequency (b) of the IMFs produced from simulation data.

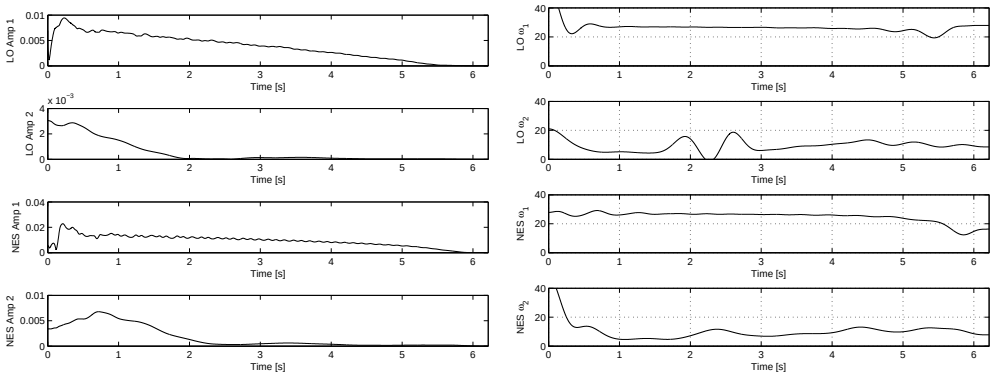

(a) Amplitude (b) Frequency

Fig. 3.21. The amplitude (a) and frequency (b) of the IMFs produced from measured data.

that the NES has "tuned" its resonant frequency to match that of the LO. (The frequency of the first LO IMF appears to be roughly equal to that of the first NES IMF. Whether they are in fact identical will be revealed in the FEP.) Due to the essential nonlinearity, and unlike linear system dynamics, the NES does not have a preferred natural frequency and instead engages in $n : m$ internal resonance with the LO. Though this system seems to oscillate with 1:1, in-phase motion, initial conditions can be tuned to excite the other modes, as demonstrated in the FEP construction of the previous chapter. The IMFs and their amplitude and displacement are plotted in Fig. 3.22 for the relative-displacement time series.

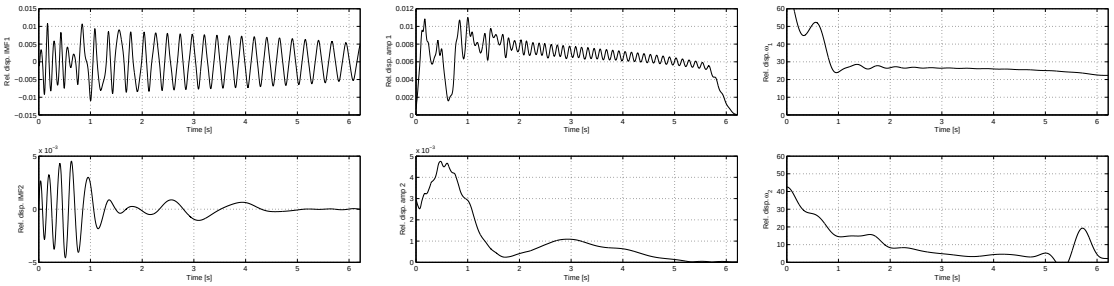

(a) IMFs (b) IMF amplitude (c) IMF frequency

Fig. 3.22. The first two IMFs (top and bottom rows, respectively) and their corresponding amplitude and frequency of the relative displacement time-series differ slightly from those of the pure displacements (Figs 3.11).

The frequencies can now be plotted against the estimated energies of Fig. 3.15 to construct the FEP. For these plots, the first n points of the frequency vector were ignored: recall from Fig. 3.20(b) that, at small time, the frequency of the first LO IMF ramped up from 0. We would expect, however, that the system would oscillate with a constant frequency for nearly all time. The lack of a constant frequency is depicted in the FEP as a long tail at high energies. To mitigate this effect, which is not indicative of motion along the S_{11} branches, these data points were discarded. Though there is no immediately clear explanation for this physically, and although there is no obvious indication in the IMF amplitude plots that a masking signal would help, additional investigation of the best way to clean up IMFs of short-duration signals is strongly recommended. No Hamiltonian backbone curve was created for the physical system at the time of writing; this is potentially an area for future consideration as well. Although Fig. 3.24 is not as clean as Fig. 3.23, it is still evident that the system is engaged in 1:1 resonance capture. The results here thus match qualitatively with the observations made in Kowtko [8].

Because the FEP does not show time explicitly, it can be difficult to judge the time behavior of a system just by studying it; an indication of time progression is helpful. In the next plot, the time corresponding to a specific (f, E) pair is marked with a dashed line. The time duration between consecutive dashed lines is equal to 1 s, so there are roughly six or seven time "snapshots" visible in the FEPs.

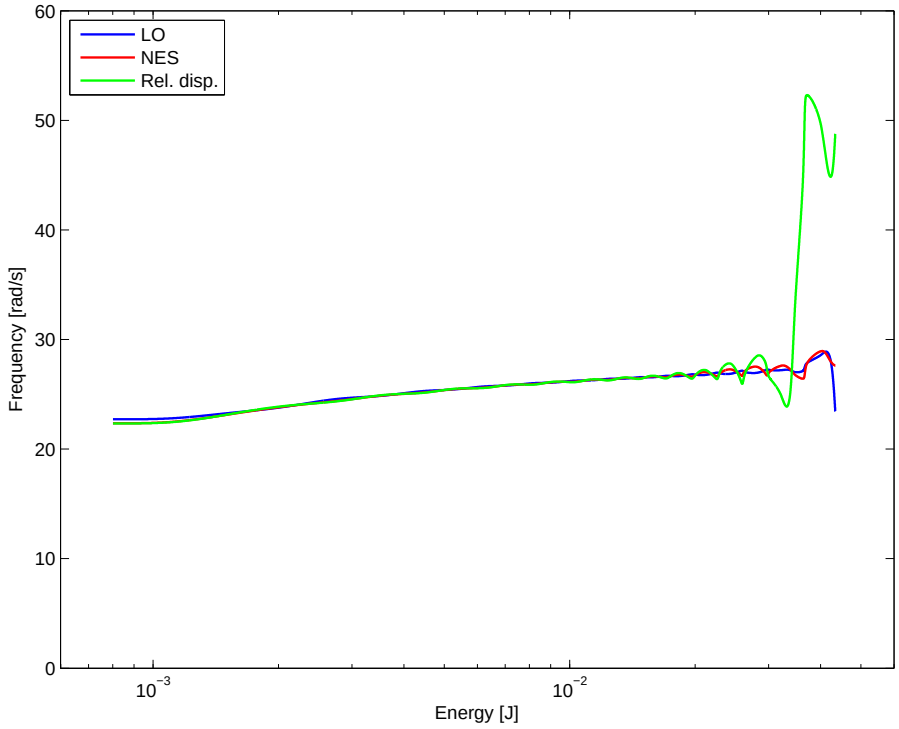

Fig. 3.23. The FEP produced from simulation data shows the clear 1:1 internal resonance between the LO and NES.

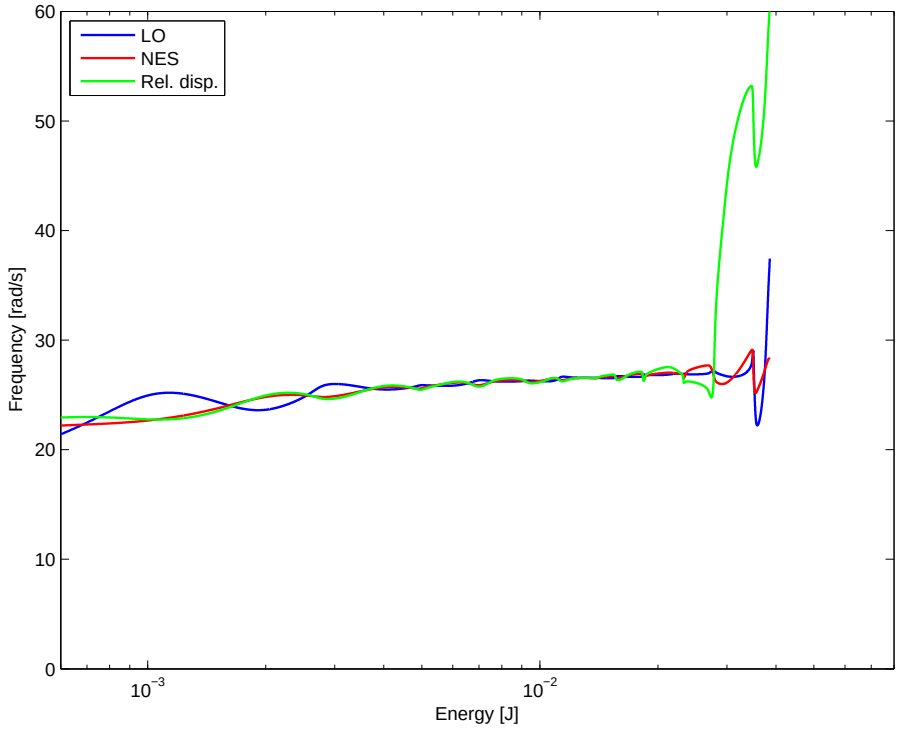

Fig. 3.24. The FEP produced from experimental data also tracks the 1:1 resonance between the LO and NES.

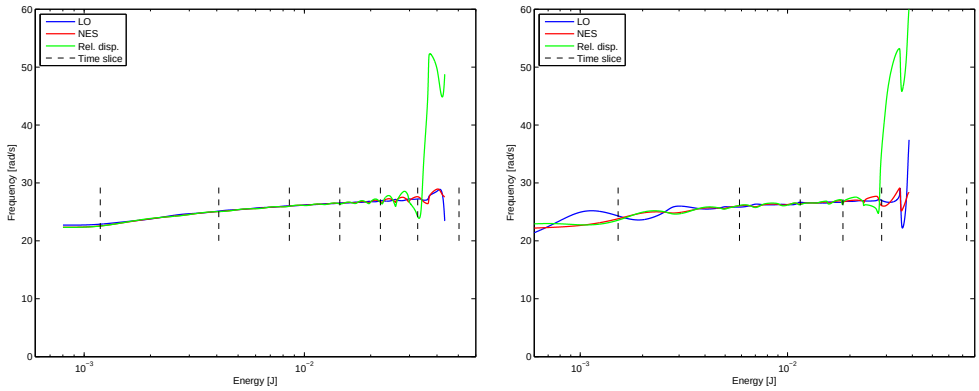

(a) Simulation (b) Experimental

Fig. 3.25. The spacing between dashed lines represents a one second interval.

For completeness, we also present the wavelet transforms of the displacement data (Figs. 3.26) and the FEP generated from that procedure (Figs. 3.27). The two algorithms should reveal the same information, of course, and that comparison is made in Figs. 3.28. There are two comments about the generation of these wavelet transforms. First, because the experimental displacements go to near-zero, the total energy of the system becomes effectively zero. Practically, this results in a blank figure when the MATLAB command `set(gca, 'XScale', 'log')` is used in conjunction with the `imagesc` function. Eq. (3.2) was applied to experimental data to avoid this conflict: for a given index i,

$$\begin{aligned} \text{if } E_{\text{exp}}(i) &< \min(E_{\text{sim}}) \\ E_{\text{exp}}(i) &= E_{\text{sim}}(i). \end{aligned} \tag{3.2}$$

Because the system was originally at rest and not excited until $t > 0$ s, the total energy starts at zero and increases to a value corresponding to the energy imparted by the input force; the parameter $\min(E_{\text{sim}})$ reflects the minimum energy after the global maximum. The choice of `NaN` instead of $\min(E_{\text{sim}})$ would be more appropriate, but `imagesc` does not generate plots correctly with this parameter, either. A second commentary is that the relative-displacement time series is actually the one that tracks the higher-frequency oscillation (near 50 rad/s). This frequency is not present in either of the pure displacements (Figs. 3.11).

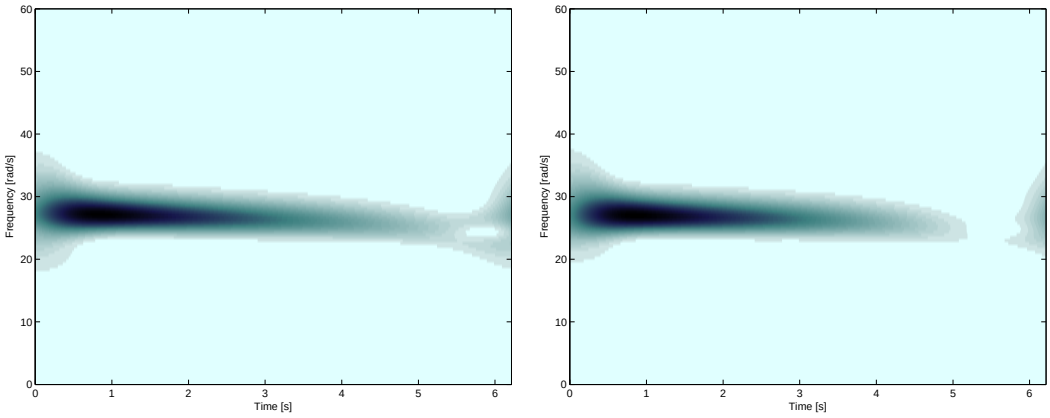

(a) Simulation: LO WT

(b) Experimental: LO WT

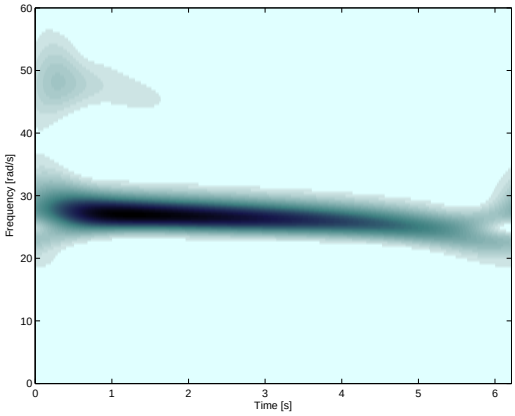

(c) Simulation: NES WT

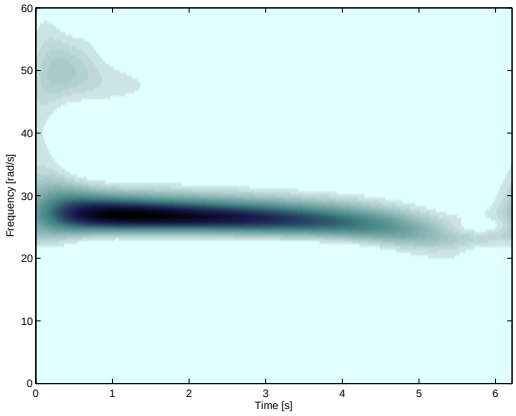

(d) Experimental: NES WT

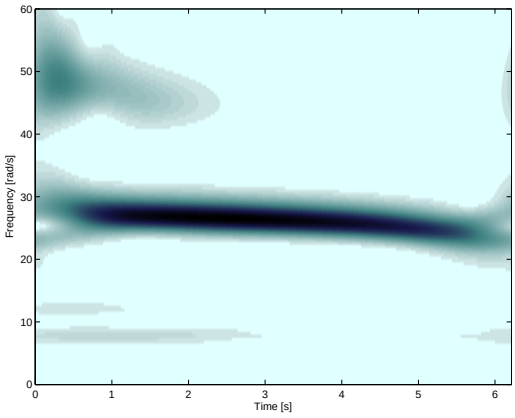

(e) Simulation: $x_{\mathrm{rel}} = y - v$ WT

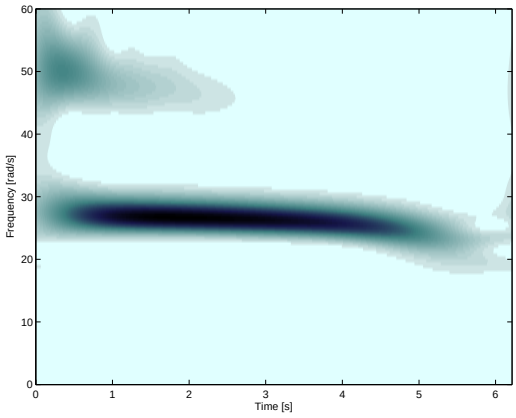

(f) Experimental: $x_{\mathrm{rel}} = y - v$ WT

Fig. 3.26. Applying the wavelet transform to the displacement data results in roughly the same frequencies as those generated from the EMD and Hilbert transform process, but with far less sharpness.

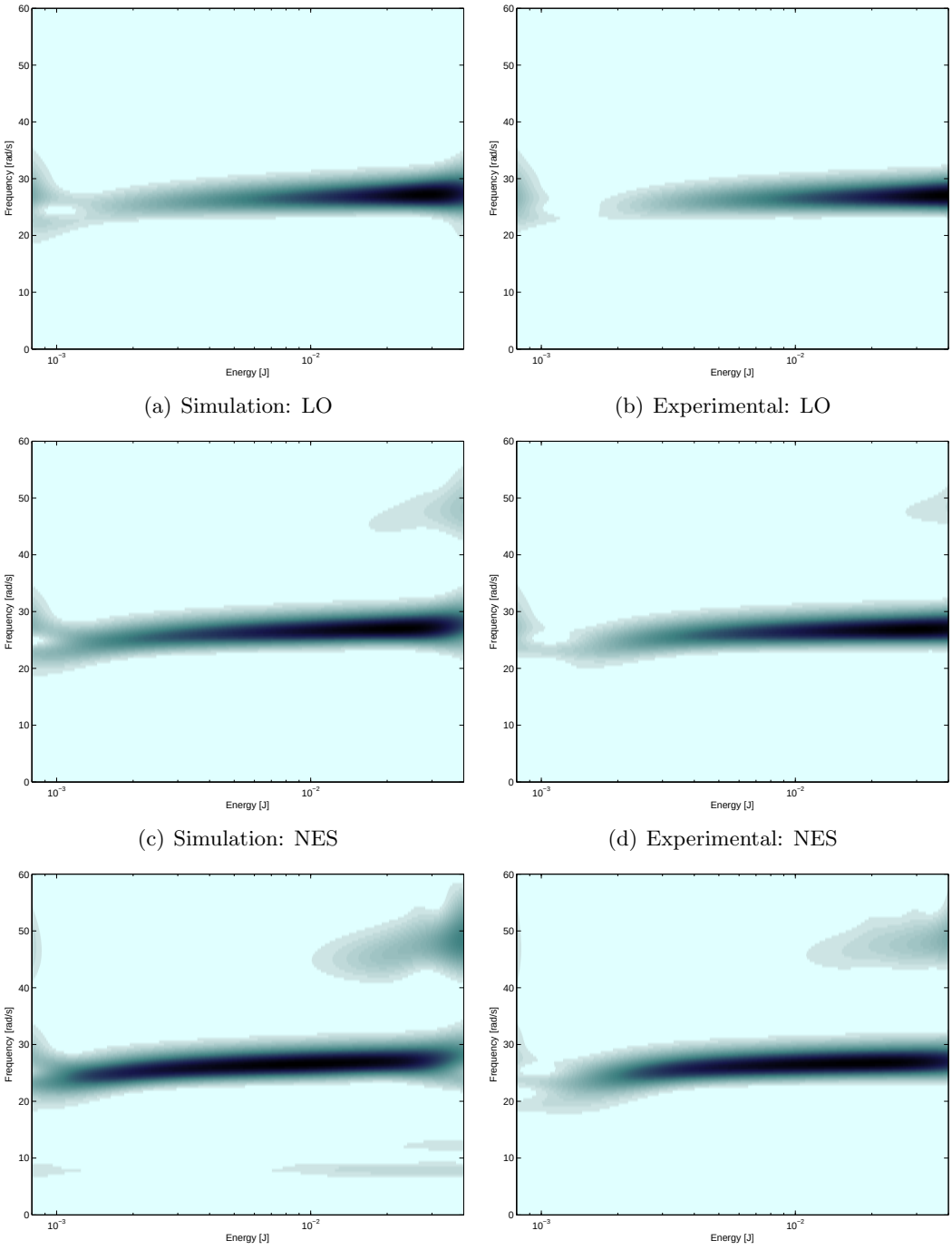

(a) Simulation: LO

(b) Experimental: LO

(c) Simulation: NES

(d) Experimental: NES

(e) Simulation: $x_{\mathrm{rel}} = y - v$

(f) Experimental: $x_{\mathrm{rel}} = y - v$

Fig. 3.27. The FEPs generated from the wavelet transforms also show 1:1 resonance capture.

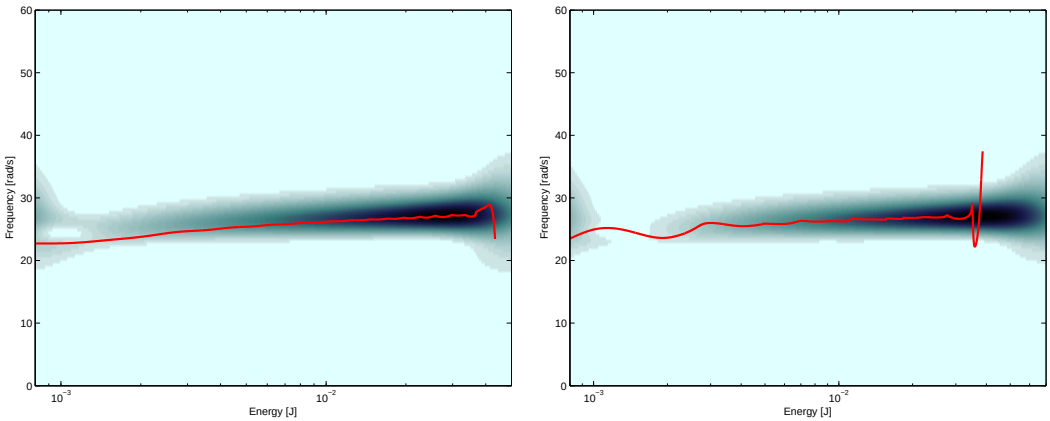

(a) Simulation: LO

(b) Experimental: LO

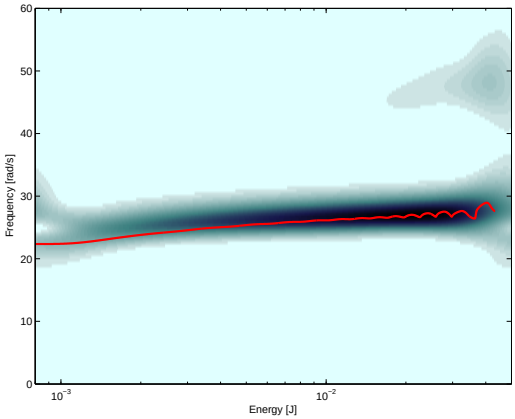

(c) Simulation: NES

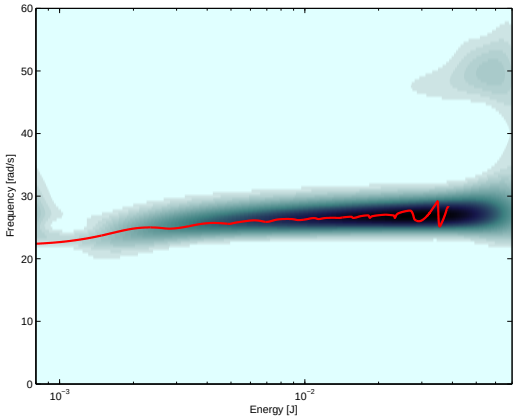

(d) Experimental: NES

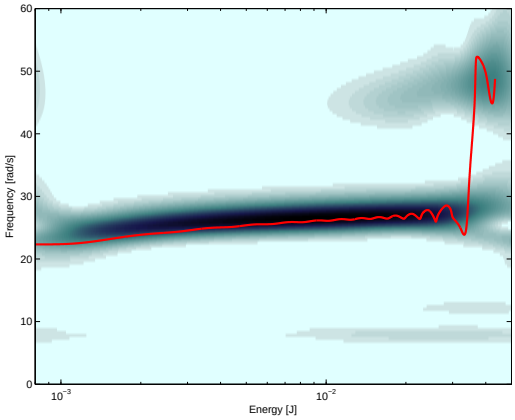

(e) Simulation: $x_{\mathrm{rel}} = y - v$

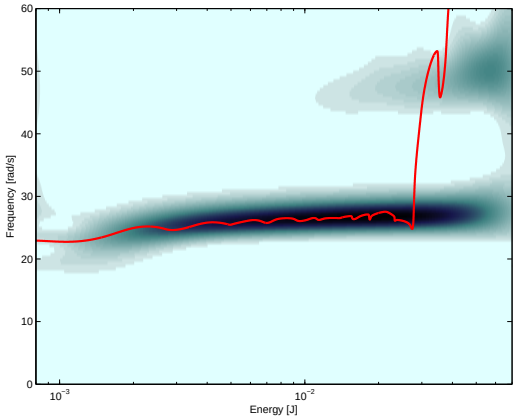

(f) Experimental: $x_{\mathrm{rel}} = y - v$

Fig. 3.28. Compared to Figs. 3.23 and 3.24, the increased sharpness of the frequency estimate of the Hilbert transform is readily apparent.

3.2.2 Case 2: 34 N Excitation Force

Parameter	Value
m_1 [kg]	1.266
m_s [kg]	0.14
k_1 [N/m]	1150
k_s [N/m$^{2.8}$]	4.11×10^6
c_1 [N/m/s]	0.135
c_s [N/m/s]	0.33

Table 3.2. Parameters for the nonlinear model of eq. (3.1); data from Kowtko [8].

We now present the next case, which has a smaller forcing amplitude to incite nonlinear beating. As expected with a smaller excitation amplitude, the resulting accelerations have considerably lower magnitude, and the number of cycles before all energy is dissipated is also fewer than in the previous case. Application of the EMD algorithm (again with no masking signal) results in moderately-clean IMFs. Though it is evident from the displacement time series that the linear oscillator stops oscillating after approximately 4.5 s and the NES around 6 s, it is of additional significance here because both the EMD and the Hilbert transform work best with data that contains several cycles over the duration of the signal. Although there are many full fast cycles within the slow flow envelope, the number of cycles of the simulated system exhibiting 1:3 TRC far exceeds that here, and it is unfortunately expected that the decomposition may not be quite as clean as even the previous case. Here, too, we have chosen the frequencies of the first LO IMF and NES IMF to plot on the ordinate axis. The criteria for this choice are again based on the IMF amplitudes and frequencies; it is appropriate to choose times over which they are well-behaved in the FEP. As a result of this latter criterion, much of the linear oscillator data for low energy should be discarded due to a negligible IMF amplitude: the LO is no longer in motion after roughly 4 s, and the extremely low energy content associated with any negligible movement is not truly evident physically. Thus, the LO branches of the FEPs constructed (Figs. 3.37 and 3.38) are not valid for the entire time interval. This was done numerically with eq. (3.2). Even with this substitution, we see that Fig. 3.37 is not as clean as Fig. 3.23. This shows the effect of short time-series on the FEP.

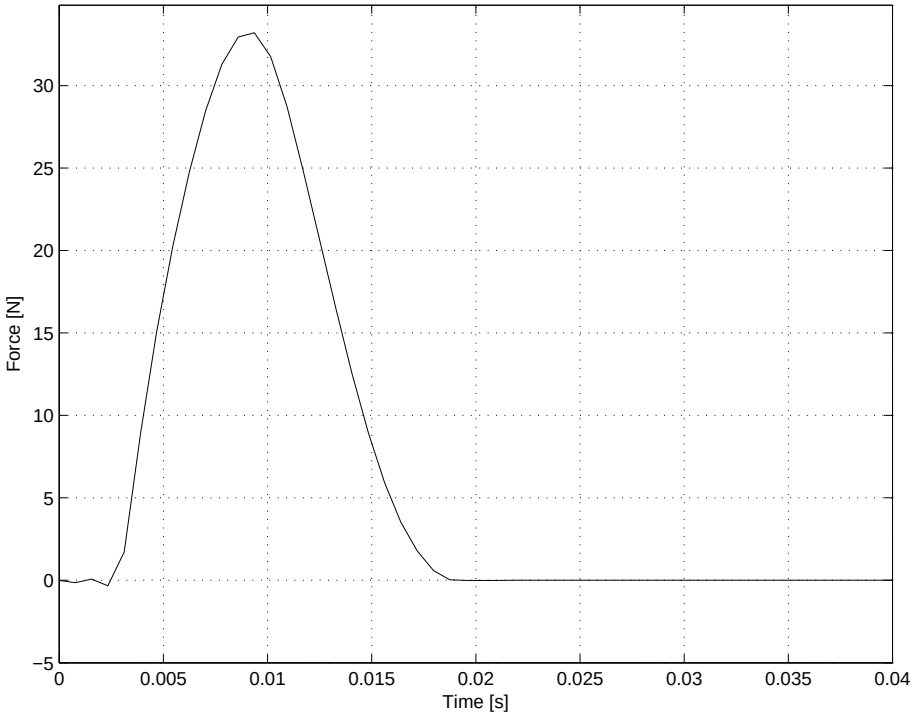

Fig. 3.29. The forcing is of lower magnitude than in the previous case considered.

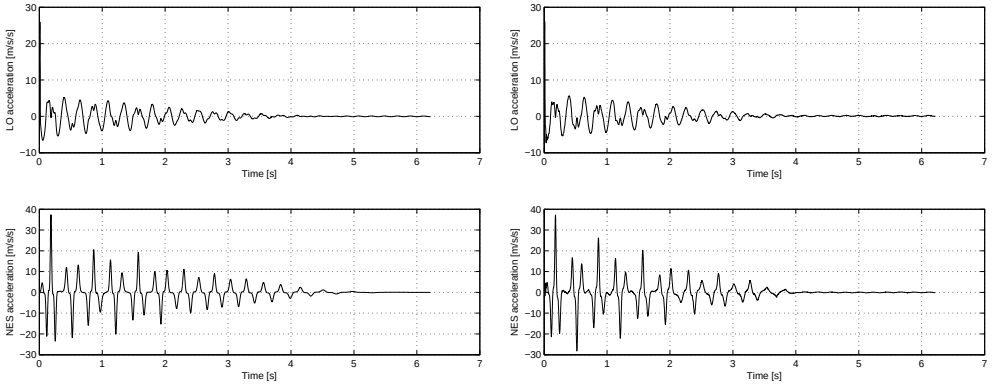

(a) Simulation (b) Experimental

Fig. 3.30. The simulated (left) and filtered experimental (right) acceleration data for the second case.

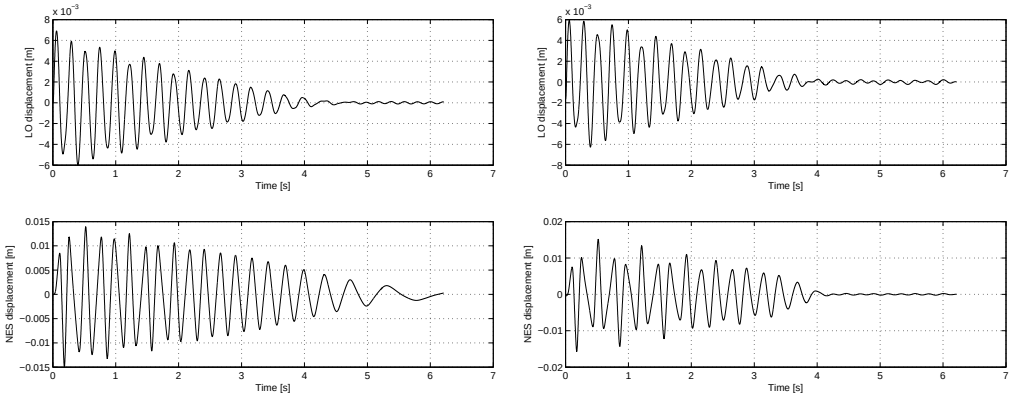

(a) Simulation (b) Experimental

Fig. 3.31. The simulated (left) and measured (right) displacements for the second forcing case.

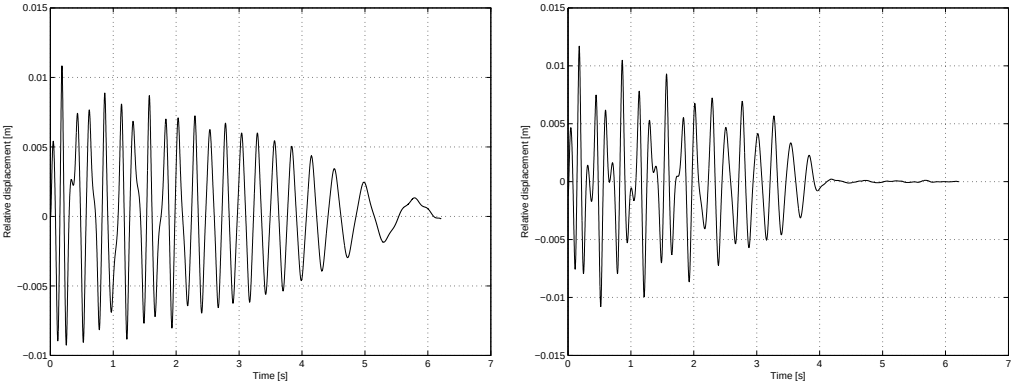

(a) Simulation (b) Experimental

Fig. 3.32. The simulated and measured relative displacements for the second case.

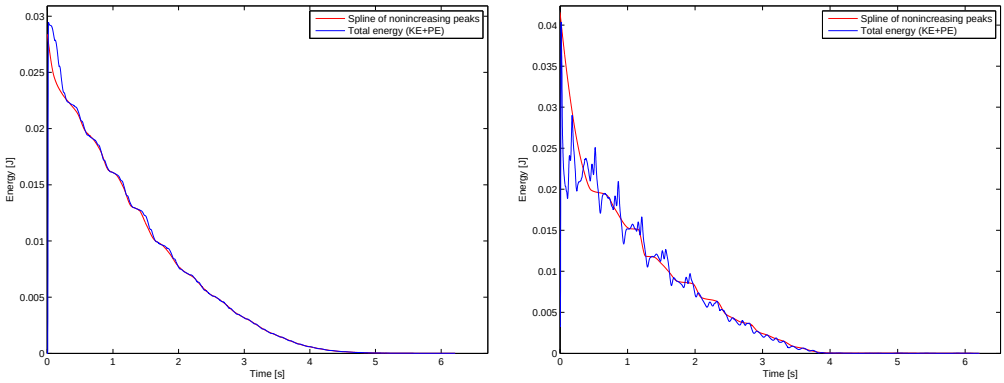

(a) Simulated (b) Experimental

Fig. 3.33. The peak-picking algorithm is still able to estimate successfully the total energy of the system.

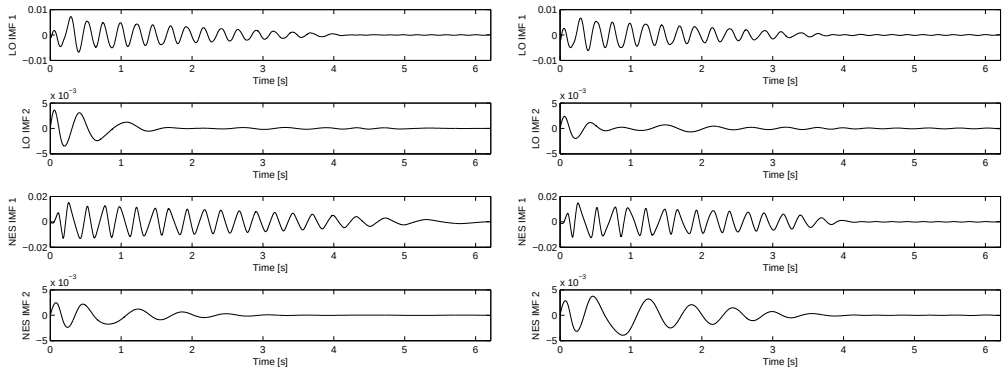

(a) Simulation (b) Experimental

Fig. 3.34. The IMFs appear to be as smooth as those in Fig. 3.18, but it can be difficult to estimate the smoothness of their frequencies simply from inspection.

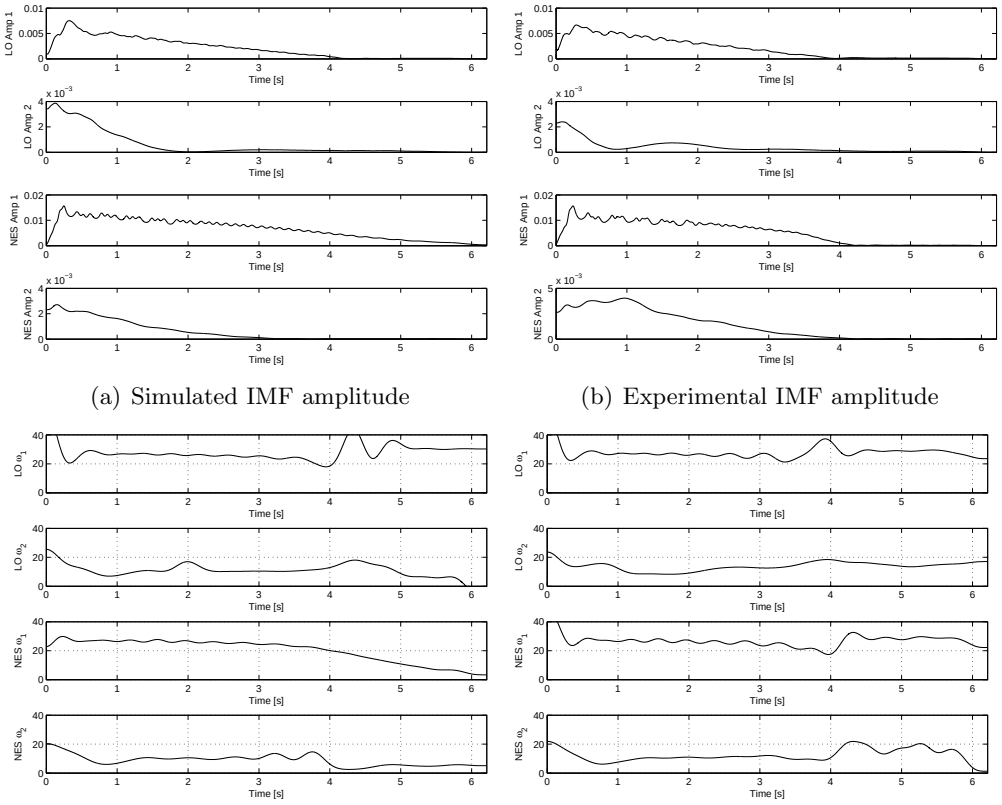

(a) Simulated IMF amplitude

(b) Experimental IMF amplitude

(c) Simulated IMF frequency

(d) Experimental IMF frequency

Fig. 3.35. The amplitude ((a), (b)) and frequency ((c), (d)) of the IMFs produced from simulation (left) and experimental data (right).

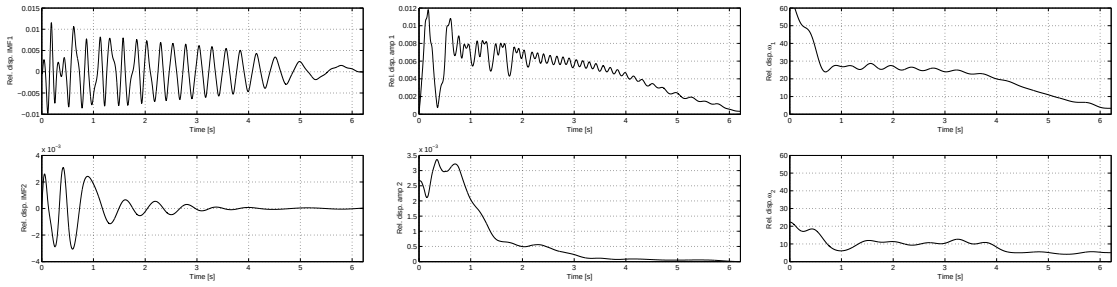

(a) IMFs

(b) IMF amplitude

(c) IMF frequency

Fig. 3.36. The first two IMFs (a) of the second forcing case, their amplitudes (b), and their frequencies (c) of the relative displacement between the two oscillators are plotted in the top and bottom rows.

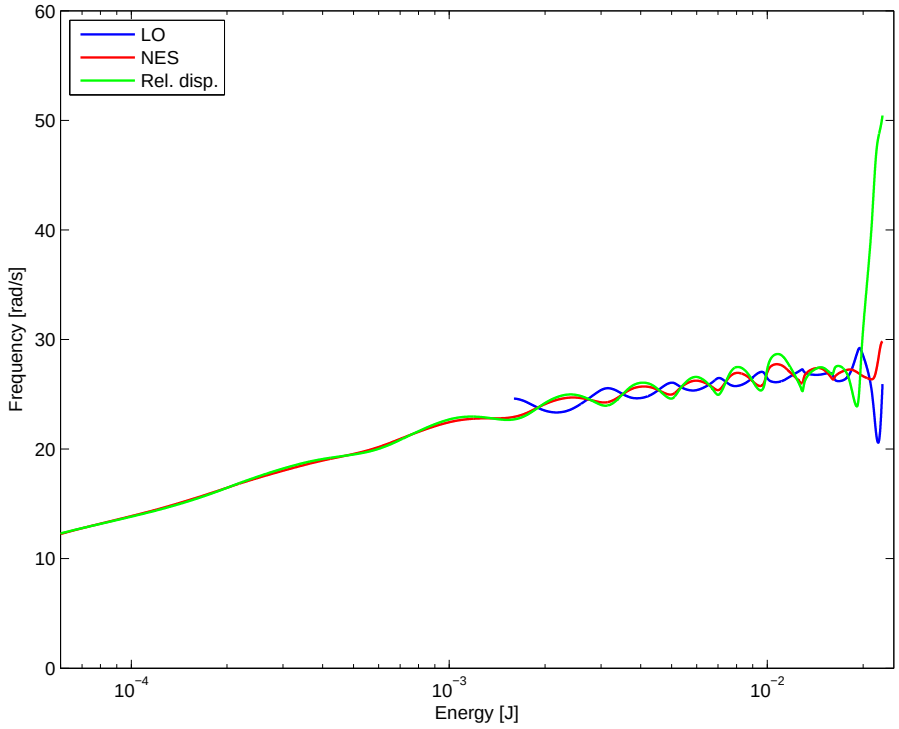

Fig. 3.37. The S_{11^+} branch produced from simulation data for the system exhibiting nonlinear beating is not quite as smooth as for the previous system.

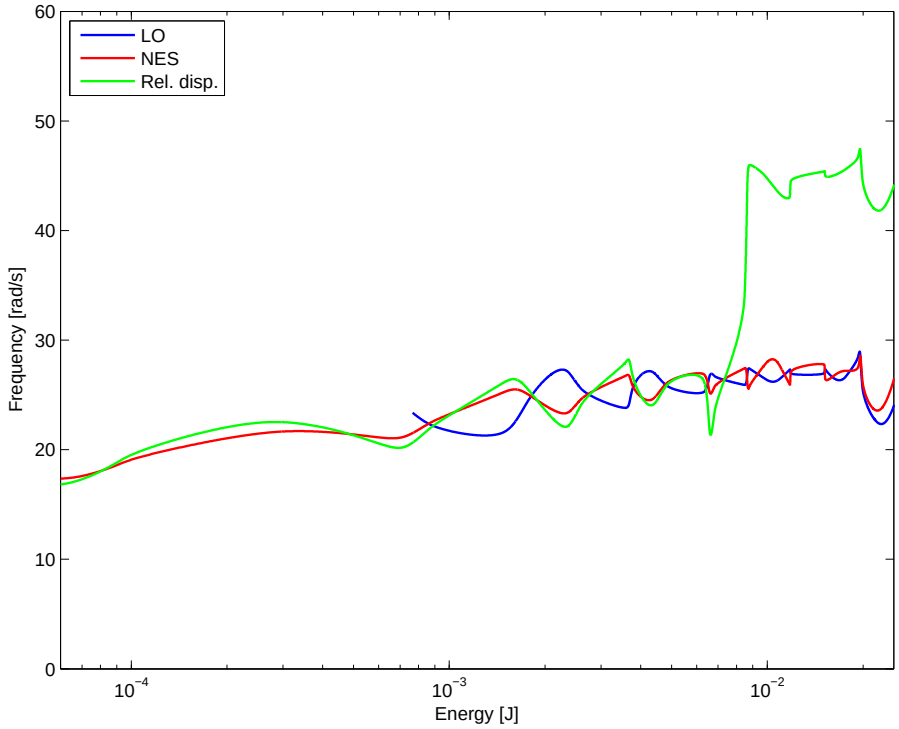

Fig. 3.38. The FEP produced from experimental data for the system exhibiting nonlinear beating faces many of the same issues as those from simulation.

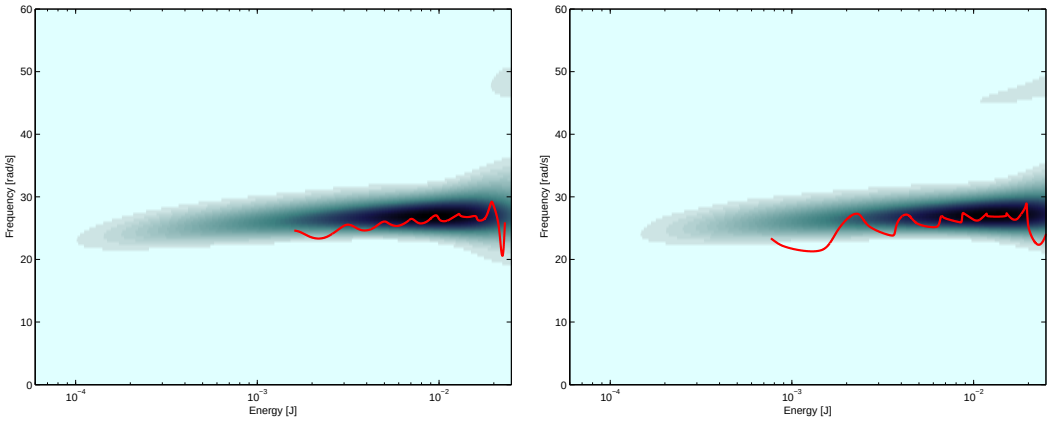

(a) Simulation: LO

(b) Experimental: LO

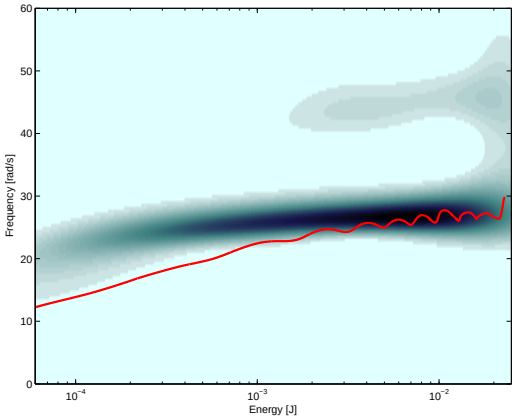

(c) Simulation: NES

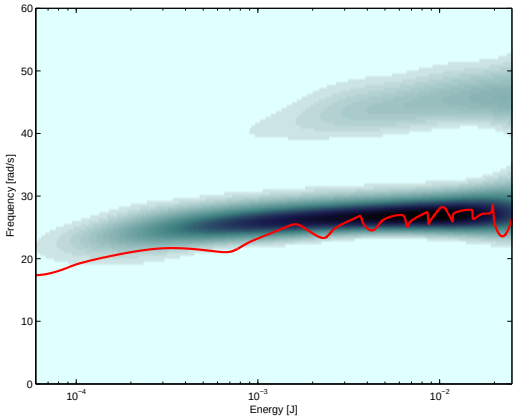

(d) Experimental: NES

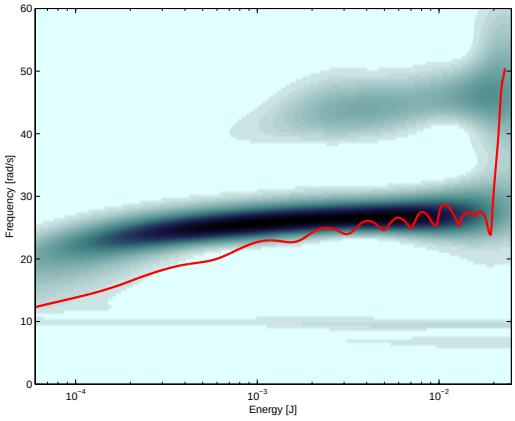

(e) Simulation: $x_{\mathrm{rel}} = y - v$

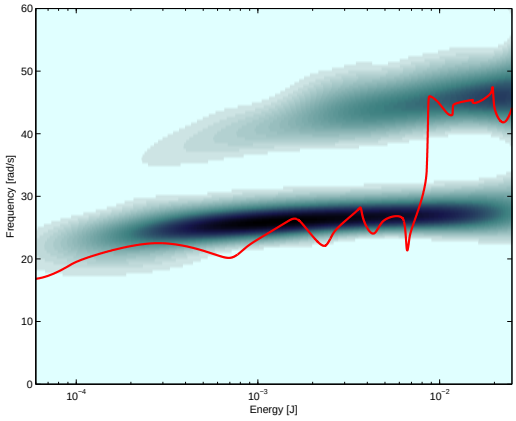

(f) Experimental: $x_{\mathrm{rel}} = y - v$

Fig. 3.39. Although the EMD-Hilbert transform method continues to provide some additional sharpness, further investigation of treatment of short-duration signals is extremely important.

3.2.3 Case 3: 38 N Excitation Force

Parameter	Value
m_1 [kg]	1.266
m_s [kg]	0.14
k_1 [N/m]	1143
k_s [N/m^3]	4.28×10^6
c_1 [N/m/s]	0.1
c_s [N/m/s]	1.622

Table 3.3. Parameters for the nonlinear model of eq. (3.1); data from Kowtko [8].

The third case presented has roughly the same forcing magnitude as that of the previous case, but the damping between the primary mass and the NES on this system is far greater than that present in the first two systems. The original intent in constructing the physical system was to show optimal energy transfer into the NES, but the primary goal here remains FEP construction. The FEP algorithm was perhaps most challenged by this dataset, as there were very few fast cycles present within the slow flow envelope. The IMFs (Fig. 3.45) don't look terrible, but they have practically zero amplitude beyond 2 s, and in that time, the fast oscillations only achieve a maximum of seven oscillations. The resulting FEPs of both simulation (Fig. 3.48) and experimental (Fig. 3.49) data are somewhat difficult to interpret as a result, but there is certainly some agreement between the wavelet transform FEP and the one generated by the EMD and Hilbert transform procedure. Here again, the difficulty of processing a short time signal of any data, experimental or simulation, is quite evident. The EMD algorithm works best on signals with many fast cycles and of longer duration, and the challenges are compounded because the Hilbert transform also works most efficiently with longer signals. The minimum energies in the wavelet transform FEPs were again set to the corresponding energies of the simulation data to prevent near-zero abscissa values using eq. (3.2).

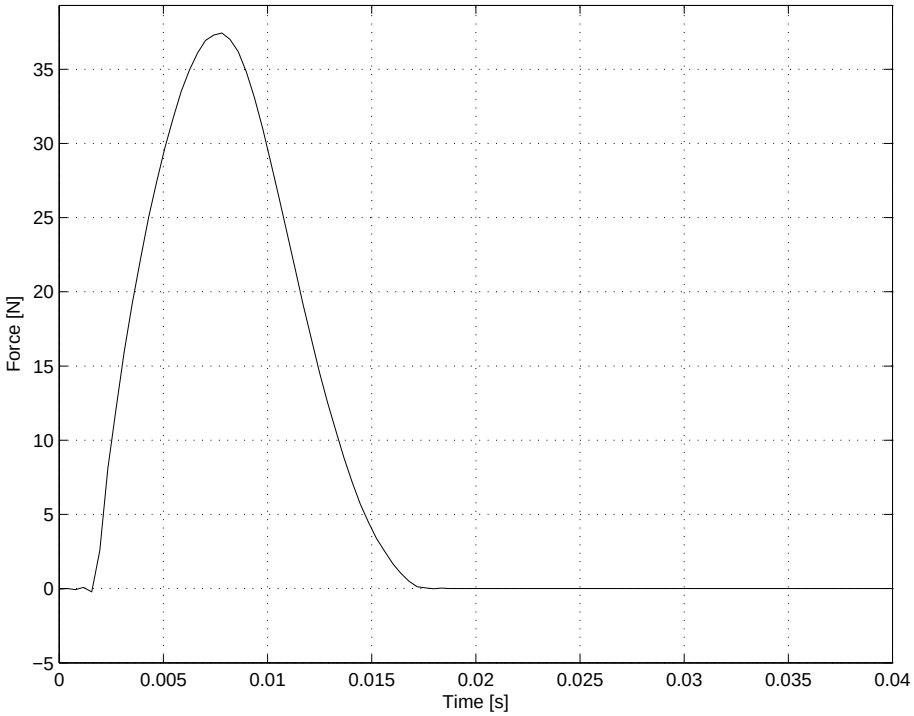

Fig. 3.40. The forcing, plotted versus time, applied to the physical system.

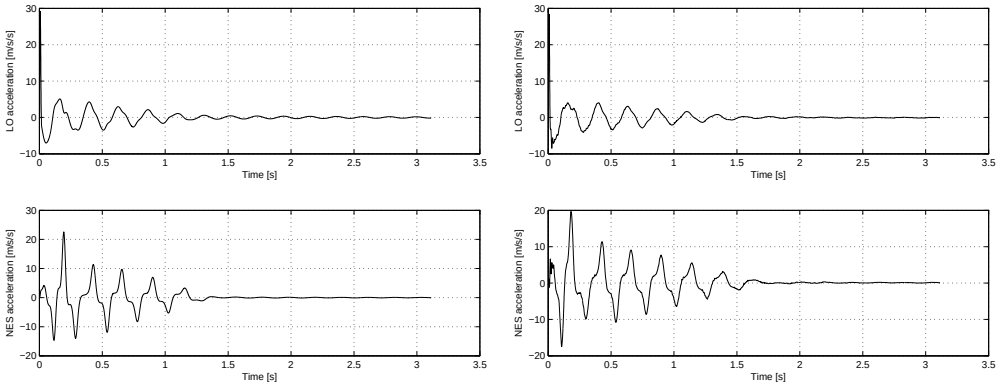

(a) Simulation (b) Experimental

Fig. 3.41. A comparison of the simulated and measured, filtered acceleration data.

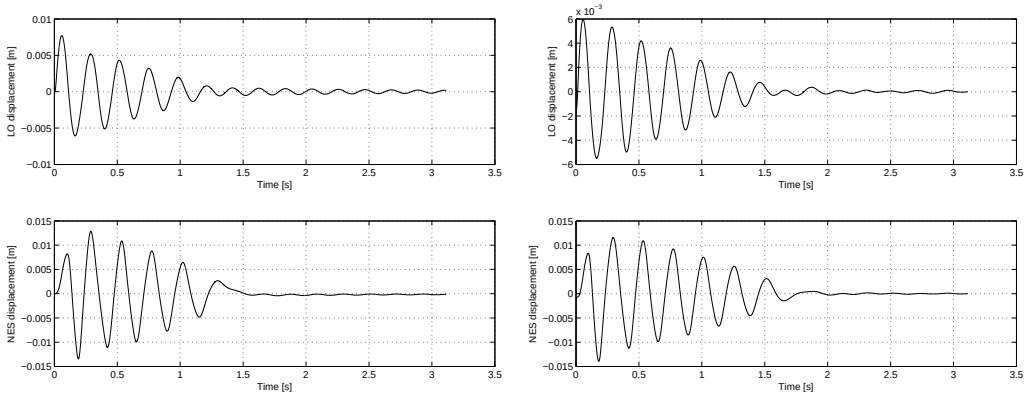

(a) Simulation (b) Experimental

Fig. 3.42. A comparison of the simulated and measured displacements.

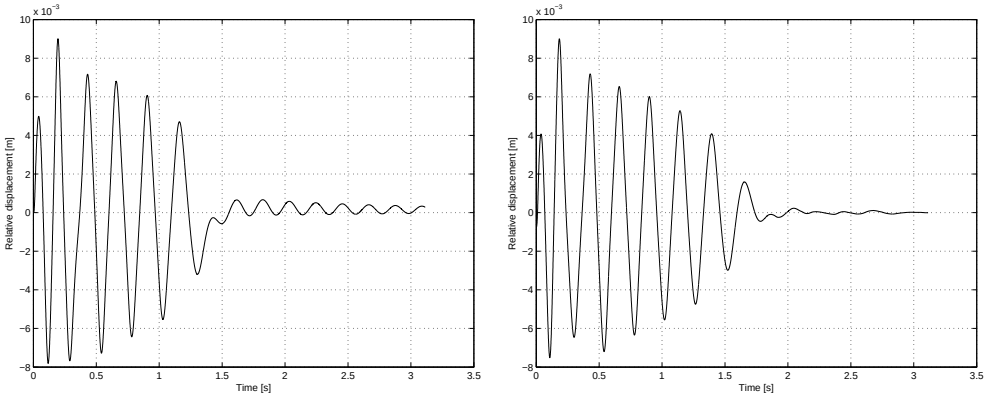

(a) Simulation (b) Experimental

Fig. 3.43. A comparison of the simulated and measured relative displacement.

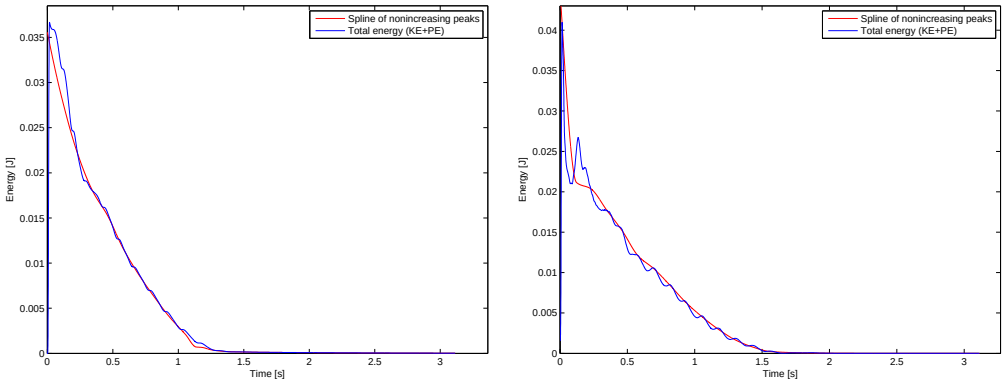

(a) Simulated (b) Experimental

Fig. 3.44. Here, too, the nonincreasing peaks of the kinetic energy serve as an admirable estimate of the total energy, even though there is a clear buckle in the experimental total energy that renders it not a monotonically-decreasing function.

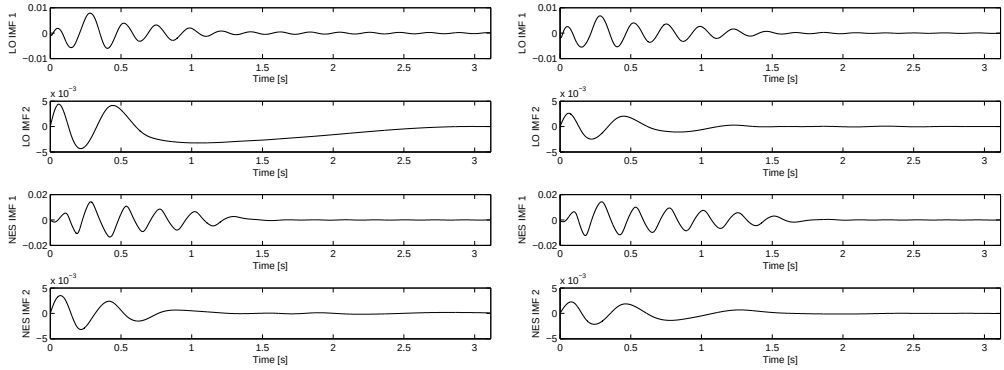

(a) Simulation (b) Experimental

Fig. 3.45. The EMD analysis yields IMFs that are generally well-behaved.

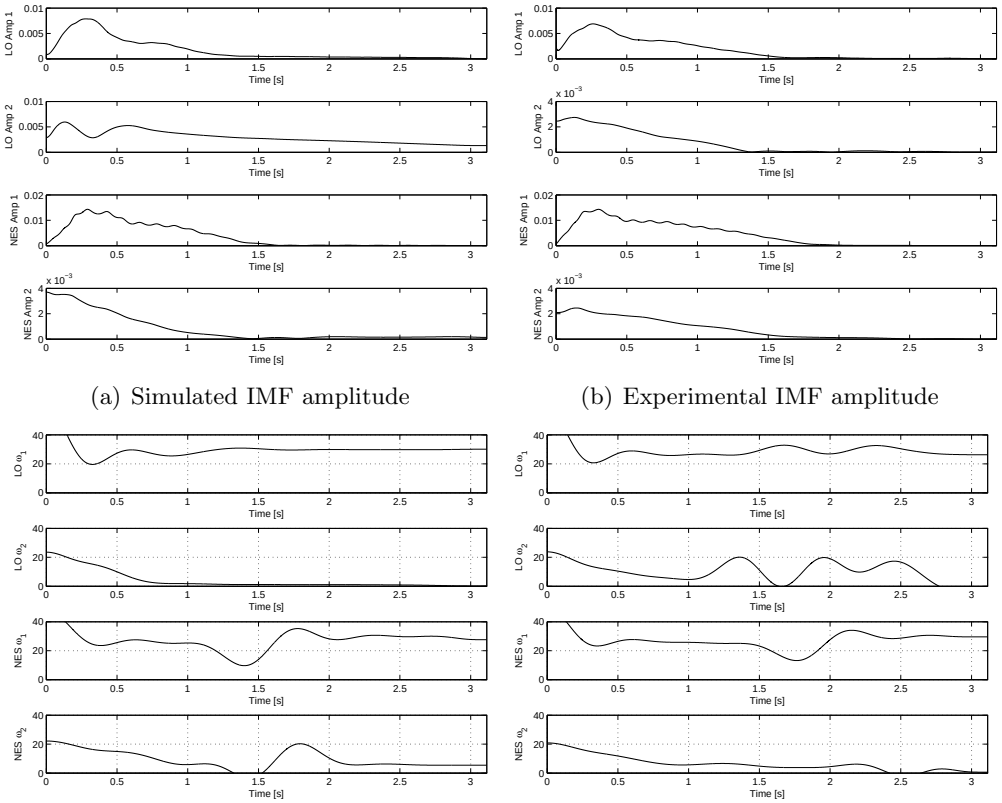

(a) Simulated IMF amplitude (b) Experimental IMF amplitude

(c) Simulated IMF frequency (d) Experimental IMF frequency

Fig. 3.46. The amplitude ((a), (b)) and frequency ((c), (d)) of the IMFs produced from simulation data (left) and experimental data (right).

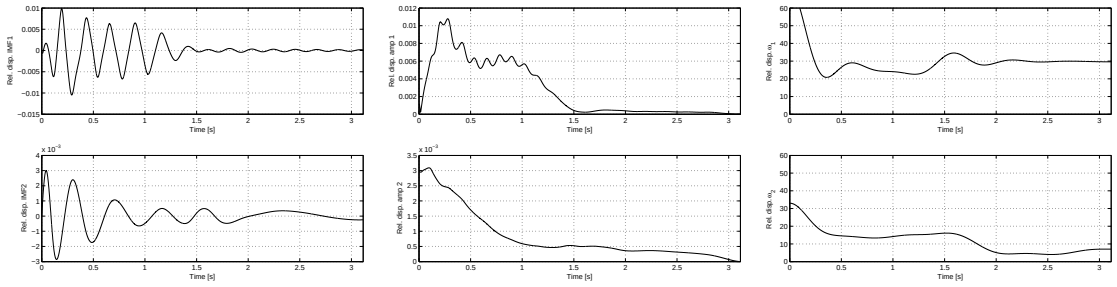

(a) IMFs (b) IMF amplitude (c) IMF frequency

Fig. 3.47. The first two IMFs (a) of the third forcing case, their amplitudes (b), and their frequencies (c) of the relative displacement between the two oscillators are plotted in the top and bottom rows.

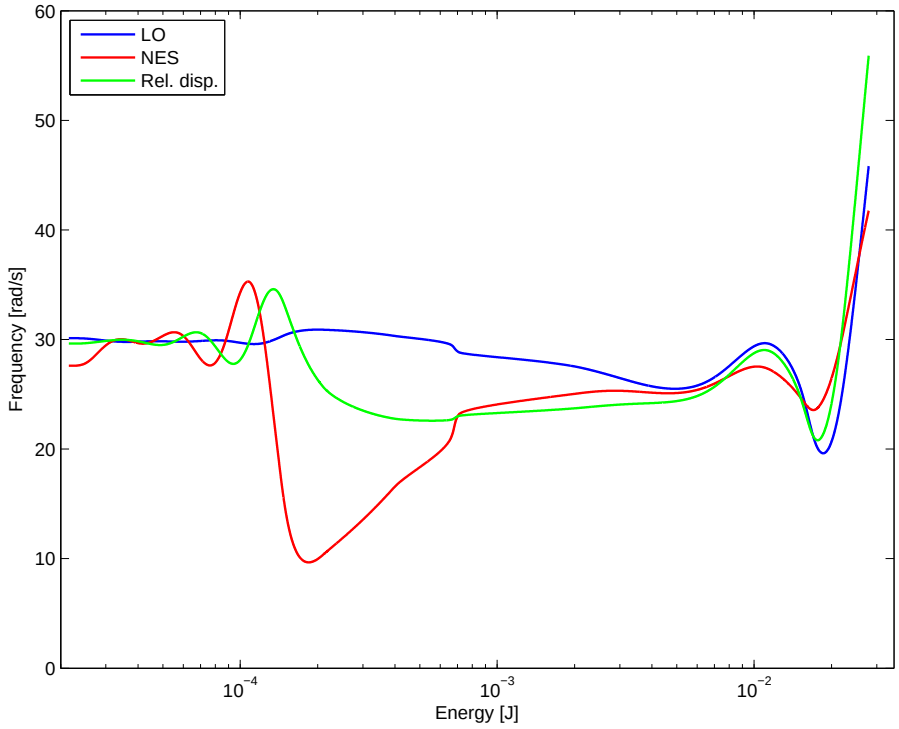

Fig. 3.48. The FEP produced from simulation data shows the approximate 1:1 resonance capture between the LO and NES, but it is not as clear as it was in Case 1.

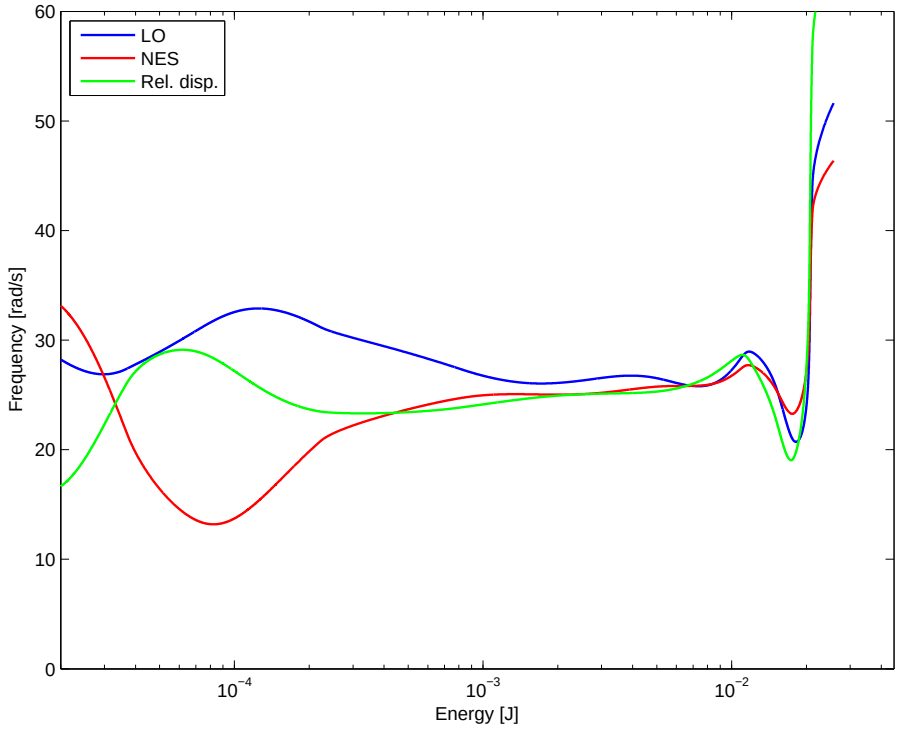

Fig. 3.49. The FEP produced from experimental data also tracks the approximate 1:1 resonance capture with less clarity than in Case 1.

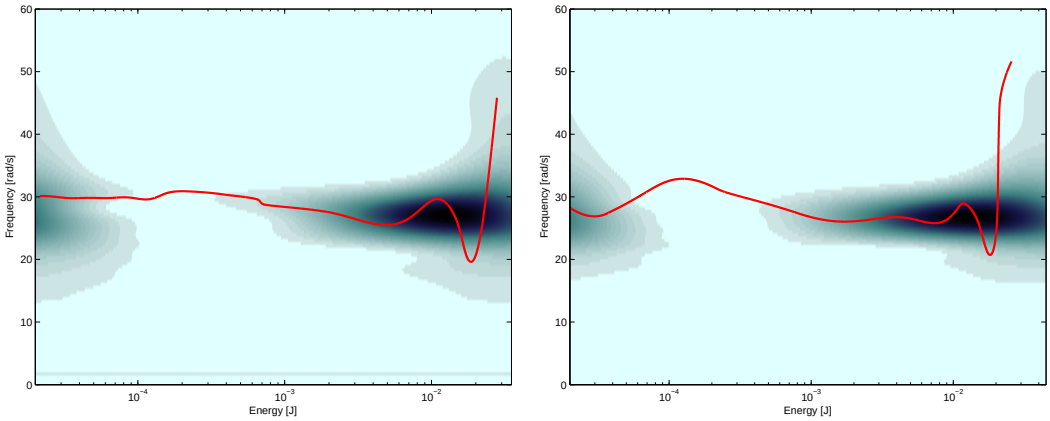

(a) Simulation: LO

(b) Experimental: LO

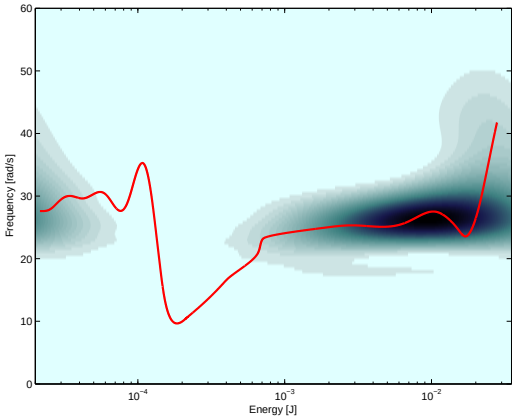

(c) Simulational: NES

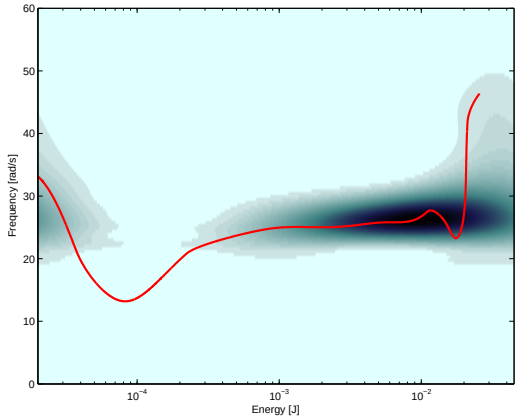

(d) Experimental: NES

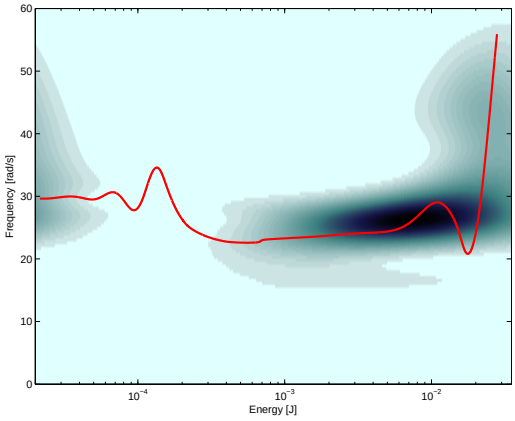

(e) Simulation: $x_{\mathrm{rel}} = y - v$

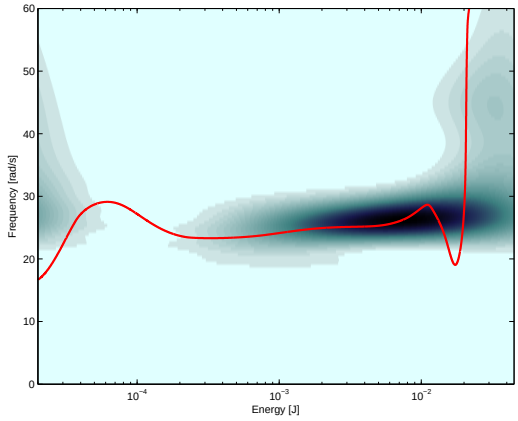

(f) Experimental: $x_{\mathrm{rel}} = y - v$

Fig. 3.50. The EMD and Hilbert transform frequency estimates are compared to the wavelet transform frequency estimates for simulation (left column) and experimental (right column) time series.

3.2.4 Effects of Filtering and Post-Processing

The greatest difficulty encountered with constructing the FEP from these time series, particularly evident in the last two cases, was that the duration of the signal is short. We assume that there should be several cycles corresponding to any branch of the FEP, and for the cases with 34 N and 38 N maximum force, the cessation of motion after roughly 1.5 s and 4 s, respectively, significantly affects the ability of the EMD algorithm to produce IMFs and of the Hilbert transform in estimating the frequency and amplitude content of the IMFs. Although these considerations were not present for the system observed in 1:3 TRC and on which the algorithm was demonstrated, various issues are clearly present with practical application of the algorithm.

One factor with a large influence on the total energy of the system, assuming known system parameters, is the cutoff frequency used to filter the acceleration data. The displacement of the carts affects the potential energy, which in turn has a contribution to the total energy. This does not impact the energy estimate as much, since it relies on kinetic energy and thus on velocities, but the smoothness of the plotted FEP branches is affected by the displacement. For poorly-integrated velocities, the slow wobble in the displacement time series results in an artificial low-frequency component evident especially in the wavelet transform. Of course, this could be filtered out, but the main point is that the integration scheme used to calculate the displacements plays a large role in the smoothness and in whether the total energy is in fact monotonically decreasing. The procedure to generate the displacements used to calculate the potential energy component of Fig. 3.12(b) can be summarized in five steps:

- Filter measured acceleration data with low-pass filter to remove noise
- Filter result with high-pass filter to remove offset.
- Integrate filtered acceleration to obtain velocity.
- High-pass filter the velocity signal to remove offset.
- Integrate filtered velocity to obtain displacement.

Fourth-order Butterworth filters were used to process the acceleration data, but because the MATLAB command `filtfilt` was used, the resulting filter is effectively of eighth-order.

In Figs. 3.51, we show the effects of filter cutoff frequencies on the total energy estimate. The erratic nature of the total energy is a manifestation of the potential energy—even with a seemingly smooth (and well-behaved) displacement, it is clear that the potential energy is strongly affected by small shifts in the cutoff frequency. In an extreme case with no filtering, Figs. 3.51(a), the displacements are so large that the estimated total energy is negligible, when in fact it is still of an order of magnitude commensurate with experimental observations. Even when the displacement seems plausible (as in the third row of plots), the total energy estimate does not match with observations of the behavior of the physical system. The figure also shows indirectly the elegance of energy estimation with the kinetic energy: it can be difficult to estimate spring stiffnesses and especially nonlinear stiffnesses, but obtaining the velocity from an experimental system is rather straightforward—and the total energy estimate is quite accurate as a result. In the figures below, note that the f_c parameter denotes the parameter used in the MATLAB code. The condition $f_c = 1$ denotes a cutoff frequency equal to half the sampling rate, so the plots and f_c shown here are indicative only of a specific sampling frequency. As has become somewhat evident, system identification is best approached on a case-by-case basis, filtering included. In Figs. 3.51, it is clear that no high-pass filtering at all causes a non-physical resulting velocity and displacement. With increasing high-pass cutoff frequency, the wobble in the displacement time series is reduced, and there is little perceptible difference between the energy estimates depicted in the fourth and fifth rows.

The effects of cutoff frequency also play a role in the Hilbert transform. Time differentiation is used to extract the frequency information, so a low-pass filter is appropriate. In the FEPs presented, the cutoff frequencies were selected to reduce the ripple in the frequency estimate. The IMFs are not actually sinusoids (they are cubic splines between maxima), so it is possible that the frequency content for an IMF produced from even a pure sinusoid might not be constant. As experimental systems are investigated, various effects could introduce even more rippling into the IMF frequency, which is evident in the experimental data already presented. To make clear the effect of the cutoff frequency in reducing this

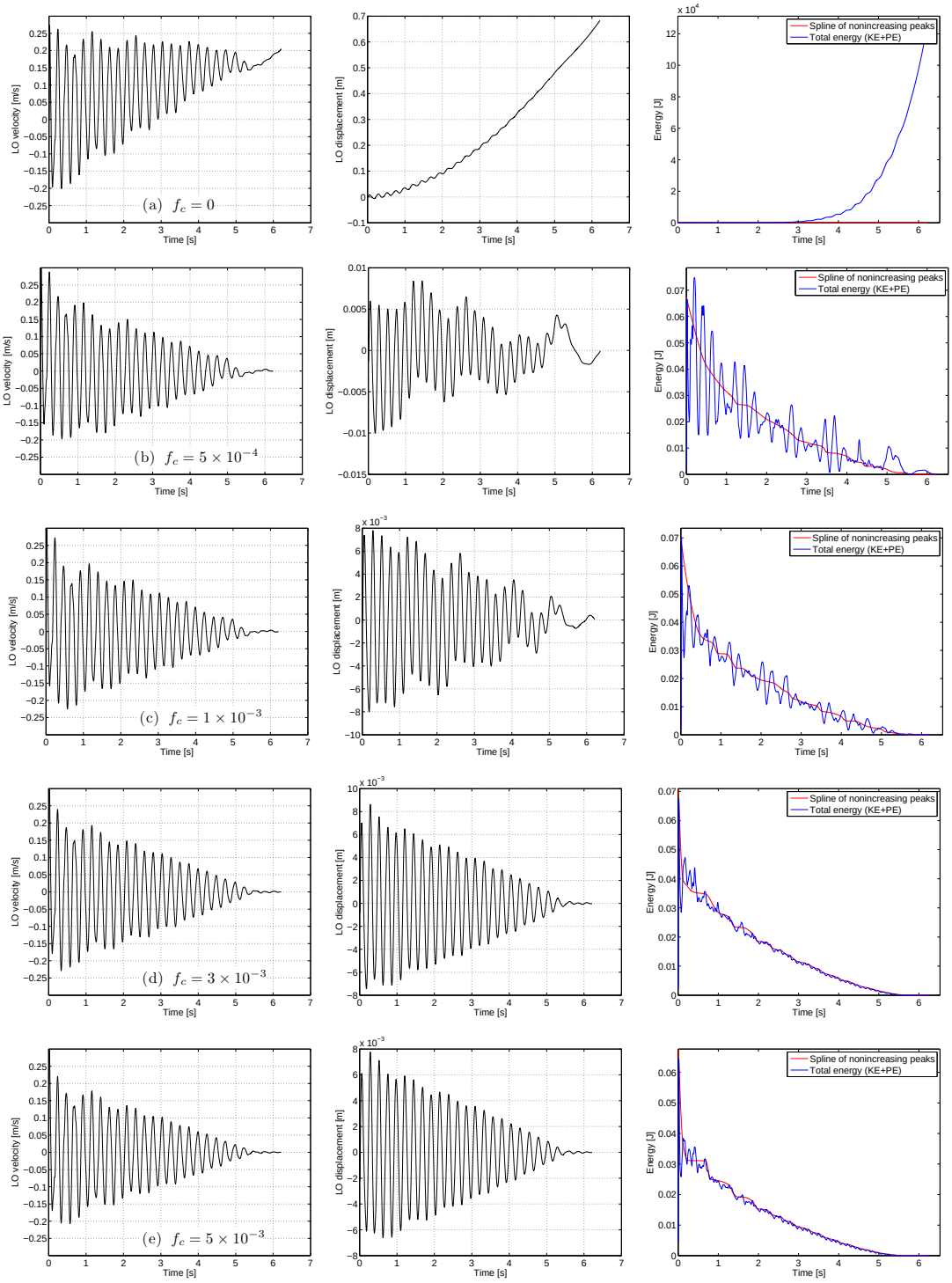

Fig. 3.51. Cutoff-frequency effects on the LO velocity (left) and displacement (center), and total system energy (right).

ripple, consider Figs. 3.52 on the following page. The f_c parameter is again that used in MATLAB and related to the sampling rate of the data collected. Here, too, there appears to be a threshold beyond which the cutoff frequency does not play as large a role. (The IMFs, which are processed by the EMD algorithm, do not show a difference due to cutoff frequency, which is used explicitly in the Hilbert transform.) The FEPs constructed previously use a cutoff frequency that preserves detail rather than smoothing everything entirely.

These are just two of the many considerations in constructing the FEP from time series. IMFs lacking clean frequencies produced by the Hilbert transform require additional analysis, and many of these examinations were discussed in the previous three sections. In summary, there are several possible parameters of IMF processing to adjust to construct the FEP most representative of a particular system. Listed here are just a few.

- Based on IMF amplitudes, decide whether there are portions of the IMF frequencies to discard.
- Decide what the initial energy of the system is. If the forcing does not start at $t = 0$ s, there will be zero energy at initial time. When the forcing begins, energy will quickly ramp up. How prominently this is evident in the FEP will vary from system to system.
- The cutoff frequencies used to filter the estimated frequency from the Hilbert transform can play a key role in the smoothness of the FEP. It is, however, important not to attempt to smooth all responses; some amount of detail must still be preserved.
- Compare the frequency content of the retained subsets of the IMFs to the frequency estimates from the wavelet transforms.
- Practically, the experimental total energy does go to zero. (It is important to assign a threshold value so that the logarithmic abscissa of the FEP can interpret this "0" energy correctly.)

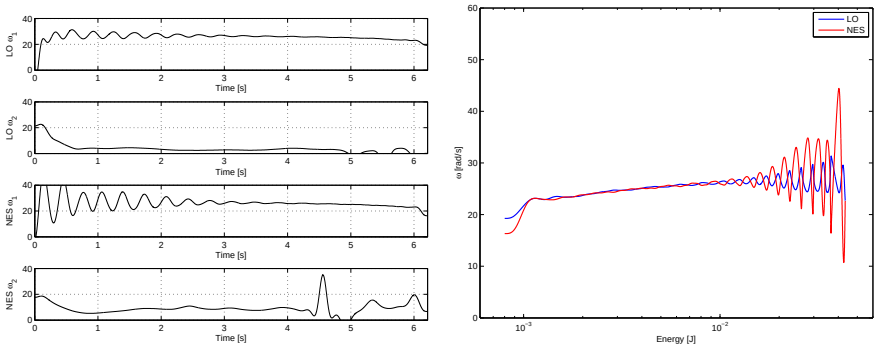

(a) $f_c = 5$

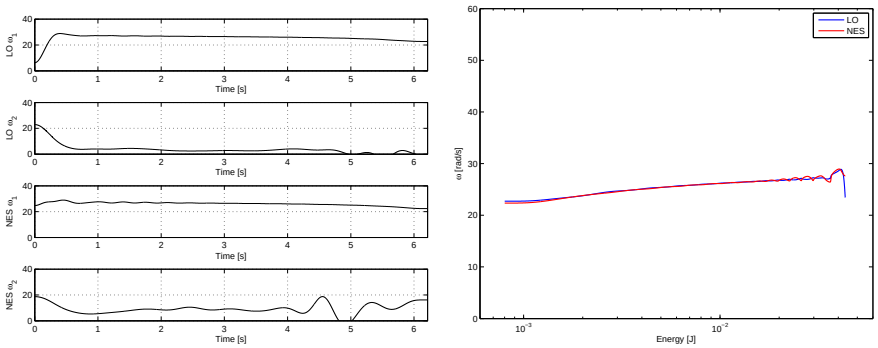

(c) $f_c = 2$

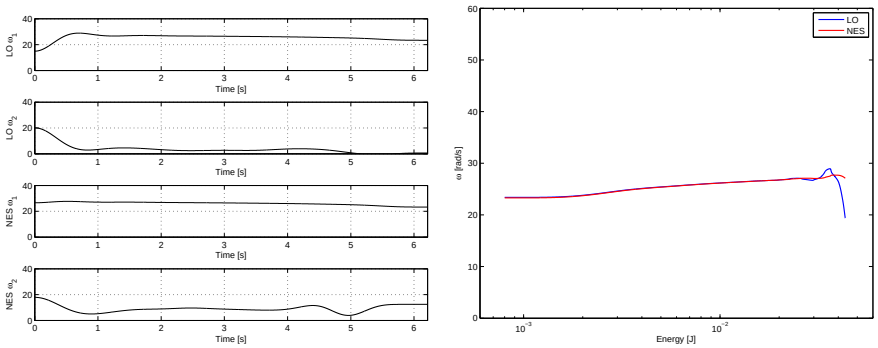

(e) $f_c = 1$

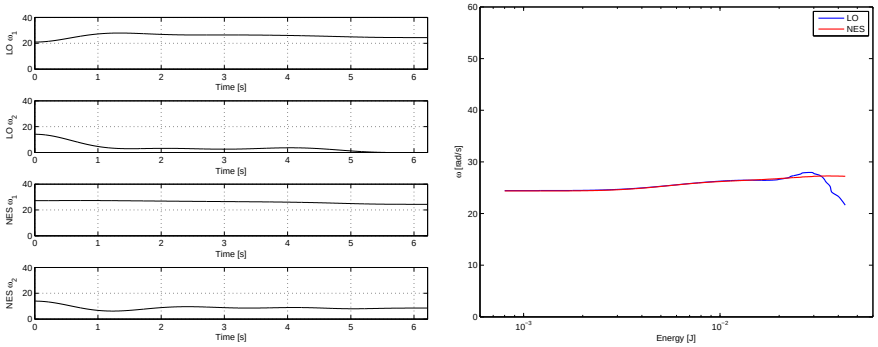

(g) $f_c = 0.5$

Fig. 3.52. Cutoff-frequency consequences on the IMF frequency estimate (left) and FEP (right).

3.3 Observations

The sheer number of cycles in the example used to describe the FEP algorithm (Section 2.4) admits clean IMFs and FEPs. The EMD and Hilbert transform alike are able to demodulate the signal, and it is clear that the system successfully tracks the appropriate tongue. When applied to short-duration simulation and experimental data, there are key difficulties in data-processing. First, the acceleration data must be carefully integrated to preserve the dynamics but still smooth out non-physical artifacts. Second, the low number of cycles means that additional care in selecting the appropriate sections of data to plot is required and that choosing the right intervals is heavily based on the individual system. Finally, when the energy of the experimental system drops below a certain threshold (roughly 6×10^{-6}), MATLAB cannot plot the FEP using the wavelet transform. As this algorithm is made more robust, this is potentially acceptable. In the short term, however, the wavelet transform offers important insight to the behavior of the system and serves as a method against which to compare this new, EMD and Hilbert transform method, so although the FEP can be plotted, careful analysis is required in each case. Above all, the present state of the algorithm is such that filtering parameters and decisions on which frequency and energy intervals to retain and which to discard must be made on an individual basis. It would be dangerous to develop an algorithm that works for a SDOF primary mass with ungrounded NES and then assume that it would work equally well with another system. The intent of the bulk of the previous section was to demonstrate that even parameters like cutoff frequency play a vital role in the portrayal of the FEP.

Chapter 4

Conclusion

4.1 Summary of FEP Construction

The construction of the FEP previously involved a solid command of the mathematical tools in analyzing nonlinear dynamics, but because the FEP is such a powerful representation of the system dynamics, it is ideal to have an algorithm to construct the FEP quickly; this is true for experimental systems in particular due to the difficulty of ascertaining system parameters. The construction of the FEP outlined in this work is largely summarized in four steps.

1. Given a system's mass distribution and velocity time series, estimate the total system energy from picking the nonincreasing peaks of the kinetic energy.
2. Use the EMD algorithm to generate IMFs.
3. Apply the Hilbert transform to the IMFs to estimate the IMF frequencies.
4. The FEP is generated when plotting these frequencies against the estimated total energy of step 1.

Several resulting FEPs were generated using this algorithm, which offers a finer estimation of frequency than does the wavelet transform. First, the FEP representing a simulated single-degree-of-freedom primary mass with an ungrounded nonlinear energy sink in 1:3 TRC was plotted. Various means, including filtering, windowing, mirroring, and the use of a masking signal, were required to generate the correct IMFs, but once generated, the

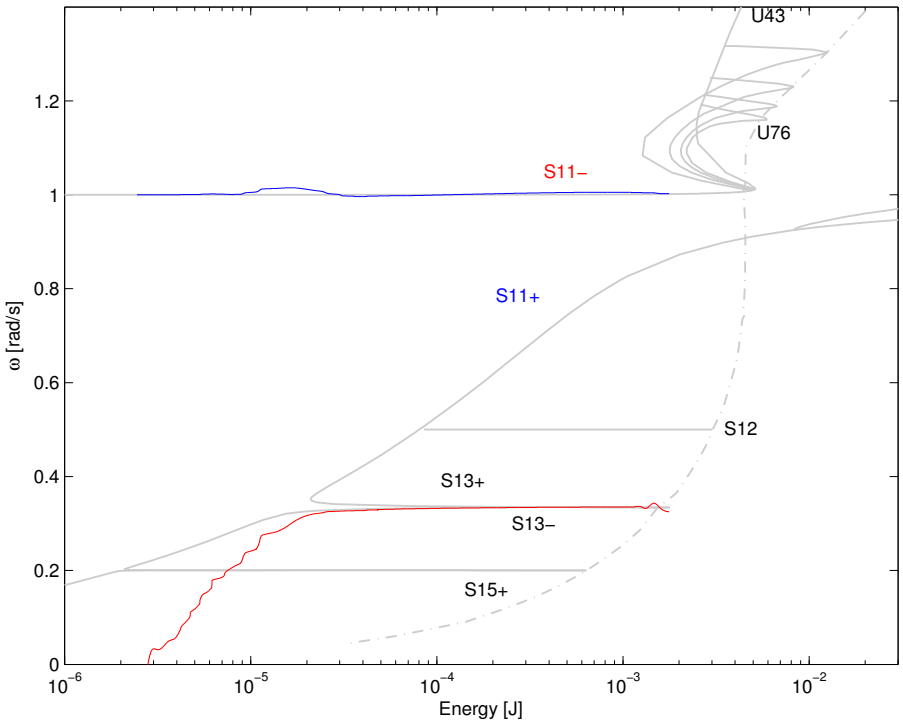

Fig. 4.1. Frequency-energy plot for the SDOF, ungrounded NES system in 1:3 TRC.

FEP tracked the S_{11-} and S_{13-} branches exactly as expected. There are several tools and methodologies that help generate correct IMFs and frequency estimates; the one to use for a particular system is best determined on an individual basis. The resulting FEP is shown in Fig. 4.1 (reproduced below from Fig. 2.36). This system was excited with velocity initial conditions and zero displacement initial conditions. Next, the same physical system was excited with initial velocity on just the first cart, and it was observed that the system tracked the manifold of impulsive orbits (Fig. 4.2). This is a demonstration of a phenomenon not previously observed and shows the beauty of the algorithm: rather than go through complicated mathematics to arrive at the analytical FEP, the four step procedure summarized at the beginning of this section is able to construct the FEP quickly. Finally, to apply the algorithm to a practical situation, various sets of legacy experimental data were obtained [8]. The FEP was then generated for both the experimental data and for a simulation corresponding to the system parameters of the experimental data. These results are referenced in Figs. 4.3 and 4.4. Although the process is not fully automatic at the time

of writing, it is successfully able to generate an FEP with appropriate user intervention for both experimental and simulation data, which is promising for future signal processing in dynamics research.

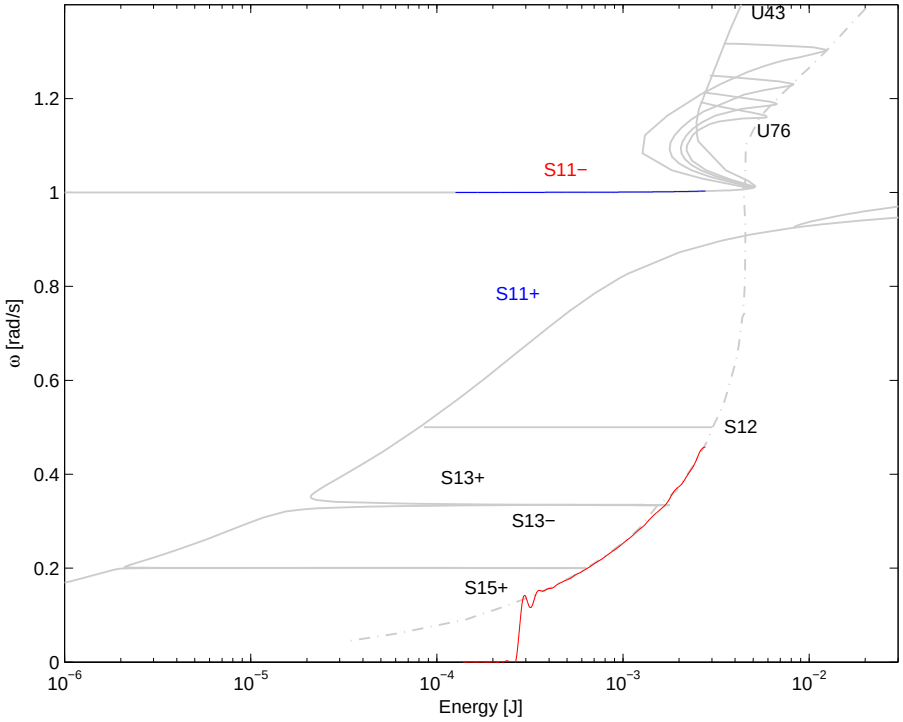

Fig. 4.2. The FEP corresponding to the system with initial velocity on only the linear oscillator and with initial energy E_{new}.

4.2 Future Work

The main thrust of this research has been to consider FEP construction from time-series data, and to this end there are several topics that can be investigated further. Currently, the ability of the algorithm to produce comprehensible FEPs is dictated largely by the experience of the analyst. This occurs in two stages: one to decide whether to include a masking signal and the second to determine the right IMF frequencies to plot in the FEP. (This second stage incorporates a number of subtasks; a discussion of some of the considerations was provided in Chapter 3.) A natural and practical extension would thus be to consider the automation of this algorithm that would first judge the IMFs generated

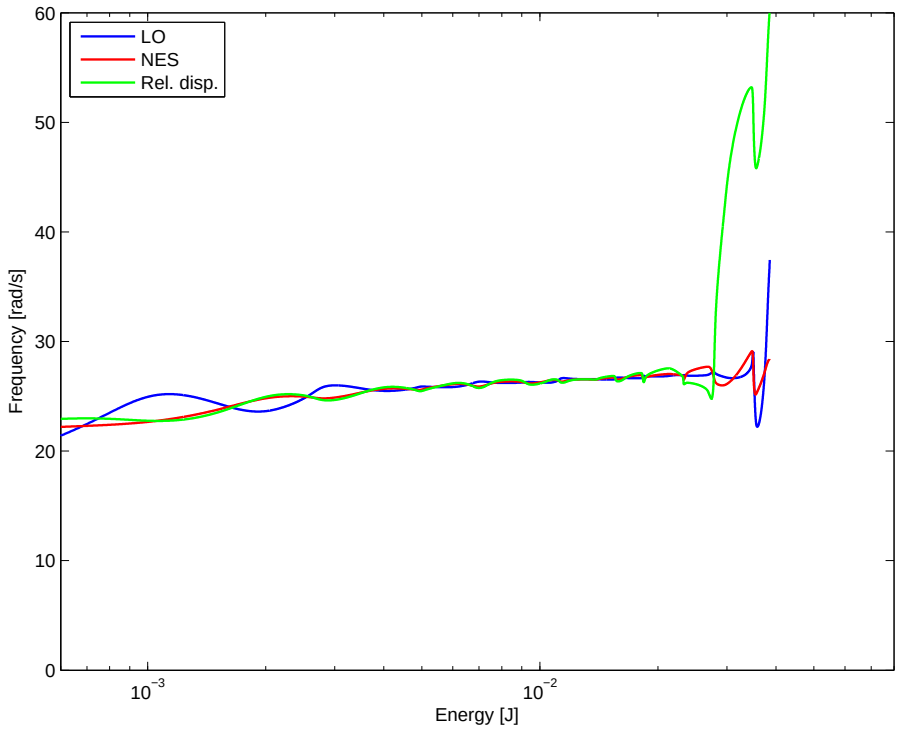

Fig. 4.3. The FEP produced from experimental data also tracks the 1:1 resonance capture between the LO and NES.

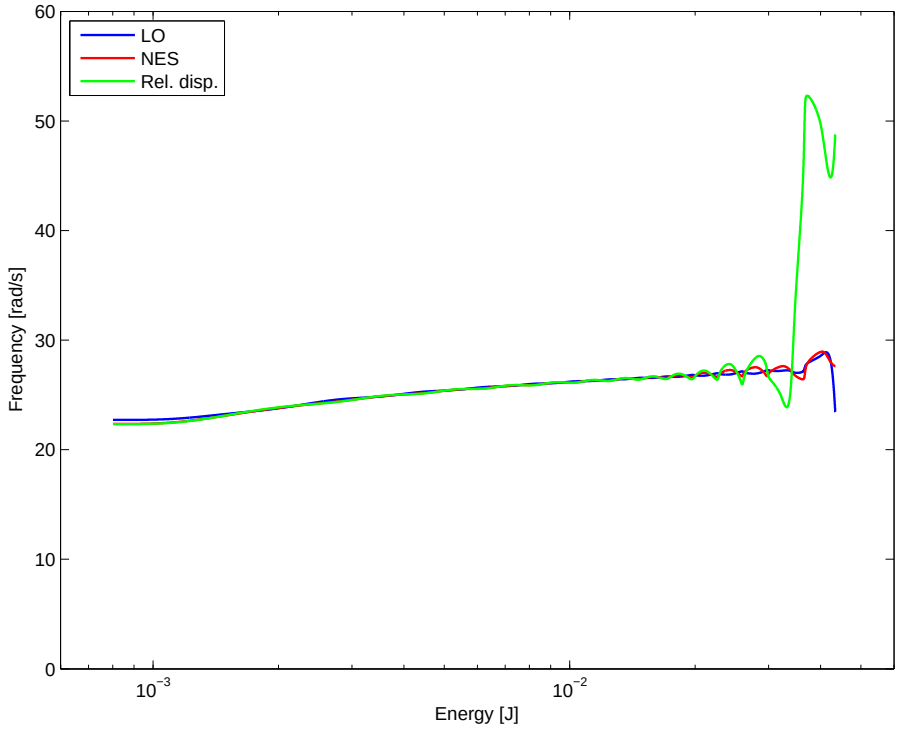

Fig. 4.4. The FEP produced from simulation data shows the clear 1:1 resonance capture between the LO and NES.

from the standard EMD process and then decide whether a masking signal would be suitable. The EMD process is truly empirical (recall its name is "empirical mode decomposition"), so while it may be difficult to specify exactly what masking signal is appropriate, some form of automation here would make the algorithm itself adaptable to a wider variety of inputs. The choice of which frequencies to plot is also related to this flexibility. There is no automatic consideration of IMF amplitude, for instance, when deciding what frequencies of which IMFs to plot (and for what duration to plot those frequencies). For a fully hands-off process, the algorithm would need to perform this step automatically. Of course, there is no guarantee that the FEP generated from this automatic process would be correct: a certain level of understanding is required still, and even then, manual adjustment of various parameters may be required to generate the best-looking FEP.

Although not directly related to the algorithm described, it would also be interesting to study the nonlinear spring. There exists a linear term in its restoring force that has been ignored for these systems (assumed zero preload), and as evident in the two-term approximation of the restoring force (eq. (1.3)), the linear term increases as the preload increases. This was studied in brief in McFarland et al. [13], but further study—and experimental and simulation verification—would shed additional light on this topic. There are several potential applications for an oscillating attachment whose behavior could be adjusted between linear and nonlinear. Although the essential nonlinearity would be lost, this type of a nonlinear system would be especially versatile since the system itself remains the same; only the preload in the wire changes.

Bibliography

[1] Deering, R. and J. F. Kaiser (2005). The use of a masking signal to improve empirical mode decomposition. In *Acoustics, Speech, and Signal Processing, 2005. Proceedings. (ICASSP '05). IEEE International Conference on*, Volume 4, pp. 485–489.

[2] Gendelman, O., L. Manevitch, A. Vakakis, and R. M'Closkey (2001, Jan). Energy pumping in nonlinear mechanical oscillators: Part I – dynamics of the underlying Hamiltonian systems. *Journal Of Applied Mechanics-Transactions of the ASME 68*(1), 34–41.

[3] Goupillaud, P., A. Grossmann, and J. Morlet (1984). Cycle-octave and related transforms in seismic signal analysis. *Geoexploration 23*(1), 85 – 102.

[4] Huang, N. E., Z. Shen, S. R. Long, M. C. Wu, H. H. Shih, Q. Zheng, N.-C. Yen, C. C. Tung, and H. H. Liu (1998). The empirical mode decomposition and the Hilbert spectrum for nonlinear and non-stationary time series analysis. *Proceedings of the Royal Sociey of London 454*, 903–995.

[5] Kerschen, G., O. Gendelman, A. F. Vakakis, L. A. Bergman, and D. M. McFarland (2008). Impulsive periodic and quasi-periodic orbits of coupled oscillators with essential stiffness nonlinearity. *Communications in Nonlinear Science and Numerical Simulation 13*(5), 959 – 978.

[6] Kerschen, G., Y. S. Lee, A. F. Vakakis, D. M. McFarland, and L. A. Bergman (2005). Irreversible passive energy transfer in coupled oscillators with essential nonlinearity. *SIAM Journal on Applied Mathematics 66*(2), 648–679.

[7] Kerschen, G., A. F. Vakakis, Y. S. Lee, D. M. McFarland, J. J. Kowtko, and L. A. Bergman (2005). Energy transfers in a system of two coupled oscillators with essential nonlinearity: 1:1 resonance manifold and transient bridging orbits. *Nonlinear Dynamics 42*(3), 283–303.

[8] Kowtko, J. J. (2005, May). Experiments with nonlinear energy sinks: A novel approach to vibrational energy dissipation. Master's thesis, The University of Illinois at Urbana-Champaign, Urbana, IL.

[9] Lee, Y. S., G. Kerschen, A. F. Vakakis, P. Panagopoulos, L. Bergman, and D. M. McFarland (2005). Complicated dynamics of a linear oscillator with a light, essentially nonlinear attachment. *Physica D: Nonlinear Phenomena 204*(1-2), 41 – 69.

[10] Lee, Y. S., S. Tsakirtzis, A. F. Vakakis, L. A. Bergman, and D. M. McFarland (2009). Physics-based foundation for empirical mode decomposition. *AIAA Journal 47*(12), 2938–2963.

[11] Lee, Y. S., A. F. Vakakis, L. A. Bergman, D. M. McFarland, G. Kerschen, F. Nucera, S. Tsakirtzis, and P. N. Panagopoulos (2008). Passive non-linear targeted energy transfer and its applications to vibration absorption: a review. *Proceedings of the Institution of Mechanical Engineers – Part K – Journal of Multi-body Dynamics 222*(2), 77–134.

[12] McFarland, D. M., L. Bergman, and A. F. Vakakis (2005). Experimental study of non-linear energy pumping occurring at a single fast frequency. *International Journal of Non-Linear Mechanics 40*, 891–899.

[13] McFarland, D. M., A. F. Vakakis, L. A. Bergman, and T. J. Copeland (2009). Characterization of a strongly nonlinear laboratory benchmark system.

[14] Meirovitch, L. (1977). *Elements of Vibration Analysis*. McGraw-Hill.

[15] Meirovitch, L. (1996). *Principles and Techniques of Vibrations*. Prentice Hall.

[16] Peel, M., G. Amirthanathan, G. Pegram, T. McMahon, and F. Chiew (2005). Issues with the application of empirical mode decomposition analysis. In A. Zerger and R. M. Argent (Eds.), *MODSIM05 International Congress on Modelling and Simulation. Proceedings.*, pp. 1681–1687. Modelling and Simulation Society of Australia and New Zealand.

[17] Peeters, M., R. Vigui, G. Srandour, G. Kerschen, and J.-C. Golinval (2009). Nonlinear normal modes, part II: Toward a practical computation using numerical continuation techniques. *Mechanical Systems and Signal Processing 23*(1), 195 – 216.

[18] Rilling, G., P. Flandrin, and P. Gonçalvès (2003). On empirical mode decomposition and its algorithms. In *Proceedings of IEEE-EURASIP Workshop on Nonlinear Signal and Image Processing NSIP-03*, Grado (Italy).

[19] Senroy, N., S. Suryanaraayanan, and P. F. Ribeiro (2007). An improved Hilbert-Huang method for analysis of time-varying waveforms in power quality. *IEEE Transactions on Power Systems 22*(4), 1843–1850.

[20] Tongue, B. (2001). *Principles of Vibrations* (2 ed.). Oxford University Press.

[21] Vakakis, A. F. and O. Gendelman (2001). Energy pumping in nonlinear mechanical oscillators: Part II–resonance capture. *Journal of Applied Mechanics-Transactions of the ASME 68*(1), 42–48.

[22] Vakakis, A. F., O. V. Gendelman, L. A. Bergman, D. M. McFarland, G. Kerschen, and Y. S. Lee (2008). *Nonlinear Targeted Energy Transfer in Mechanical and Structural Systems*, Volume I. Springer.